

FAILURE ASSESSMENT IN AEROSPACE SYSTEMS
VIA INTEGRATED MULTI-FUNCTIONAL
SENSORS

by

İSMAİL ERKİN GÖNENLİ

Presented to the Faculty of the Graduate School of
The University of Texas at Arlington in Partial Fulfillment
of the Requirements
for the Degree of

DOCTOR OF PHILOSOPHY

THE UNIVERSITY OF TEXAS AT ARLINGTON

May 2010

Copyright © by İsmail Erkin Gönenli 2010

All Rights Reserved

ACKNOWLEDGEMENTS

I would like to express my sincere gratitude to my advisor Professor Zeynep Çelik-Butler for her continuous direction and support throughout my Ph.D. Her excellent remarks and continuous guidance were invaluable in getting the best out of my research and developing as a researcher.

I like to thank Dr. Donald Butler, Dr. Jung-Chih Chiao, Dr. Michael Vasilyev and Dr. Samir Iqbal for taking part in my dissertation committee. I am especially grateful to Dr. Donald Butler for his help and clever solutions with any kind of problems I had in my research. I also like to thank Lockheed Martin and Air Force Office of Research for their financial support.

I am thankful to all Nanofab staff. I especially would like to single out Dennis Bueno and Eduardo Maldonado for their prompt attendance to equipment troubles no matter how busy they are.

I like to thank all my friends in Nanofab, especially Tanvir, Mukti, Rohit, Gaviraj, Shahriar, Suraj and Murali for the fruitful discussions we had and all their help. I feel lucky for working with such nice people.

I am indebted to my wife Özge for her continuous love, understanding and support during that difficult time. I also would like to thank all my family members, especially my father Yalçın, my mother Yıldız and my brother Burçin for their love, support and encouragement.

I feel very lucky for having my baby daughter Lara Ceylin. She was my joy during my last year.

April 14, 2010

ABSTRACT

FAILURE ASSESSMENT IN AEROSPACE SYSTEMS VIA INTEGRATED MULTI-FUNCTIONAL SENSORS

İsmail Erkin Gönenli, PhD

The University of Texas at Arlington, 2010

Supervising Professor: Zeynep Çelik-Butler

Integrated sensors fabricated on flexible substrates show lots of promise due to their ability to conform on non-planar surfaces. Potential applications could be smart-skin and wearable electronics which can be used on prosthetic devices or in harsh environments to provide with the sense of feel of the ambient.

Design, fabrication and characterization of MEMS piezoresistive pressure sensors and capacitive accelerometers were done on silicon (Si) and flexible polymer substrates using surface micromachining to be used on aerospace applications. Devices were successfully tested on planar surfaces.

For the pressure sensor fabrication, Si_3N_4 was used as a membrane material due to its linear stress-strain response and high elasticity while polysilicon was used as a piezoresistive material because of its high gauge factor as well as linear response. Response measurements of fabricated devices resulted in slightly lower values compared to the ones obtained from simulations.

Accelerometer fabrication was done with UV-LIGA (Ultra-violet Lithographie, Galvanoformung, Abformung). Nickel (Ni) was used as a proof mass because of its relatively

high density and corrosion resistance. Response measurements of fabricated accelerometers resulted in higher values compared to simulated ones.

Although there was difference between simulated and fabricated responses, device measurements on Si and flexible substrates showed comparable values.

TABLE OF CONTENTS

ACKNOWLEDGEMENTS	iii
ABSTRACT	iv
LIST OF ILLUSTRATIONS.....	ix
LIST OF TABLES	xii
Chapter	Page
1. INTRODUCTION.....	1
1.1 Introduction.....	1
1.2 MEMS Sensors in Failure Assessment.....	2
1.3 Flexible Substrate	2
1.4 Pressure Sensors.....	4
1.5 Piezoresistivity.....	4
1.5.1 Mathematical Expression of Piezoresistivity	5
1.5.2 Polysilicon as Piezoresistor.....	7
1.5.2.1 Electrical Properties	8
1.5.2.2 Mechanical Properties.....	10
1.5.2.3 Gauge Factor	11
1.5.2.4 Transverse and Longitudinal Coefficients	11
1.6 Aluminum Induced Crystallization	13
1.7 Accelerometers	15
1.8 Damping Force.....	16
1.8.1 Slide Film Air Damping.....	16
1.8.2 Squeeze Film Air Damping	18

1.9 Electroplating	20
1.10 Summary.....	21
2. PIEZORESISTIVE MEMS PRESSURE SENSORS	23
2.1 Introduction.....	23
2.2 Wheatstone Bridge.....	24
2.3 Design	26
2.4 Fabrication.....	29
2.5 Characterization	33
2.5.1 I-V Measurements.....	33
2.5.2 Response Measurements	35
2.5.3 Gauge Factor Calculations.....	37
2.6 Summary.....	39
3. CAPACITIVE MEMS ACCELEROMETERS	41
3.1 Introduction.....	41
3.2 Design	42
3.3 Fabrication.....	47
3.4 Characterization	51
3.4.1 Measurement Setup.....	51
3.4.2 Response Measurements	52
3.5 Summary.....	60
4. CONCLUSIONS	62
APPENDIX	
A. PRESSURE SENSOR DESIGNS AND SIMULATIONS	65
B. PRESSURE SENSOR SIMULATION SETTINGS AND CALCULATIONS	74
C. I-V CHARACTERIZATION RESULTS OF PRESSURE SENSORS	85
D. CAPACITIVE ACCELEROMETER DESIGNS	94

E. ACCELEROMETER SIMULATION SETTINGS AND CALCULATIONS	100
F. RESPONSE CHARACTERIZATION RESULTS OF ACCELEROMETERS.....	111
REFERENCES.....	118
BIOGRAPHICAL INFORMATION	127

LIST OF ILLUSTRATIONS

Figure	Page
1.1 Normal and shear stress components acting on the surface of a cube.....	5
1.2 Simple electrical model for polysilicon with grains and grain boundaries showing the series resistance structure.....	8
1.3 Current, voltage and stress relation representing (a) longitudinal piezoresistive coefficient, (b) transverse piezoresistive coefficient cases.....	12
1.4 Illustration of eutectic metal model (a) a-Si diffuses into Al, (b) formation of nuclei, (c) and (d) grain growth and layer inversion	14
1.5 Illustration of compound forming metal model (a) Initial layer structure, (b) formation of metal silicide, (c) silicide migration through a-Si, (d) crystallization of a-Si during silicide migration	15
1.6 Mass spring system showing the dynamic behavior of an accelerometer.....	16
1.7 Basic model of the slide film damping, showing the movement parallel to air film	17
1.8 Basic model showing the squeeze film damping behavior and pressure build up	19
1.9 Model showing the electroplating process	20
1.10 Discharge, nucleation and continuous film formation on the cathode surface	21
2.1 Cross sectional view of a basic piezoresistive MEMS pressure sensor	24
2.2 Wheatstone bridge circuit diagram. Arrows on the diagram denote resistors in the active sensor area	24
2.3 Piezoresistive pressure sensors in half Wheatstone bridge configuration	26
2.4 Boundary conditions for pressure sensor simulations	27
2.5 Displaced membrane to determine high strain region	28
2.6 Piezoresistors at high strain region of displaced membrane	28
2.7 Trench opening on Si ₃ N ₄ membrane (a) simulated, (b) fabricated	30

2.8	Fabrication of piezoresistors (a) simulated, (b) fabricated.....	31
2.9	Fabrication of metallization layer and bond pads (a) simulated, (b) fabricated	32
2.10	Illustration of the undercut after ashing (a) simulated, (b) fabricated.....	32
2.11	Illustration of the setup to measure pressure sensor response	36
2.12	Surface profile through a ripped off membrane. The 5 μm gap is formed by the sacrificial layer of 3.1 μm and membrane with a thickness of 1.9 μm	37
2.13	Simulation results for membranes displaced by 3.1 μm to determine average strain on piezoresistors. Pressures given are the values required to displace membrane by 3.1 μm . Output voltages and resistance changes were calculated assuming a gauge factor of 50 and input voltage of 1 V. a) $P=78\text{ MPa}$, $\epsilon_{\text{AVG}}=7.05\times 10^{-4}$, $\Delta R/R=3.52\%$, $V_{\text{out}}=17.30\text{ mV}$ b) $P=120\text{ MPa}$, $\epsilon_{\text{AVG}}=9.9\times 10^{-4}$, $\Delta R/R=4.95\%$, $V_{\text{out}}=24.15\text{ mV}$ c) $P=128\text{ MPa}$, $\epsilon_{\text{AVG}}=9.46\times 10^{-4}$, $\Delta R/R=4.73\%$, $V_{\text{out}}=23.10\text{ mV}$ d) $P=73\text{ MPa}$, $\epsilon_{\text{AVG}}=7.53\times 10^{-4}$, $\Delta R/R=3.76\%$, $V_{\text{out}}=18.45\text{ mV}$	38
3.1	Z-axis accelerometer supported by four springs.....	42
3.2	Basic lateral axis accelerometer structure	43
3.3	Illustration of displacement for z-axis accelerometer for 1g acceleration in the sensing direction.....	46
3.4	Illustration of displacement for lateral axis accelerometer for 1g acceleration in the sensing direction.....	47
3.5	Interconnect metallization layer for z-axis accelerometers (a) simulated, (b) fabricated.....	48
3.6	Patterned polyimide layer for z-axis accelerometers (a) simulated (b) fabricated	48
3.7	Patterned NR-4 8000 P mold photoresist showing (a) combs for x, y-axes, (b) z-axis accelerometer	49
3.8	Electroplated z-axis accelerometer (a) simulated (b) fabricated.....	50
3.9	Suspended accelerometer (a) simulated (b) top view of fabricated device.....	50
3.10	Illustration of the setup which is used to measure accelerometer response	52
3.11	Circuit diagram of MS 3110 capacitive readout circuitry.....	52
3.12	Time domain plot of overlapped amplitude data for the reference and fabricated accelerometer	53

3.13 Time domain plot of reference and fabricated accelerometer after phase adjustment.....	54
3.14 Voltage and capacitance response of the z-axis accelerometer on Si substrate. Capacitance change is 39 fF/g	54
3.15 Voltage and capacitance response of the z-axis accelerometer on Si substrate. Capacitance change is 32.4 fF/g	55
3.16 Voltage and capacitance response of the z-axis accelerometer on flexible polymer substrate. Capacitance change is 27.7 fF/g	55
3.17 Voltage and capacitance response of the z-axis accelerometer on flexible polymer substrate. Capacitance change is 25.2 fF/g	56
3.18 Voltage and capacitance response of the x,y-axis accelerometer on Si substrate. Capacitance change is 11.9 fF/g	56
3.19 Voltage and capacitance response of the x,y-axis accelerometer on Si substrate. Capacitance change is 17.5 fF/g	57
3.20 Folded beam spring	59

LIST OF TABLES

Table	Page
1.1 Transverse and longitudinal piezoresistive coefficients for different cubic crystal directions	13
2.1 Material properties used for simulations	27
2.2 Process details of photoresists that were used in pressure sensor fabrication	33
2.3 Resistance values measured from the slope of I-V charts assuming linear fit	34
2.4 Individual resistance values, which are calculated using MathCAD	34
2.5 Comparison of calculated and measured offset voltages for 1 V DC bias. Sample 8 was measured applying 3 V DC bias	35
2.6 Differential output voltage and voltage response values in response to 1 V input. For Sample 8, 3 V input was applied	36
2.7 Actual gauge factor values calculated using measured differential output voltages	39
3.1 Properties of Ni used in simulations	43
3.2 Process details of photoresists that were used in accelerometer fabrication	51
3.3 Sensitivity of accelerometers fabricated on silicon and flexible polymer substrates	58

CHAPTER 1
INTRODUCTION
1.1 Introduction

Advances in the semiconductor industry made miniaturization of sensors possible. By integrating electronic circuits with mechanical parts on a common substrate new intelligent micro systems called microelectromechanical systems (MEMS) were created to monitor the environment and its behavior by measuring pressure, acceleration, temperature, etc.

Mechanical MEMS sensors, particularly pressure sensors and accelerometers have the biggest share in MEMS industry. MEMS accelerometers are used to monitor inertial navigation, to do tilt measurements and control air-bag systems. Similarly, MEMS pressure sensors are used in manifold systems or to check tire pressures.

Recently there has been a growing interest in fabricating electronic circuits and sensors on flexible substrates as they can fit on non-planar surfaces and are cost effective. Flexible substrates show promise in the efforts of fabricating wearable electronics and smart skin, i.e. an integrated array of sensors [1, 2]. Such applications require integration of several sensors on a common substrate and low temperature fabrication compatible with the stringent temperature restrictions of the flexible polymer substrates.

The objective of this work is demonstration of design, fabrication and characterization of piezoresistive pressure sensors and capacitive accelerometers. This is the first attempt to fabricate accelerometers on a flexible substrate. In this work, maximum process temperature was 550 °C, which is compatible with polymer materials used. For these reasons, this work is an important contribution towards the realization of smart skin.

1.2 MEMS Sensors in Failure Assessment

Failure assessment through condition based monitoring is a routine practice which is used to predetermine any developing failure conditions to enhance machine availability, reduce repair costs and provide safety [3]. The evaluations are generally based on pressure and vibration monitoring [4]. Using conventional equipment to measure these parameters is both costly and difficult because of the equipment sizes, especially when multipoint measurements are needed [3, 4]. Thus, there is a growing interest in MEMS sensors for nondestructive failure analysis. MEMS sensors were shown to operate for such applications in industries like aerospace, automotive and construction [5-8].

1.3 Flexible Substrate

Currently, most device fabrication is done on silicon substrates. However, Si substrates suffer from mechanical problems such as brittle fracture and non-conformality [9]. Recently, device fabrication on flexible substrate became a promising field of research due to its potential applications such as smart tags, electronic textiles, artificial skin and prosthetic devices due to its ability to follow non-planar contours [10]. Devices on flexible substrates were reported before [11-15] and were shown to have comparable results with their counterparts on rigid substrates [15, 16]. Such substrates should be chemically inert, have high elastic modulus and comparable thermal expansion coefficients to the films formed on top, and electrically insulating [17].

So far three types of substrates, glass [18], polymer [19] and metal [20], were used for device fabrication. All of them have their advantages and disadvantages. Thinned glass plates can be used as substrates; especially for optical applications since they retain their optical properties after thinning. Nevertheless, they are difficult to handle due to their fragility and high cost. Polymers are cheap and highly flexible, but they are not suitable for high temperature processes. Metal foil substrates are attractive for optical applications as well as those requiring high thermal and mechanical durability. However, they are conducting and have high surface roughness, so they require insulating coatings and surface polishing [17].

During microfabrication on flexible substrates, thin films are grown on the substrate in sequential order to build devices. Generally, there is a mismatch between the physical properties of the substrate and grown layers, as well as inbetween different layers, which results in strain, induced on the whole structure. Main reasons for strain are the mismatch between elastic modulus and the thermal expansion coefficient between different layers. The overall strain, ε_M , exerting on a non-deformed substrate/film couple is tensile if the value is positive and can be expressed as

$$\varepsilon_M = \varepsilon_0 + \varepsilon_{th} \quad (1.1)$$

where ε_0 is the mismatch strain between the film and the substrate and ε_{th} is the thermal strain which can be expressed as

$$\varepsilon_{th} = (\alpha_f - \alpha_s) \Delta T \quad (1.2)$$

where α_f and α_s are the respective film and substrate thermal expansion coefficients and ΔT is the change in temperature with reference to room temperature. When the substrate is bent, the top surface is in tension and bottom surface is in compression. Assuming that film and substrate have comparable elastic modulus ($Y_f \approx Y_s$), strain on top of the film can be expressed as

$$\varepsilon_{top} = (d_f + d_s) / 2R \quad (1.3)$$

where d_f and d_s are the film and substrate thicknesses, respectively and R is the radius of curvature [21].

If elastic moduli of substrate and film are different ($Y_f > Y_s$), strain front moves towards the substrate and the strain on the top of film can be expressed as

$$\varepsilon_{top} = \left(\frac{(d_f + d_s)}{2R} \right) \frac{(1 + 2\eta + \chi\eta^2)}{(1 + \eta)(1 + \chi\eta)} \quad (1.4)$$

where $\eta = d_f/d_s$ and $\chi = Y_f/Y_s$ [21]. In this case, the strain on the top surface is reduced by several factors with changing η value.

For a device on flexible substrate to operate properly, it should be able to stay intact and retain its functionality even after being stressed.

1.4 Pressure Sensors

A pressure sensor is a device which is used to detect pressure changes. There are three different kinds of pressure measurements, namely absolute pressure, differential pressure and gauge pressure. Absolute pressure is measured relative to perfect vacuum. Differential pressure measures the pressure between two different points and gauge pressure is measured relative to atmospheric pressure. The same device can be used to measure different kinds of pressures [22].

The most important requirements for a good pressure sensor are high sensitivity, good resolution, quick response to detect pressure changes and reproducibility. Sensitivity (S) is the difference in output voltage per applied pressure difference and given as:

$$S = \frac{\Delta V}{\Delta P} \frac{1}{V_b} \quad (1.5)$$

where ΔV , ΔP and V_b are output voltage difference, pressure difference and input voltage bias, respectively [23].

Generally either capacitive or piezoresistive pressure sensors are used for sensing. Working principles of these sensors are given in Section 2.1 of Chapter 2.

1.5 Piezoresistivity

Piezoresistivity is a material property, where resistivity changes under an applied stress. It was first discovered in germanium and silicon by Smith [24] and Adams [25] in Bell Labs in 1954.

Both metals and semiconductors were shown to display piezoresistive effect [26-28]. For a metal, piezoresistive effect is suggested to be a result of dimensional change due to strain [29], whereas for a semiconductor strain gauge, it is proposed to be due to a change in carrier density related to shifting in band positions under applied stress [30].

1.5.1 Mathematical Expression of Piezoresistivity

Piezoresistivity relates the electric field vector (ε) with current vector (i) through resistivity (ρ) in three dimensions. For an anisotropic three dimensional crystal, this relation can be expressed by a three-by-three tensor matrix. For a symmetrical crystal, however, these nine coefficients reduce to six due to symmetry and the tensor can be expressed as:

$$\begin{bmatrix} \varepsilon_1 \\ \varepsilon_2 \\ \varepsilon_3 \end{bmatrix} = \begin{bmatrix} \rho_1 & \rho_6 & \rho_5 \\ \rho_6 & \rho_2 & \rho_4 \\ \rho_5 & \rho_4 & \rho_3 \end{bmatrix} \begin{bmatrix} i_1 \\ i_2 \\ i_3 \end{bmatrix} \quad (1.6)$$

For an isotropic structure, such as cubic lattice, $\rho_1 = \rho_2 = \rho_3 = \rho$ and $\rho_4 = \rho_5 = \rho_6 = 0$.

Equation 1.6 is valid for an unstressed condition. However, if the material of concern is piezoresistive, then the resistivity components depend on stress. In this case, stress components acting on a cube of infinitesimal dimensions dx , dy and dz can be expressed using three normal stress components, which are acting perpendicular to the surface of the cube and three shear stress components acting parallel to the surface as illustrated in Fig. 1.1 [31].

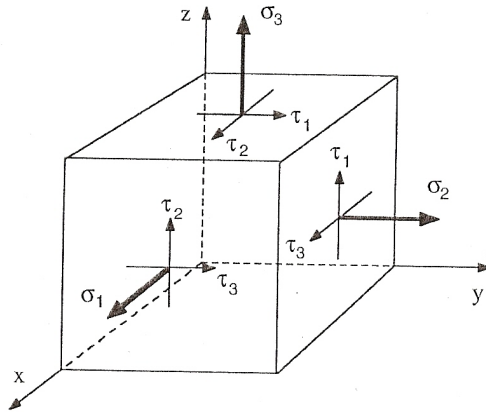


Fig. 1.1 Normal and shear stress components acting on the surface of a cube [31]

Considering an isotropic and unstressed case, six resistivity components can be expressed as:

$$\begin{bmatrix} \rho_1 \\ \rho_2 \\ \rho_3 \\ \rho_4 \\ \rho_5 \\ \rho_6 \end{bmatrix} = \begin{bmatrix} \rho \\ \rho \\ \rho \\ 0 \\ 0 \\ 0 \end{bmatrix} + \begin{bmatrix} \Delta\rho_1 \\ \Delta\rho_2 \\ \Delta\rho_3 \\ \Delta\rho_4 \\ \Delta\rho_5 \\ \Delta\rho_6 \end{bmatrix} \quad (1.7)$$

By relating the fractional resistivity changes to six stress components, a matrix of 36 components can be found which describes the piezoresistance effect. The elements of this matrix are called piezoresistance coefficients and symbolized as π_{ij} with unit of Pa^{-1} [31].

To be able to calculate the matrix, ideally 36 measurements have to be conducted. Nonetheless, by using symmetry operations, the matrix could be calculated theoretically for a crystalline material. Symmetry conditions of crystal structures generally result in disappearance of some of the matrix components, reducing the number to less than 36 and simplifying it. For the cubic structures such as germanium and silicon, only π_{11} , π_{12} and π_{44} remain and the matrix can be written as

$$\frac{1}{\rho} \begin{bmatrix} \Delta\rho_1 \\ \Delta\rho_2 \\ \Delta\rho_3 \\ \Delta\rho_4 \\ \Delta\rho_5 \\ \Delta\rho_6 \end{bmatrix} = \begin{bmatrix} \pi_{11} & \pi_{12} & \pi_{12} & 0 & 0 & 0 \\ \pi_{12} & \pi_{11} & \pi_{12} & 0 & 0 & 0 \\ \pi_{12} & \pi_{12} & \pi_{11} & 0 & 0 & 0 \\ 0 & 0 & 0 & \pi_{44} & 0 & 0 \\ 0 & 0 & 0 & 0 & \pi_{44} & 0 \\ 0 & 0 & 0 & 0 & 0 & \pi_{44} \end{bmatrix} \begin{bmatrix} \sigma_1 \\ \sigma_2 \\ \sigma_3 \\ \tau_1 \\ \tau_2 \\ \tau_3 \end{bmatrix} \quad (1.8)$$

Combining Eqs. 1.6 and 1.7 leads to the expression for electric field in a cubic crystal under stress which can be expressed as:

$$\begin{aligned} \varepsilon_1 &= \rho i_1 + \rho \pi_{11} \sigma_1 i_1 + \rho \pi_{12} (\sigma_2 + \sigma_3) i_1 + \rho \pi_{44} (i_2 \tau_3 + i_3 \tau_2) \\ \varepsilon_2 &= \rho i_2 + \rho \pi_{11} \sigma_2 i_2 + \rho \pi_{12} (\sigma_1 + \sigma_3) i_2 + \rho \pi_{44} (i_1 \tau_3 + i_3 \tau_1) \\ \varepsilon_3 &= \rho i_3 + \rho \pi_{11} \sigma_3 i_3 + \rho \pi_{12} (\sigma_1 + \sigma_2) i_3 + \rho \pi_{44} (i_1 \tau_2 + i_2 \tau_1) \end{aligned} \quad (1.9)$$

The first term in Eq.1.9 is the contribution from the unstressed condition. The second term represents the effect of stress on the voltage drop with current flow in the same direction as stress. Other terms define the more complicated behavior under stress and depend on the material properties. It should be noted that Eq. 1.9 is valid only for bulk materials and for finite dimensions. The effect of dimension changes should also be considered. In addition, it should be noted that piezoresistive coefficients could be positive or negative depending on doping type, concentration and temperature [31].

1.5.2 Polysilicon as Piezoresistor

Polysilicon is a polycrystalline material which is made up of a network of small single crystalline silicon grains of varying orientation. These grains with different orientations meet at the grain boundaries to form a very thin amorphous layer. This amorphous layer, which acts as a barrier has large impact on electrical properties as well as mechanical. The microstructure and orientation highly depend on the processing conditions, which makes it difficult to develop a precise fabrication process flow [32].

Polysilicon is an important material both for semiconductor and MEMS industry. Heavily doped polysilicon is used as gate material in MOSFET devices [33]. Its piezoresistive properties make it an important strain gauge material in MEMS industry, to be used with shear force sensors [34], pressure sensors [35] and accelerometers [36].

The advantages of polysilicon as a piezoresistive material over others can be stated as follows:

- Polysilicon can be deposited as a thin film, which makes it advantageous over single crystal silicon although the former has a gauge factor of 60-70% of the latter under same doping condition [37].
- Compared with metals, it has a relatively high gauge factor.
- Compared to metal strain gauges, polysilicon strain gauges show reduced hysteresis and creep which leads to more repeatable results.

- Its ease of fabrication allows high device density.
- On chip circuitry can be integrated along with piezoresistors and the structure holding them for signal amplification and temperature compensation.

1.5.2.1 Electrical Properties

Polysilicon is made up of grains which are oriented in different crystallographic directions and separated by a thin, amorphous grain boundary. As two different orientations meet, dangling bonds are created at the grain boundaries, which are passivated when polysilicon is doped, resulting in a barrier similar to Schottky barrier with a semiconductor on both sides [32].

The simple electrical model of polysilicon can be expressed as a series of resistors, where resistivity contribution comes from both grains and grain boundaries. In normal operation, voltage drop across a grain boundary is negligible so the structure is considered as a linear resistor, where resistivity is given as:

$$\rho = \left[\frac{L - (2w + \delta)}{L} \right] \rho_g + \left[\frac{2w + \delta}{L} \right] \rho_b \quad (1.10)$$

where ρ is the resistivity of a polysilicon film, ρ_g and ρ_b are resistivities for grain and grain boundary. L is the overall length of the grain and grain boundary, w is the width of the depletion layer and δ is the width of the grain boundary. The basic electrical model is illustrated in Fig.

1.2.

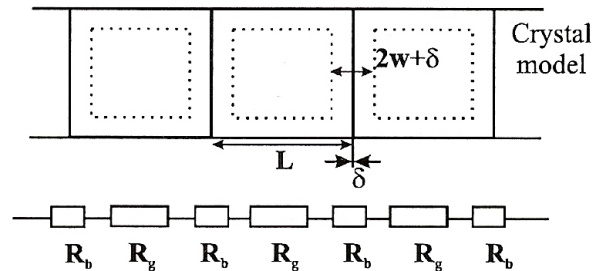


Fig. 1.2 Simple electrical model for polysilicon with grains and grain boundaries showing the series resistance structure [32].

Many models have been proposed to explain the electrical conduction in polysilicon. Two among those, “dopant segregation model” and “carrier-trapping model”, are the widely accepted ones. Other models are only derivatives of these two models [38].

There are two effects that are favoring segregation at the grain boundaries, chemical and size. Dopant atoms that are decreasing the melting temperature of Si are more favorable to segregate at the grain boundaries. Size effect favors segregation if the atomic radii of the dopants are both larger and smaller than that of Si [39]. When dopants are segregated at the grain boundaries, they are trapped and become inactive [40, 41]. The conductivity is controlled by segregation. For low doping amounts, most of the atoms are segregated at the grain boundaries and only a few atoms contribute to conductivity. At high carrier concentrations, more atoms are segregated at the grain boundaries until saturation limit is reached and resistivity approaches to that of single crystal silicon [42, 43]. Grain boundary segregation is only important for n-type dopants and does not happen in the presence of p-type dopants [44].

Carrier-trapping model, assumes that the dopant atoms are distributed uniformly throughout the material and conductivity is limited by carrier trapping at disordered structures at the grain boundaries which act as trap sites. When the charge is trapped, a depletion layer with charges of opposite sign is formed around the grain boundary. The presence of depletion layer charges cause band bending, which results in formation of a potential barrier, restricting the movement of any free charge. At low doping concentrations, assuming that most of the carriers are trapped, there are only few carriers left for conduction; depletion region expands into grains, so there is no neutral region left. The depletion region of a grain boundary of length L expands by $L/2$ for a completely depleted case and the potential barrier height can be expressed as

$$V_B = \frac{qNL^2}{8\epsilon} \quad (1.11)$$

where V_B is the barrier height, q is the electronic charge, N is number of carriers and ϵ is the permittivity of silicon. As the dopant concentration increases above a critical value such that all

trap sites are filled, the width of the depletion region decreases and the barrier height could be expressed as

$$V_B = \frac{qN_T^2}{8 \epsilon N} \quad (1.12)$$

where N_T is the number of trapped carriers per unit area of the grain boundary and constant since all the available trap sites are filled. Beyond the critical doping concentration, barrier height decreases with increased carrier number. However, depletion region width is still high and conduction takes place through thermionic emission. Further increasing dopant concentration reduces the potential barrier more as well as the depletion layer width. Conduction takes place through thermionic field emission, which is a combination of thermionic emission and tunneling, where the resistivity of the material approaches to that of single crystal grains [38, 45].

At high temperatures, carriers are energetic enough to overcome potential barrier. Therefore, conduction through the grain boundary is dominated by thermionic emission. At low temperatures, tunneling through the barrier takes place and conduction is dominated by thermionic field emission [46-49].

1.5.2.2 Mechanical Properties

It is important to understand mechanical properties of polysilicon to determine device limitations. Polysilicon has a highly orientation-dependant Young's modulus, which varies between minimum and maximum of single crystalline. This suggests that Young's modulus is not affected much by grain boundaries. However, grain boundary morphology has a profound effect on intrinsic stress.

Polysilicon deposited in polycrystalline form is suggested to be under compressive stress. This could be relieved by an annealing step at high temperature. However, this is not possible if polysilicon is integrated with other devices. As an alternative, polysilicon could be deposited at a low temperature without forming grain boundaries and then annealed at temperatures as low as 600 °C to crystallize it. This way, early grain boundary impingement can

be prevented and bigger grains can be obtained. Since the crystalline form has lower volume than amorphous, this way the stress could be shifted from compressive to tensile [32].

1.5.2.3 Gauge Factor

The gauge factor is a measure of the sensitivity of the material and can be defined as the relative change in resistance per unit strain, given as

$$G = \frac{\Delta R}{R\varepsilon} = 1 + 2\nu + \frac{\Delta\rho}{\rho\varepsilon} \quad (1.13)$$

where ν is the Poisson's ratio, ρ is the resistivity and ε is the applied strain. The gauge factor is highly dependent on grain orientation and grain boundary and it is estimated to take the average value for each grain in the case of polysilicon.

In the case of a textured structure where grains have a preferred orientation, gauge factor can be defined as

$$G = \frac{\Delta R}{R\varepsilon} = 1 - 2\frac{S_{ij}}{S_{ii}} + \frac{\pi}{S_{ii}} \quad (1.14)$$

where S_{ij} and S_{ii} are compliance coefficients.

If the grain boundaries have an influence, the films can be considered as a series resistor string and both resistors contribute to the piezoresistive effect. In that case, the change in the resistivity of silicon can be given as

$$\frac{\Delta\rho}{\rho} = \left[\frac{L - (2w + \delta)}{L} \right] \frac{\Delta\rho_g}{\rho\varepsilon} + \left[\frac{2w + \delta}{L} \right] \frac{\Delta\rho_b}{\rho\varepsilon} \quad (1.15)$$

1.5.2.4 Transverse and Longitudinal Coefficients

Once the piezoresistive coefficients of π_{11} , π_{12} and π_{44} which are defined in a coordinate system aligned to the <100> axes of silicon, piezoresistive properties in other directions can also be calculated by performing axis transformation. If a vector (x, y, z) denotes the initial axes and a vector (x^*, y^*, z^*) denotes the transferred axes, axes transformation could be defined as

$$\begin{bmatrix} x^* \\ y^* \\ z^* \end{bmatrix} = \begin{bmatrix} l_1 & m_1 & n_1 \\ l_2 & m_2 & n_2 \\ l_3 & m_3 & n_3 \end{bmatrix} \begin{bmatrix} x \\ y \\ z \end{bmatrix} \quad (1.16)$$

where l , m and n are direction cosines and given by,

$$\begin{bmatrix} l_1 & m_1 & n_1 \\ l_2 & m_2 & n_2 \\ l_3 & m_3 & n_3 \end{bmatrix} = \begin{bmatrix} c\phi c\theta c\psi - s\phi s\psi & s\phi c\theta c\psi + c\phi s\psi & -s\theta c\psi \\ -c\phi c\theta s\psi - s\theta c\psi & -s\psi c\theta s\psi + c\phi c\psi & s\theta s\psi \\ c\phi s\theta & s\phi s\theta & c\theta \end{bmatrix} \quad (1.17)$$

where θ , ϕ and ψ are the Euler angles and $c\phi = \cos \phi$, $s\theta = \sin \theta$, etc [50].

Of all possible orientations that can be found via Eq. 1.16, the most common situations arise either when uniaxial stress, electric field and current are in the same direction or when the direction of current and electric field are perpendicular to the stress as shown in Fig. 1.3.

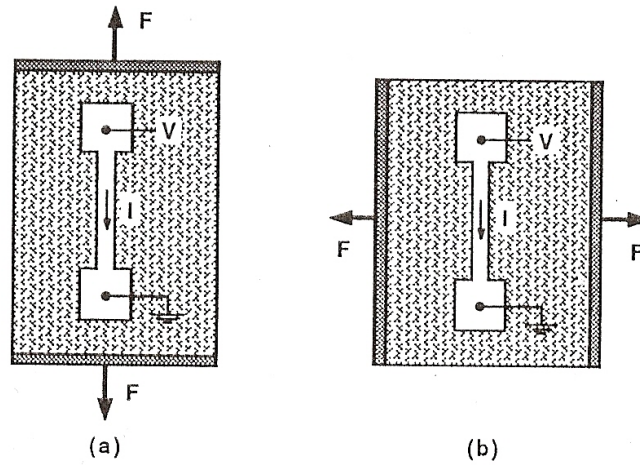


Fig. 1.3 Current, voltage and stress relation representing a) longitudinal piezoresistive coefficient b) transverse piezoresistive coefficient cases [31]

In the case of first situation, a longitudinal piezoresistive coefficient is defined and is given as

$$\pi_l = \pi_{11} + 2(\pi_{44} + \pi_{12} - \pi_{11})(l_1^2 m_1^2 + l_1^2 n_1^2 + m_1^2 n_1^2) \quad (1.18)$$

In the case of the second situation, transverse piezoresistive coefficient is defined and calculated in a similar way as

$$\pi_t = \pi_{12} - (\pi_{44} + \pi_{12} - \pi_{11})(l_1^2 l_2^2 + m_1^2 m_2^2 + n_1^2 n_2^2) \quad (1.19)$$

Longitudinal and transverse coefficients in various directions for a cubic crystal structure are given in Table 1.1.

Table 1.1 Transverse and longitudinal piezoresistive coefficients for different cubic crystal directions [31]

Longitudinal Direction	π_l	Transverse Direction	π_t
(1 0 0)	π_{11}	(0 1 0)	π_{12}
(0 0 1)	π_{11}	(1 1 0)	π_{12}
(1 1 1)	$1/3 (\pi_{11} + 2\pi_{12} + 2\pi_{44})$	(1 $\bar{1}$ 0)	$1/3 (\pi_{11} + 2\pi_{12} - 2\pi_{44})$
(1 1 $\bar{0}$)	$1/2 (\pi_{11} + \pi_{12} + \pi_{44})$	(1 1 1)	$1/3 (\pi_{11} + 2\pi_{12} - \pi_{44})$
(1 1 $\bar{0}$)	$1/2 (\pi_{11} + \pi_{12} + \pi_{44})$	(0 0 1)	π_{12}
(1 1 $\bar{0}$)	$1/2 (\pi_{11} + \pi_{12} + \pi_{44})$	(1 $\bar{1}$ 0)	$1/2 (\pi_{11} + \pi_{12} - \pi_{44})$

Piezoresistive coefficients given in Table 1 are valid for a single crystalline or textured grain structure.

1.6 Aluminum Induced Crystallization

In general, polysilicon thin films are obtained via Chemical Vapor Deposition (CVD) techniques. This can be at a low pressure (LPCVD) or atmospheric pressure (APCVD). It can also be deposited using Plasma Enhanced Chemical Vapor Deposition (PECVD). However, this technique yields amorphous silicon and requires an additional anneal step for crystallization. Due to use of high temperatures for crystallization, these techniques are not cost efficient.

Moreover, these techniques, which require high temperature processing, are not suitable for most plastic substrates due to their low thermal tolerances.

Alternatively, two different methods, namely laser anneal crystallization (LAC) [51] and metal induced crystallization (MIC) [52] can be used. The former method, LAC suffers from poor spatial uniformity and narrow process window, leaving MIC as the better candidate.

In the MIC process, a metal and a-Si (amorphous silicon) layer are deposited on top of each other. A temperature increase initiates diffusion of a-Si into metal and as the layers exchange places, crystallization takes place [53].

Two different models were proposed to explain MIC depending on the type of metal. The first model, eutectic metal, suggests that covalent bonds on the a-Si are weakened as the temperature increases facilitating diffusion of a-Si into metal layer until they find a preferred nucleation site on metal grains. As thermal treatment continues, the nuclei start to grow and eventually form a continuous film which results in a layer inversion. This process is limited by the solubility of a-Si in the metal film. Process steps for the first model are shown in Fig. 1.4 [54].

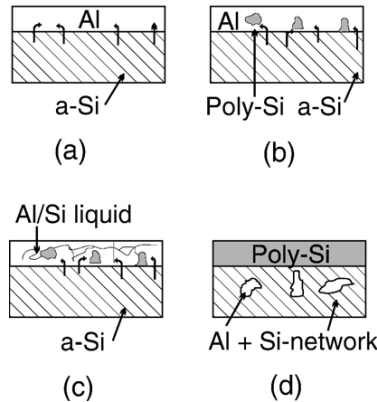


Fig. 1.4 Illustration of eutectic metal model a) a-Si diffuses into Al b) formation of nuclei c and d) grain growth and layer inversion [54]

The second model, compound-forming metal, starts with formation of the most silicide rich compound at the interface. The silicide rich compound then dissociates and forms nodules

which migrate through a-Si and leaving polysilicon on their path as they move. This process is limited by migration of silicide nodules through a-Si as shown in Fig. 1.5 [54].

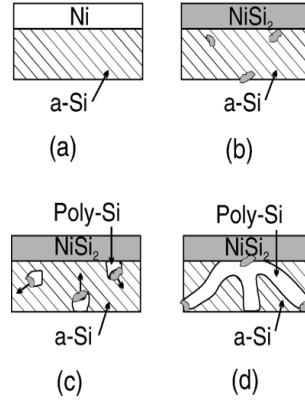


Fig. 1.5 Illustration of compound forming metal model a) Initial layer structure b) formation of metal silicide c) silicide migration through a-Si d) crystallization of a-Si during silicide migration [54]

Aluminum is one of the metals that lower the crystallization temperature most, owing to high a-Si solubility in it. Aluminum-induced crystallization of a-Si at temperatures as low as 120 °C has been reported [55].

In this work, we have used aluminum-induced crystallization of silicon to obtain polysilicon piezoresistors.

1.7 Accelerometers

An accelerometer is a device which is used to measure acceleration. It is composed of a spring system with a proof mass at the ends [56]. When it is subject to a force, the proof mass displaces due to simultaneous expansion and contraction of springs at the opposite ends which results in a displacement of the proof mass. By using capacitive or piezoresistive means, that displacement is converted to acceleration. The dynamics of an accelerometer could be described by a mass spring system as illustrated in Fig. 1.6 and is governed by Eq. 1.20 as given below:

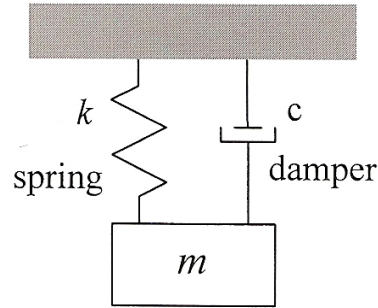


Fig. 1.6 Mass spring system showing the dynamic behavior of an accelerometer [57]

$$m \frac{d^2 x}{dt^2} + b_m \frac{dx}{dt} + k_m x = F_x(t) \quad (1.20)$$

where m is the mass, b_m is the damping coefficient and k_m is the spring constant [57].

1.8 Damping Force

In a real vibratory system, system movement is always restricted by dissipative forces such as air viscosity, friction and internal dissipation. The energy for the work is generally lost from the vibration energy in the form of thermal energy. Thus, damping could be described as a process where energy is taken from the system.

In the case of MEMS devices, there is a high interaction between structure and air. Therefore, viscous air damping is the most significant source for energy dissipation. This can happen in either as slide film damping or squeeze film damping or both [58, 59].

1.8.1 Slide Film Air Damping

Slide film damping occurs on laterally moving devices. Movement of a plate parallel to a fixed area will not change the pressure in the air gap underneath the plate and damping will take place due to gravity forces in the fluid [58]. The basic model of the slide film could be described as an infinite plate in a viscous fluid moving in the lateral directions as shown in Fig.

1.7.

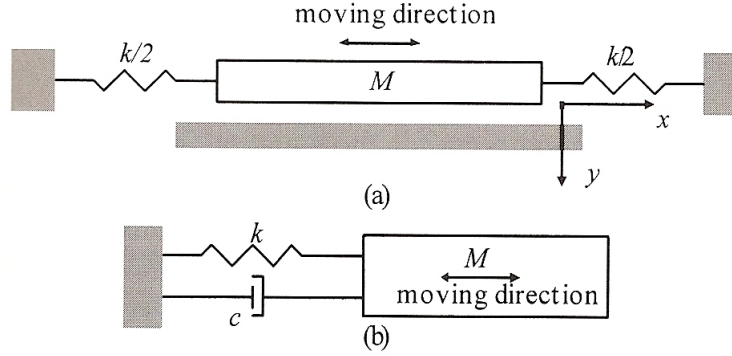


Fig. 1.7 Basic model of the slide film damping, showing the movement parallel to air film a) double spring representation b) single spring-damper representation [60]

The equation governing the steady flow of an incompressible fluid is the Navier-Stokes equation which is given as [60]

$$\rho \left[\frac{\partial \vec{v}}{\partial t} + (\vec{v} \cdot \nabla) \vec{v} \right] = \vec{F} - \nabla \rho + \mu \nabla^2 \vec{v} \quad (1.21)$$

where F is the force applied and μ is the coefficient of viscosity, ρ is the pressure and v is the velocity of the fluid where

$$\vec{v} = u \vec{i} + v \vec{j} + w \vec{k} \quad (1.22)$$

Assuming that the plate moves in the x-direction, Eq.19 could be simplified to

$$\frac{\partial u}{\partial t} + u \frac{\partial u}{\partial x} = \frac{\mu}{\rho} \frac{\partial^2 u}{\partial z^2} \quad (1.23)$$

If it is supposed that the structure is oscillating harmonically with respect to its rest position with $u(t) = a_0 \omega \cos \omega t = u_0 \cos \omega t$ where a_0 is the amplitude of oscillation, ω is the frequency, right and left sides of Eq.21 could be calculated separately leading to the definition of an “effective decay distance” which is given as

$$\delta = \sqrt{2\mu / \rho \omega} \quad (1.24)$$

Depending on the effective decay distance, two flow models, Couette and Stokes, can be defined.

Couette flow dominates if the oscillating frequency is low so that $\delta \gg d$ where d is the air gap between the plate and the substrate. In the case of Couette flow, velocity gradient on the top of the plate is zero so there is no damping force on the top and all the energy dissipated by damping takes place at the bottom.

If the effective decay distance is not too large compared with the gap, Couette flow model is invalid and Stokes model dominates. In the case of Stoke's flow, viscous forces dominate over inertial forces. Stoke's flow takes place if the viscosity of the fluid is very high, flow velocity and characteristic dimensions through which flow takes place, are very small [60]. In that case, the Reynolds number is less than 1. Reynolds number is a ratio of inertial to viscous forces and can be expressed as

$$\text{Re} = \frac{\rho VL}{\mu} \quad (1.25)$$

where ρ is the density of the fluid, V is the mean fluid velocity, L is the characteristic linear dimension and μ is the fluid viscosity.

1.8.2 Squeeze Film Air Damping

A plate separated from a fixed surface by a thin film of air will undergo squeeze film damping if it is moved towards the surface. As the plate moves, the air film is squeezed and an additional pressure is developed in the gap forcing air out of the gap as shown in Fig. 1.8. When the pressure is relieved, the pressure in the gap is reduced so that air can flow in. In either case the forces on the plate are against its movement and the work done by the plate is consumed by viscous flow and converted into heat. Since the air film acts as a damper, the process is called as squeeze film damping.

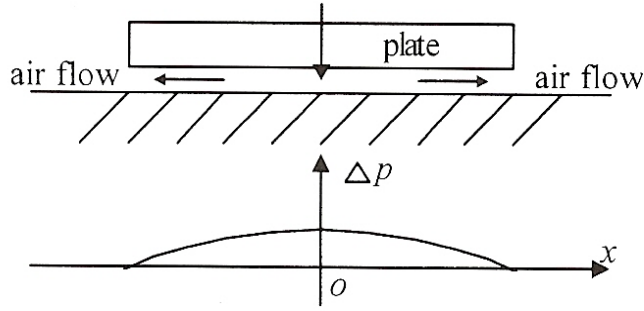


Fig. 1.8 Basic model showing the squeeze film damping behavior and pressure build up [60]

Squeeze film damping is a characteristic for capacitive MEMS devices where parallel plates are separated by a thin film of air. To increase the sensitivity, the distance between plates is preferred to be as small as possible, which results in a damping force.

Squeeze film damping has profound effects on the dynamics of the system and should be controlled to an expected level.

For a vibrating system, the free vibration frequency is given as

$$\omega_0 = \sqrt{\frac{k}{m}} \quad (1.26)$$

where k is the spring constant and m is the proof mass.

Another important frequency that is used in analyzing the damping effect is the cutoff frequency, which can be defined as the frequency when the elastic force equals the damping force and given by

$$\omega_c = \frac{\pi^2 h_0^2 p_a}{12 \mu w^2} \quad (1.27)$$

where h_0 is the film thickness, p_a is the ambient pressure; w is the width of the structure and μ is the coefficient of viscosity.

For MEMS devices such as high sensitivity accelerometers, the resonance frequency is low and $\omega_0 \ll \omega_c$. In this case, the coefficient of damping force is constant and the gas film is

assumed to be incompressible, i.e. the squeeze action is slow and there is enough time for the gas to leak. In that case the damping ratio is given as

$$\xi = c_{d0} / 2m\omega_0 \quad (1.28)$$

where ξ is the damping ratio and c_{d0} is the coefficient of damping force. A system under the above conditions is considered to be under damped if $\xi < 1$, over damped if $\xi > 1$ or critically damped if $\xi = 1$. A critically damped structure comes to rest almost instantaneously, without oscillating whereas it takes longer for an over damped system to come to rest. An under damped system continues to oscillate at its natural frequency. Optimum damping is obtained when $\xi \approx 0.7$ [60, 61].

1.9 Electroplating

Electroplating is a surface covering process where a metal is deposited on a conducting surface. It is based on the discharge of metal ions which are present in the electrolyte on the surface of cathode as demonstrated in Fig. 1.9. By taking an electron at the conducting cathode-electrolyte interface, metal ion deposits as metal atom on the conducting surface. The metal ion required for the process is either supplied by an electrolytic solution with metal salts added to it or by the dissolution of anode during the process.

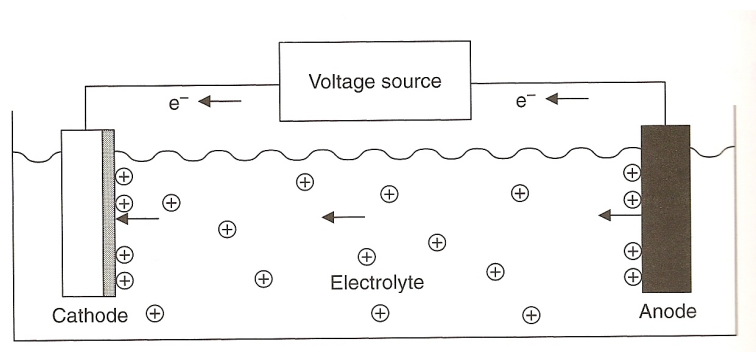


Fig. 1.9 Model showing the electroplating process [62]

Electroplating is a multi-stage process whereby the hydrated metal atom first diffuses through electrolyte to cathode. At the cathode, discharge of metal takes place and then via

surface diffusion nucleation of atoms on the metal surface takes place. In the final step, nuclei fuse together to form a continuous film as shown in Fig. 1.20 [62].

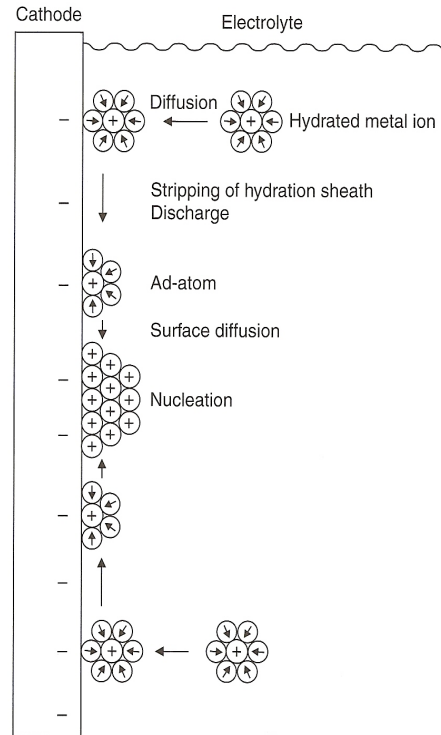


Fig. 1.10 Discharge, nucleation and continuous film formation on the cathode surface [62]

In this work, we have used electroplating to grow the mass and springs of accelerometer.

1.10 Summary

In this chapter, first an overview is given on failure assessment using MEMS sensors and on flexible substrates. Then, an introduction to pressure sensor is provided, followed by the general theory of piezoresistivity and piezoresistivity specifically in polysilicon. In this work, we have used aluminum-induced crystallization of silicon to obtain polysilicon piezoresistors. Thus, concept of aluminum-induced crystallization is discussed. Next, an introduction into capacitive

accelerometers is given followed by theory of damping, which is one of the most important parameters for MEMS devices. Finally, electroplating, which is one of the methods used in the accelerometer fabrication is explained.

CHAPTER 2

PIEZORESISTIVE MEMS PRESSURE SENSORS

2.1 Introduction

MEMS pressure sensors have found a lot of applications in fields such as automotive, aerospace [63] as well as in biomechanics [64] due to their low cost, low energy consumption and small size.

A typical MEMS pressure sensor is made up of a diaphragm which is supported on the edges. Based on detection method, the sensing could be employed either by using capacitance change or piezoresistivity.

Capacitive pressure sensors are based on the principle of parallel plate capacitance. With the applied pressure, diaphragm deflection takes place which changes the capacitance by changing plate separation. Capacitive pressure sensors have low temperature sensitivity, however, due to non-uniform diaphragm deflection, they have low linearity and they require complex readout circuitry [31].

Typically piezoresistive pressure sensors are composed of a diaphragm supported by bridge arms housing diffused, implanted or deposited piezoresistors based on the method of fabrication (Fig 2.1). The diaphragm acts as a stress amplifier where amplified stress is converted to resistance change by piezoresistors and that change is read in the form of voltage or current change. Piezoresistive pressure sensors are more linear compared with their capacitive counterparts; however, they have high temperature sensitivity [65]. This temperature sensitivity could be minimized by using Wheatstone bridge, provided that the resistances are equal [31]. Another advantage of piezoresistive pressure sensors is that the output could be read directly.

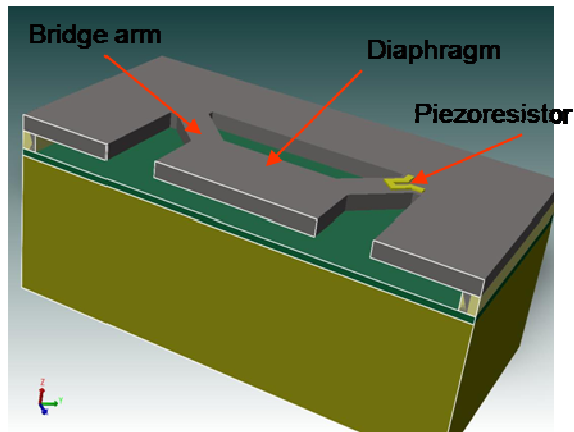


Fig. 2.1 Cross sectional view of a basic piezoresistive MEMS pressure sensor

This chapter explains design, fabrication and characterization of piezoresistive MEMS pressure sensor via surface micromachining.

2.2 Wheatstone Bridge

The circuit diagram of a Wheatstone bridge is shown in Fig. 2.2. Four resistors corresponding to the piezoresistors in a pressure sensor are denoted as R_1 , R_2 , R_3 and R_4 .

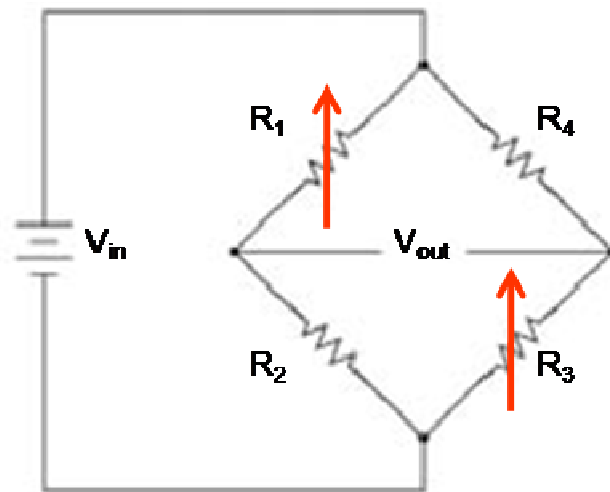


Fig. 2.2 Wheatstone bridge circuit diagram. Arrows on the diagram denote resistors in the active sensor area

For a given voltage input of V_{in} , the output voltage V_{out} of the bridge in Fig. 2.2 is given as

$$V_{out} = \frac{R_1 R_3 - R_2 R_4}{(R_1 + R_4)(R_2 + R_3)} V_{in} \quad (2.1)$$

When the bridge is balanced, i.e. $R_1 R_3 = R_2 R_4$ and $V_{out} = 0$. However, for an unbalanced bridge, there is a finite voltage output which is called as the offset voltage. Equation 2.1 is for zero applied pressure case. When pressure is applied, it can be rewritten as

$$V_{out} + \Delta V_{out} = \frac{(R_1 + \Delta R_1)(R_3 + \Delta R_3) - (R_2 + \Delta R_2)(R_4 + \Delta R_4)}{(R_1 + \Delta R_1 + R_4 + \Delta R_4)(R_2 + \Delta R_2 + R_3 + \Delta R_3)} V_{in} \quad (2.2)$$

Where ΔR_1 , ΔR_2 , ΔR_3 and ΔR_4 are fractional changes in resistance due to applied pressure and ΔV_{out} is the change in output voltage.

The diaphragm region, where deformation due to applied pressure takes place is called the active region and resistors in this region are called active resistors. Resistors which were placed outside active region are called passive resistors and they were not affected by the applied pressure. In Fig. 2.2, resistors R_1 and R_3 which are marked with red arrows are active and R_2 and R_4 are passive resistors. Considering that resistance change will only occur for active resistors, Eq. 2.2 reduces to

$$V_{out} + \Delta V_{out} = \frac{(R_1 + \Delta R_1)(R_3 + \Delta R_3) - (R_2)(R_4)}{(R_1 + \Delta R_1 + R_4)(R_2 + R_3 + \Delta R_3)} V_{in} \quad (2.3)$$

Assuming that all resistors are equal, and after rearrangement, Eq. 2.3 can be written as

$$\Delta V_{out} = \frac{\frac{\Delta R}{R}}{2 + \frac{\Delta R}{R}} V_{in} \quad (2.4)$$

considering a half Wheatstone bridge, where $\Delta R/R$ is the normalized resistance change.

2.3 Design

Computer analysis of devices for optimization and performance is an important part of MEMS fabrication flow, as these could help to increase device performance and eliminate design and calculation errors. For this purpose, Coventorware™ has been used to design, optimize and analyze various pressure sensors through finite element analysis.

As a first step, two dimensional system layouts were created, which then were transferred into three dimensional solid models through a process flow. Twenty one pressure sensor structures composed of square membranes were created. Details of these sensors are given in Appendix A. Each membrane was supported by four bridge arms on the corners, housing two piezoresistors in a half Wheatstone bridge configuration as shown in Fig. 2.3. Structures differed in terms of membrane size and shape, bridge arm dimensions and piezoresistor shapes and dimensions. Considering the isotropic etching of the sacrificial polyimide during actual fabrication, an equal undercut length from the edges of trenches in both directions were determined to suspend the membrane.

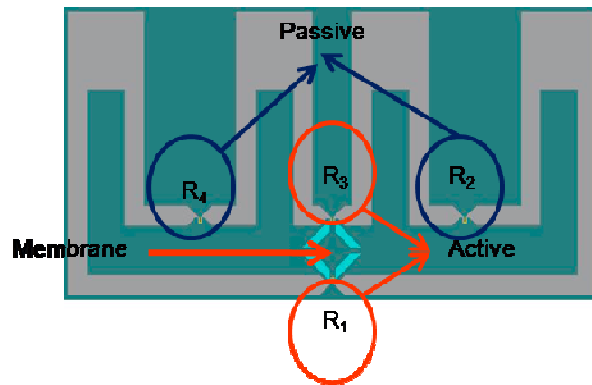


Figure 2.3 Piezoresistive pressure sensors in half Wheatstone bridge configuration

Si₃N₄ was the material choice for membrane due to its high strength, hardness, elasticity and linearity [66]. Polysilicon has been chosen as the piezoelectric material due to its high gauge factor [44]. Material properties for simulations were tabulated in Table 2.1. For simulation purposes, all materials were assumed to be linear, elastic and isotropic.

Table 2.1 Material properties used for simulations [67, 68]

Material	Young's Modulus (GPa)	Poisson's Ratio
Si ₃ N ₄	222	0.27
Polysilicon	160	0.22

For the simulations, extruded brick was used for meshing. In the extruded brick, meshing is first applied on the x, y axes and then extended into the z axis. Finding the right mesh size is important in finite element analysis to avoid erroneous results. Thus, initially a convergence analysis for displacement has been performed starting with a high mesh size and then gradually decreasing it until two consecutive displacement values converge.

Simulations were performed using MemMech module of Coventorware™ by applying uniform pressure of 50 kPa on top of whole surface after meshing and constraining the sides of the membrane as shown in Fig. 2.4. During the simulations, maximum stress is observed at maximum membrane displacement. Initially, simulations were done without placing the piezoresistors to determine the maximum strain regions for optimum placement and piezoresistor dimensions (Fig.2.5). Then U or Y-shaped piezoresistors were placed and simulations were repeated (Fig.2.6). The type and dimensions of the piezoresistor were determined according to the stress distribution on the membrane arms.

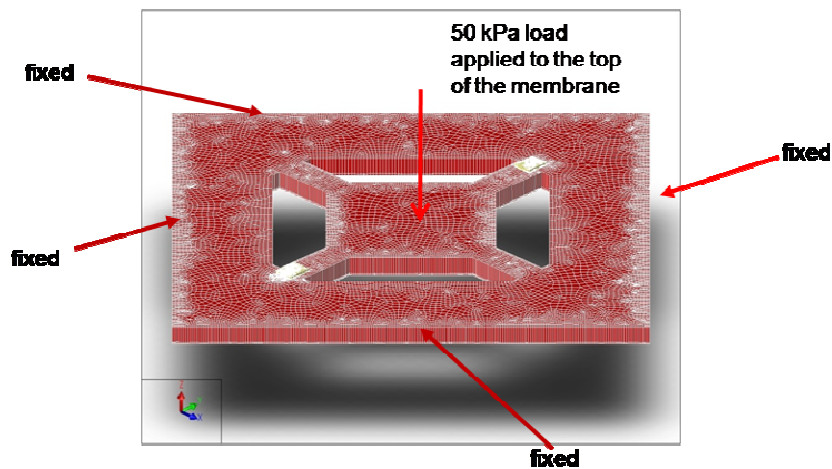


Figure 2.4 Boundary conditions for pressure sensor simulations

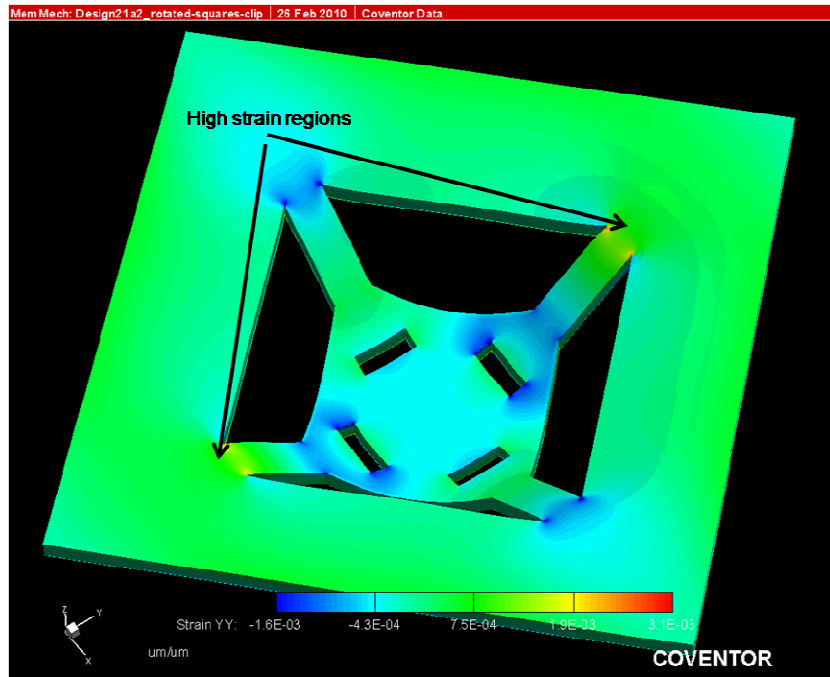


Figure 2.5 Displaced membrane to determine high strain region

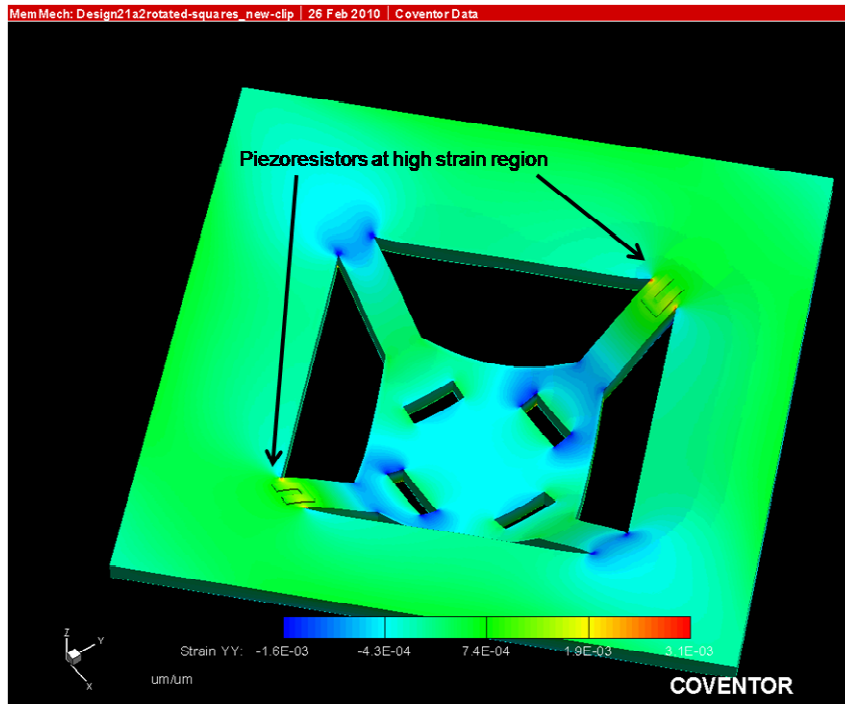


Figure 2.6 Piezoresistors at high strain region of displaced membrane

After the simulations, post simulation calculations were performed to find values such as average strain, $\Delta R/R$ and ΔV_{out} . To calculate average strain, U-shaped piezoresistors were divided into three regions and Y-shaped piezoresistors were divided into five regions to calculate transverse (ε_{xx}) and longitudinal (ε_{yy}) strains. Axis transformation was applied for Y-shaped piezoresistors using

$$\varepsilon_x = \varepsilon_{xx} \cos^2 \theta + \varepsilon_{yy} \sin^2 \theta + \gamma_{xy} \sin \theta \cos \theta \quad (2.5)$$

where, ε_{xx} , ε_{yy} and γ_{xy} are transverse, longitudinal and shear strains respectively. The angle θ is the angle between the global axis and the transferred axis. Using the strain data, the average strain was calculated using

$$Strain_{AVG} = \frac{Strain_{total}}{Area_{total}} = \frac{\iint [\varepsilon_{xx} + \varepsilon_{yy}] dx dy}{\iint dx dy} \quad (2.6)$$

Using the calculated average strain value, the normalized change in resistance was found assuming a gauge factor (GF) of 50 for polysilicon [32] and using

$$\frac{\Delta R}{R} = Strain_{AVG} * GF \quad (2.7)$$

Finally, differential output voltage was calculated considering an input voltage of 1 V and assuming half Wheatstone structure, using Eq. 2.4.

As a result of simulations and analysis, ten devices showing the best performance were selected for fabrication. Using the selected devices, a four mask layout was prepared using Coventorware™. Simulation settings, mask layouts and calculations are given in detail in Appendix B.

2.4 Fabrication

Fabrication of the pressure sensors was performed on 4 inch Si (100) and flexible polymer substrates by using surface micromachining techniques. Polyimide has been the material of choice to serve as sacrificial layer as well as flexible substrate. Prior to fabrication, wafers were cleaned in 3:1 H₂SO₄:H₂O₂ and 6:1 BOE followed by DI water rinse and

dehydration bake at 100 °C for 5 minutes. Before each fabrication step, wafers were cleaned in acetone and methanol, followed by DI water rinse and dehydration bake. Sputtering at room temperature was used for thin film deposition while etch and lift-off techniques were used to create structures. All sputtering was done using AJA ATC Orion series UHV sputter system and photolithography was performed using OAI Model806 i-line contact aligner. For DRIE, Trion DRIE system was used.

Fabrication started with sputter deposition of Si_3N_4 layer of 0.4 μm on Si (100) wafer to serve as a passivation and planarization layer. Si_3N_4 deposition was done at room temperature under 30 sccm Ar and 5 sccm N_2 gas flow at a pressure of 2.8 mTorr using 150 W RF power. To fabricate pressure sensors on Si substrate, next 3.1 μm of PI 2611 (HD Microsystems) polyimide sacrificial layer was spin coated at 5000 rpm for 30 seconds followed by hot plate bake at 110 °C for 5 minutes and cured at 380 °C for 8 hours in nitrogen gas environment with a ramp up and ramp down rate of 1.5 °C/min. Then, 1.9 μm of Si_3N_4 layer was sputter deposited to create the membrane layer. Following membrane deposition, NR-71 6000 P (Futurrex) negative photoresist was spin coated and patterned to serve as a mask layer for DRIE. Trench opening was done using DRIE with RIE and ICP powers of 30 and 3500 W respectively at CF_4 flow of 25 sccm and 25 mTorr pressure by etching Si_3N_4 all the way through as shown in Fig.2.7.

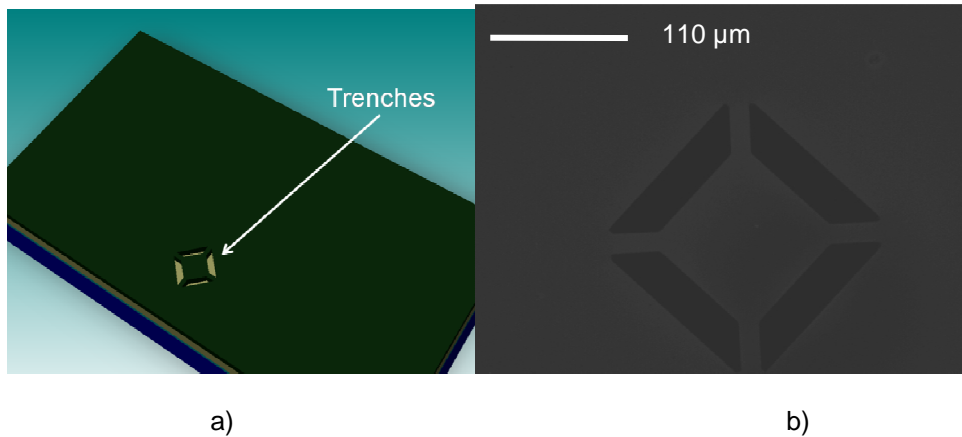


Figure 2.7 Trench opening on Si_3N_4 membrane a) simulated b) fabricated

Following trench opening, NR-9 1500 PY (Futurrex) negative resist was spin coated and patterned followed by stacking of Al and a-Si layers of 0.5 μm each on top of each other. Aluminum was sputtered at 2.8 mTorr using 150 W DC power at 30 sccm Ar flow followed by deposition of a-Si at a pressure of 6 mTorr using an RF power of 150 W in 30 sccm Ar gas flow. Lift-off to define piezoresistors was done in acetone followed by rapid thermal anneal at 500 $^{\circ}\text{C}$ for 1.5 hours to crystallize piezoresistors through aluminum induced crystallization as shown in Fig.2.8 [69]. The residual Al remaining after layer exchange was etched for 2 minutes at 55 $^{\circ}\text{C}$ in Al-etch, prepared by mixing 80 % H_3PO_4 , 10 % H_2O , 5 % HNO_3 and 5 % CH_3COOH . Next, 0.5 μm Al metallization was deposited and patterned by lift-off using NR-9 1500 PY photoresist followed by deposition and patterning of Al bond pads of same thickness as illustrated in Fig.2.9. Finally, oxygen plasma ashing of sacrificial polyimide at a pressure of 0.65 mbar using 150 W power was performed to obtain suspended pressure sensors as shown in Fig.2.10. To fabricate pressure sensors on flexible substrate, six layers of PI 5878G (HD Microsystems) polyimide to serve as flexible substrate were spin coated on top of first Si_3N_4 layer at 1500 rpm for 60 seconds followed by 110 $^{\circ}\text{C}$ bake for 5 minutes after each layer. Curing was done in nitrogen

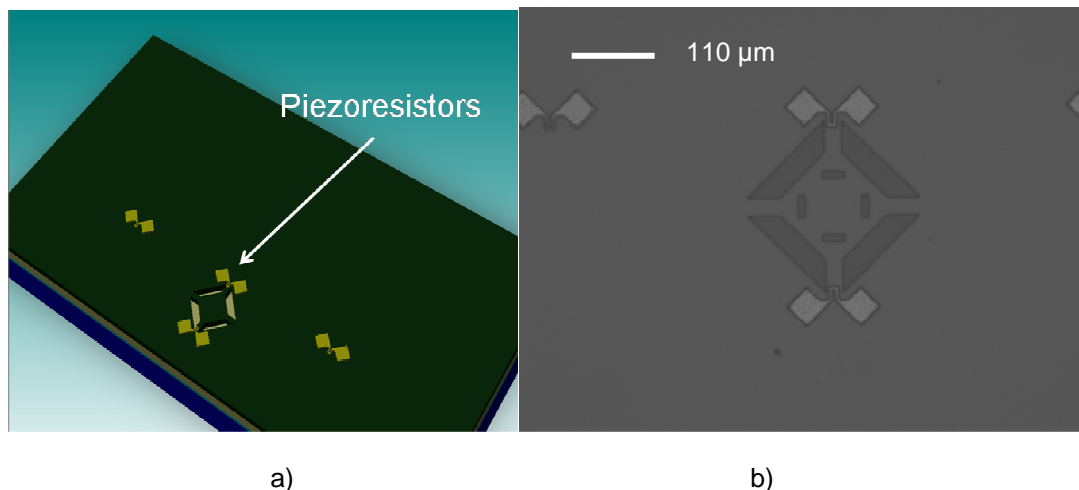


Figure 2.8 Fabrication of piezoresistors a) simulated b) fabricated

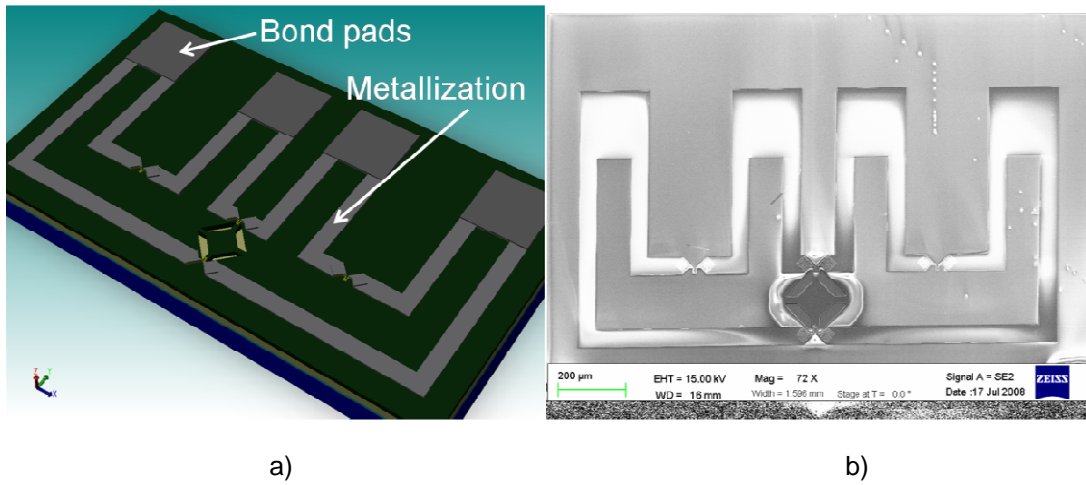


Figure 2.9 Fabrication of metallization layer and bond pads a) simulated b) fabricated

gas by ramping up the temperature to 390 °C (1.2 °C/min ramp rate) with a dwell time of 6 hours followed by ramp up to 450 °C in 1 hour and keeping it there for 4 hours. At the end of the dwell time, temperature was brought down with a ramp rate of 1.2 °C/min. Then a second layer was deposited on flexible substrate to passivate it from other layers. Next, One layer of PI 5878 G was spin coated at 5000 rpm for 60 seconds to serve as sacrificial layer and cured under the

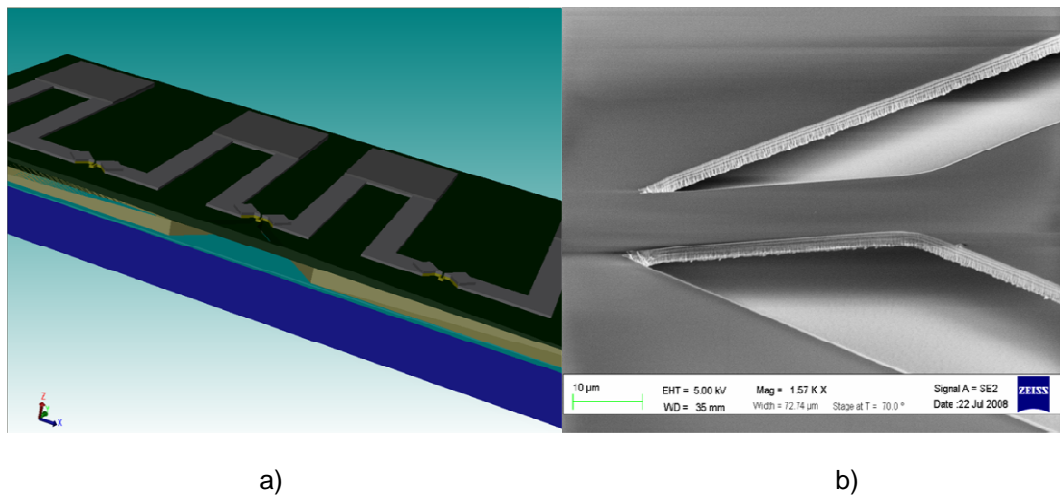


Figure 2.10 Illustration of the undercut after ashing a) simulated b) fabricated

same conditions as flexible substrate layer. Before depositing membrane, LOR B15 (Microchem) was spin coated at 2000 rpm for 45 seconds followed by hot plate bake at 150 °C for 2 minutes to act as undercut resist. Then S1813 (Shipley) positive photoresist was spin coated and patterned. After the deposition of membrane, trenches were opened by lift-off in acetone. All subsequent processes were the same as before. Details of all resist processes are given in Table 2.2.

Table 2.2 Process details of photoresists that were used in pressure sensor fabrication

Resist	Spin Coating		Exposure Energy (mJ/cm ²)	Resist Bake (°C)		Development Time (sec)	Resist Thickness (µm)
	RPM	Duration (sec)		Pre-bake	Post-bake		
NR-9 1500PY	2500	40	313.6	170	113	8	1.76
NR-71 6000P	1500	40	383.7	170	113	135	14
S 1813	2000	30	78.4	128	none	120	1.6

2.5 Characterization

2.5.1. I-V Measurements

I-V characterizations were performed by probing bond pads and sweeping current between negative and positive 5×10^{-6} A using Agilent 4155C semiconductor parameter analyzer connected to a probe station. Resistance notation and equivalent circuit diagram are given in Fig. 2.3 and Fig. 2.2, respectively.

During I-V characterization, the whole Si wafer was scanned to identify working devices and twelve of those among many, which were showing relatively close resistance values within were taken as samples for further characterization. I-V characterizations were performed before and after packaging the samples. Results of I-V characterizations are given in Appendix C.

The resistance values for bonded devices, which were found from the slope of I-V charts by assuming a linear fit, are tabulated in Table 2.3. Resistances are denoted as total resistance since each direct measurement gives the resistance of the measured one in parallel with the series connection of other three. Then using a MathCAD code, actual resistance values were calculated as shown in Table 2.4.

Table 2.3 Resistance values measured from the slope of I-V charts assuming linear fit

	R1Total (kΩ)	R2Total (kΩ)	R3Total (kΩ)	R4Total (kΩ)
Sample 1	45.6	169.2	204.1	60.9
Sample 2	57.5	59.3	84.0	60.0
Sample 3	60.0	64.2	25.4	32.6
Sample 4	454.2	190.1	328.0	286.8
Sample 5	38.9	76.1	149.7	38.9
Sample 6	43.0	61.7	87.2	43.0
Sample 7	277.9	182.4	503.7	295.4
Sample 8	246.9	156.4	416.2	268.0
Sample 9	233.6	527.5	475.6	158.8
Sample 10	270.0	161.1	227.0	270.9
Sample 11	196.2	83.9	192.0	133.2
Sample 12	239.9	147.2	85.5	60.9

Table 2.4 Individual resistance values, which are calculated using MathCAD

	R1 (kΩ)	R2 (kΩ)	R3 (kΩ)	R4 (kΩ)
Sample 1	48.4	234.8	491.0	66.0
Sample 2	72.0	75.0	134.6	76.2
Sample 3	91.5	108.1	28.4	38.0
Sample 4	832.6	215.4	428.0	356.0
Sample 5	39.4	77.8	3438.0	39.4
Sample 6	50.2	80.1	168.6	50.2
Sample 7	331.5	202.4	1157.0	357.9
Sample 8	301.4	174.7	854.1	335.6
Sample 9	267.2	968.8	718.0	172.8
Sample 10	389.9	189.4	296.2	392.3
Sample 11	304.9	94.3	291.0	165.2

Table 2.4 – *Continued*

Sample 12	891.1	171.4	92.6	64.3
------------------	-------	-------	------	------

Then, using Eq. 2.1 together with calculated resistances; offset voltages for each sample were calculated for 1 V DC input.

Table 2.5 Comparison of calculated and measured offset voltages for 1 V DC bias. Sample 8 was measured applying 3 V DC bias.

	Calculated Offset Voltage (mV)	Measured Offset Voltage (mV)
Sample 1	99.5	436.8
Sample 2	127.9	203.0
Sample 3	85.5	96.6
Sample 4	365.7	156.0
Sample 5	477.9	425.0
Sample 6	178.3	369.0
Sample 7	332.0	311.7
Sample 8	910.0	986.0
Sample 9	32.9	55.0
Sample 10	108.4	200.0
Sample 11	403.9	28.0
Sample 12	283.4	566.7

2.5.2. Response Measurements

The setup to measure pressure sensor response is illustrated in Fig. 2.11. For the measurements, first offset voltage was measured without applying any load to the membrane. Offset voltage measurements were performed for four different configurations which were obtained by switching input and output ports as well as input source polarity. The configuration showing lowest offset value was used for further measurements. At the input port, a potential

difference of 1 V was applied using Agilent E3620A DC voltage supply and measurements were taken using Keithly 2182A Nanovoltmeter at the output port.

Probe to apply pressure to the center.

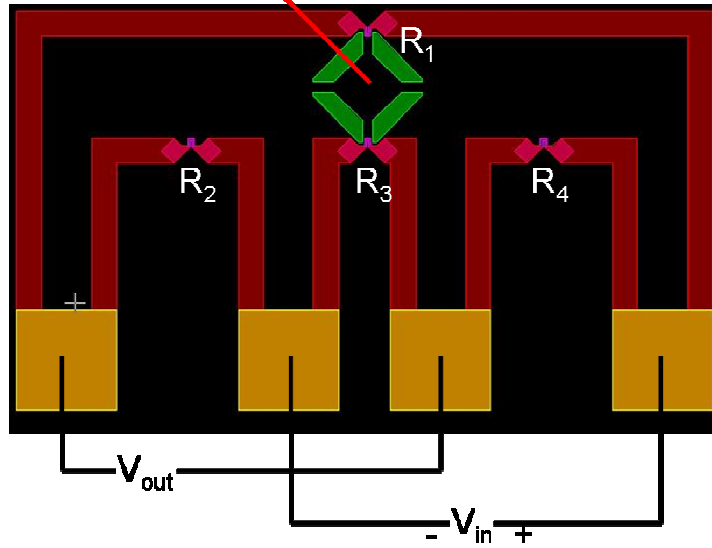


Figure 2.11 Illustration of the setup to measure pressure sensor response

To determine device response, membrane was fully deflected until it touched the bottom and output voltage was measured. Differential voltage output was calculated by subtracting the offset voltage values from the deflected ones. As shown in Table 2.6, a maximum voltage difference of 13.7 mV was obtained at full deflection for an input voltage of 1 V.

Table 2.6 Differential output voltage and voltage response values in response to 1 V input. For Sample 8, 3 V input was applied.

	V_{offset} (mV)	V_{out} (deflected) (mV)	ΔV (mV)
Sample 1	436.8	433.8	3.0
Sample 2	203.0	210.0	7.0
Sample 3	96.6	105.3	8.7
Sample 4	156.0	165.0	9.0
Sample 5	425.0	433.0	8.0
Sample 6	369.0	378.0	9.0
Sample 7	311.7	316.8	5.1

Table 2.6 – Continued

Sample 8	986.0	961.0	25.0
Sample 9	55.0	52.0	3.0
Sample 10	200.0	186.3	13.7
Sample 11	28.0	35.0	7.0
Sample 12	566.7	563.7	3.0

2.5.3. Gauge Factor Calculations

Gauge factors of measured samples were calculated using response measurement results in combination with simulations.

In Section 2.5.2, it was mentioned that the membrane was fully displaced during response measurement, which corresponds to a distance of 3.1 μm . This statement was confirmed by ripping off a membrane and profiling the surface using Alpha-Step stylus profilometer as shown in Fig. 2.12. Then, using CoventorwareTM, computer models of measured samples were displaced by 3.1 μm as shown in Fig. 2.13. Different from the previous simulations, in this case, pressure was applied only on a node created at the center of the membrane, rather than the whole membrane surface. That approach was implanted with the purpose of replicating membrane deflection using a probe. Pressure values shown in Fig. 2.13 are only simulation settings which were required to displace each structure by 3.1 μm .

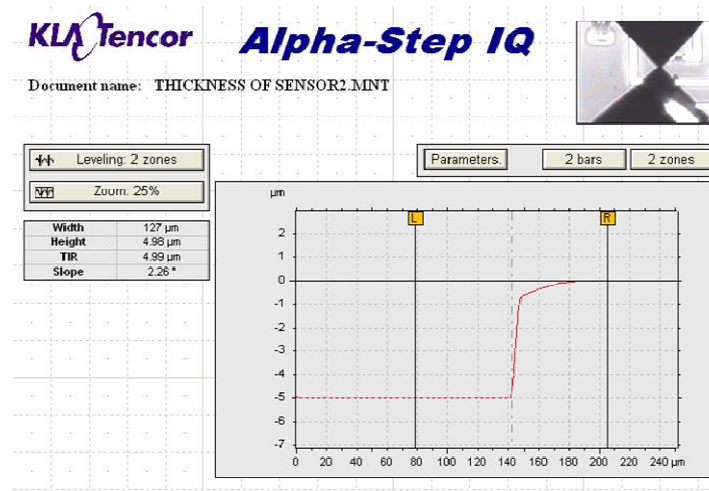
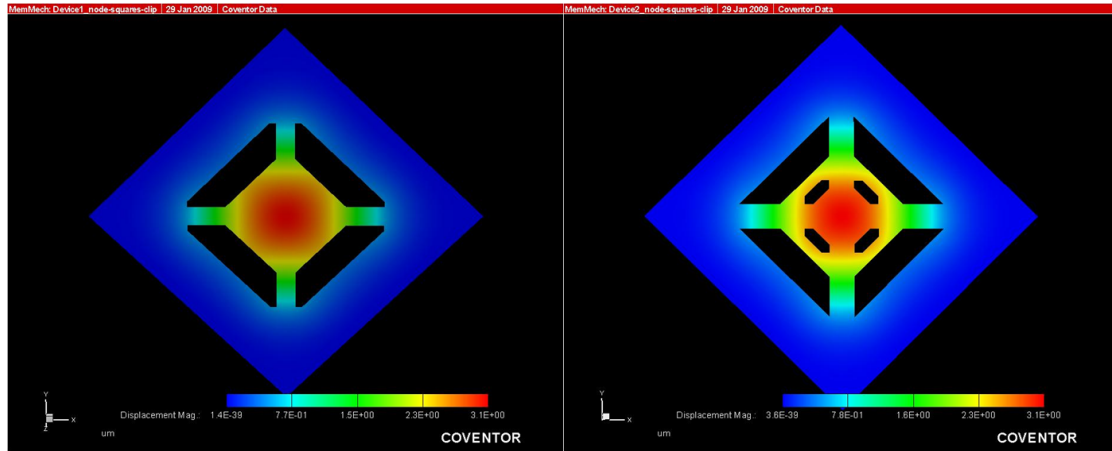
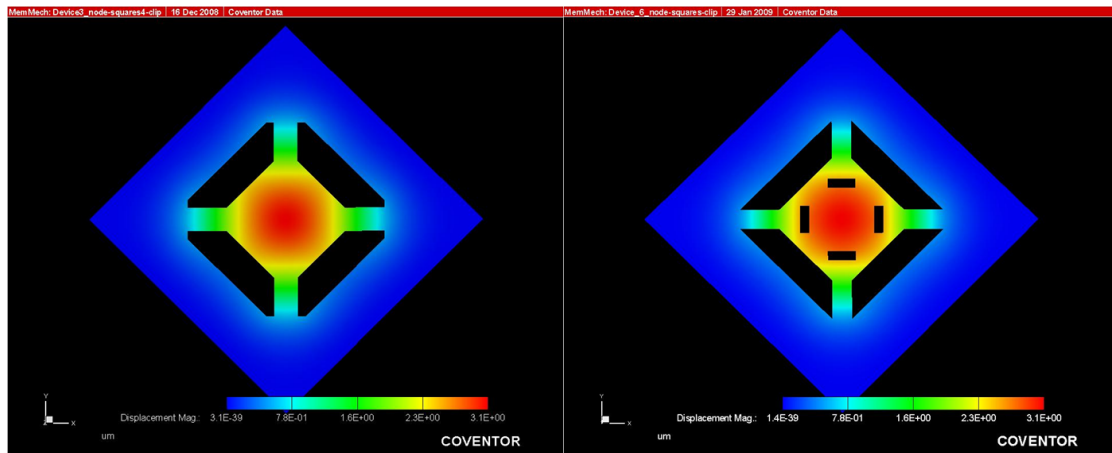


Figure 2.12 Surface profile through a ripped off membrane. The 5 μm gap is formed by the sacrificial layer of 3.1 μm and membrane with a thickness of 1.9 μm .



a)

b)



c)

d)

Figure 2.13 Simulation results for membranes displaced by $3.1 \mu\text{m}$ to determine average strain on piezoresistors. Pressures given are the values required to displace membrane by $3.1 \mu\text{m}$. Output voltages and resistance changes were calculated assuming a gauge factor of 50 and input voltage of 1 V. a) $P=78 \text{ MPa}$, $\epsilon_{\text{AVG}}=7.05 \times 10^{-4}$, $\Delta R/R=3.52 \%$, $V_{\text{out}}=17.30 \text{ mV}$ b) $P=120 \text{ MPa}$, $\epsilon_{\text{AVG}}=9.9 \times 10^{-4}$, $\Delta R/R=4.95 \%$, $V_{\text{out}}=24.15 \text{ mV}$ c) $P=128 \text{ MPa}$, $\epsilon_{\text{AVG}}=9.46 \times 10^{-4}$, $\Delta R/R=4.73 \%$, $V_{\text{out}}=23.10 \text{ mV}$ d) $P=73 \text{ MPa}$, $\epsilon_{\text{AVG}}=7.53 \times 10^{-4}$, $\Delta R/R=3.76 \%$, $V_{\text{out}}=18.45 \text{ mV}$

After simulations, strain analysis was performed as explained in Section 2.3, to calculate average strain. Next normalized change in resistance, $\Delta R/R$, was calculated using Eq. 2.4 by substituting measured ΔV_{out} values into equation. For this calculation, it was assumed that all resistances are the same. Finally, gauge factor was calculated using Eq. 2.7, by dividing normalized resistance change by average strain. Calculated values are given in Table 2.7.

Table 2.7 Actual gauge factor values calculated using measured differential output voltages.

Sample	Actual Gauge Factor
1	6.360
2	19.998
3	18.533
4	24.121
5	22.878
6	25.764
7	13.615
8	17.766
9	6.079
10	29.366
11	14.903
12	7.992

2.6 Summary

MEMS pressure sensors were designed and simulated for performance, fabricated using surface micromachining and characterized. For design purposes, elastic, linear and isotropic material characteristics as well as equal resistances were assumed. Simulated and fabricated devices showed a lot of variations, mainly due to deviations from simulated structures during fabrication caused by photolithography instabilities such as incorrect exposure and development, misalignment as well as non-uniformities during deposition or residual stress formed during high temperature processes.

Initial I-V characterizations showed non-linear behavior. This was attributed to temperature coefficient of resistance which in general can be expressed as

$$\beta = \frac{dR}{R} \left(\frac{1}{R} \right) \quad (2.8)$$

where R is the resistance at a given temperature and β is the temperature coefficient of resistance [70]. When current is applied, piezoresistors heat up due to Joule heating resulting in non-linear I-V characteristics. Although this approach seems to be correct initially, it should be noted that active resistors R_1 and R_3 are sitting on a low thermal conductivity air pocket (0.025 W/m.K) while passive resistors R_2 and R_4 are fabricated on top of relatively higher thermal conductivity PI2611 sacrificial polyimide layer (0.105 W/m.K) practically acting as heat sink. From this consideration, it is expected that only the active piezoresistors would show non-linear I-V characteristics while passive ones show relatively linear behavior. However, this is not the case which indicates that nonlinearity is due to Schottky type contact between semiconducting polysilicon and Al rather than ohmic.

The response measurements of selected samples gave a maximum voltage output change of 13.7 mV. Gauge factor values, which were calculated using measured differential output voltages in combination with Coventorware™ simulations resulted in a maximum value of 29.4, which was lower than the assumed value of 50. This was expected considering the low temperature fabrication of polysilicon, which results in low doping concentrations as well as fine grain size [71], as the gauge factor of polysilicon is reported to be highly microstructure and doping concentration dependent [44].

CHAPTER 3

CAPACITIVE MEMS ACCELEROMETERS

3.1 Introduction

MEMS accelerometers are found in many applications such as airbag triggers in cars, earthquake detection circuits, toys, cameras and cell phones [72].

As explained in Section 1.7, MEMS accelerometers are composed of a spring and damper system with a proof mass at the end. The sensing elements can be capacitive [73], piezoresistive [74] or piezoelectric [75]. Although each technique has its advantages and disadvantages, capacitive sensing is mostly preferred due to its high sensitivity, low drift, good noise performance, simplicity and low temperature sensitivity [74, 76].

For a capacitive accelerometer, acceleration is detected by the change in capacitance. This is achieved by displacement of a moveable capacitor plate with respect to its stationary counterpart.

The sensitivity of an accelerometer is based on its displacement. High displacement and high sensitivity values are achieved for large mass and low spring constant. Under these conditions, the resonance frequency of the accelerometer is low and the displacement is directly proportional to the acceleration following:

$$x \approx \frac{g}{\omega_0^2} \quad (3.1)$$

where x is the displacement, g is acceleration and ω_0 is the resonance frequency [77]. Large mass also decreases the noise floor [78] by decreasing the noise caused by Brownian motion [79].

This chapter explains design, fabrication and characterization of capacitive MEMS accelerometers on silicon and flexible polymer substrates.

3.2 Design

Using Coventorware™, six different devices were designed to measure acceleration in three axes. Two of them were designed to measure acceleration in z-axis while others, including three single axis and one dual axes, were designed for lateral sensing. Properties of designed accelerometers are given in Appendix D. Vertical axis accelerometers were composed of parallel plate capacitors and four springs to support the proof mass. Basic structure of the z-axis accelerometer is illustrated in Fig. 3.1.

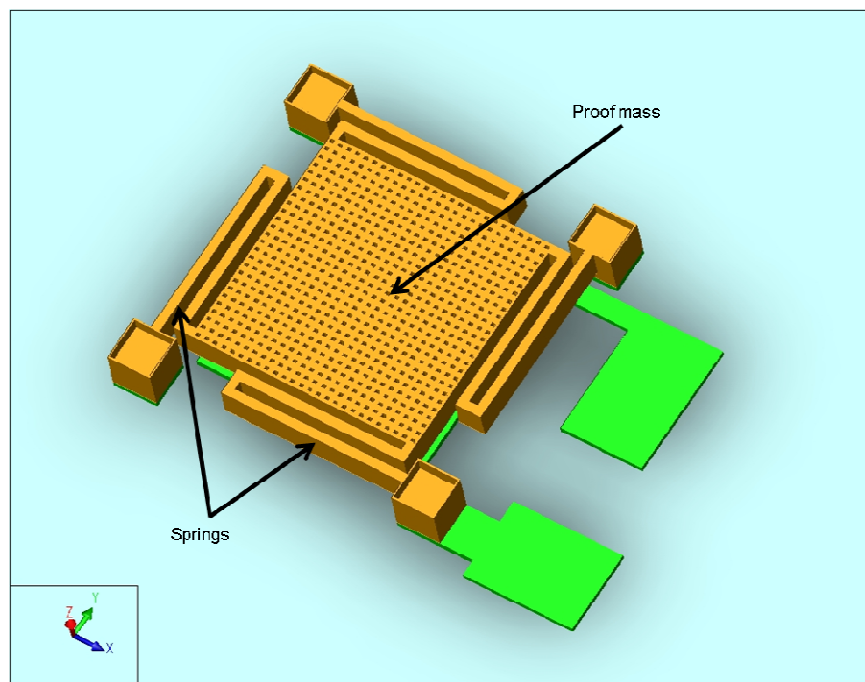


Fig. 3.1 Z-axis accelerometer supported by four springs

To measure acceleration in x,y-axes, differential capacitance was used. Differential capacitance is provided by combs which are moving between fixed ones. Moving combs were attached to the proof mass, which was supported by two springs. Basic structure of the lateral accelerometer is shown in Fig 3.2. Devices differed in mass in the case of the z-axis accelerometer and both in mass and number of combs to measure capacitance, in the case of the x, y-axes ones.

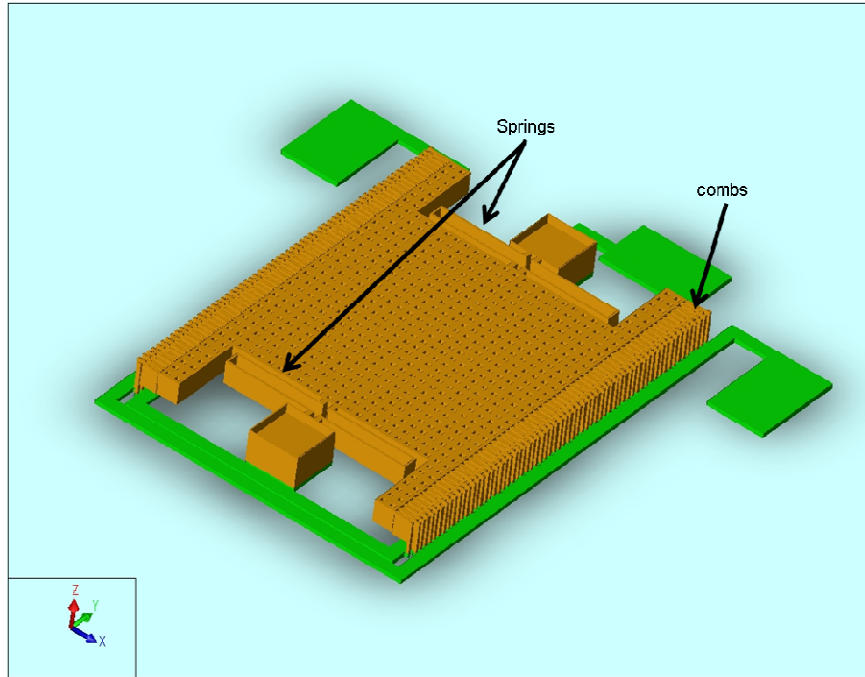


Fig. 3.2 Basic lateral axis accelerometer structure

The material of choice for the proof mass was nickel due to its high density and resistance to corrosive environmental conditions [80]. Ni properties that were used for simulations are given in Table 3.1. As metal interconnects, Al was used. All materials were assumed to be linear, elastic and isotropic.

Table 3.1 Properties of Ni used in simulations

Material	Young's Modulus (GPa)	Poisson's Ratio
Ni	220	0.3

For all simulations, meshing was done using manhattan brick. In the manhattan brick, mesh is applied uniformly in all global directions and for each direction, different mesh sizes can be applied.

Simulations were done using SpringMM, InertiaMM, DampingMM and CoSolveEM modules of Coventorware™. CoSolve couples MemMech and MemElectro to determine

capacitance while acceleration is applied to the device. First, using InertiaMM, proof mass simulations were performed assuming steady mass. For proof mass simulations, a solid model was created only for the proof mass. Then, spring constant simulations were performed using SpringMM, by creating a solid model for the spring only and displacing one end in the direction of sensing with the other end fixed. Spring constant values were also determined from simulation results using

$$k = \frac{m \times g}{x} \quad (3.2)$$

where k , m , g and x are the spring constant, proof mass, gravitational acceleration and displacement, respectively. Since from the simulations the spring constant was found for a single spring, to calculate it for the whole system, series and parallel spring calculations were performed where necessary. Overall spring constant for springs in series and in parallel were calculated using

$$\frac{1}{k} = \frac{1}{k_1} + \frac{1}{k_2} + \Lambda + \frac{1}{k_n} \quad (3.3)$$

and

$$k = k_1 + k_2 + \Lambda + k_n \quad (3.4)$$

respectively [81]. For z-axis, spring constant was calculated to be around 10 N/m while for x, y-axes it was found to be around 24 N/m. Spring constant values calculated from displacement were compared with simulated values. For lateral axes, both values were in agreement, however, for z-axis, a slight difference was seen which can be attributed to lack of the rotational component of spring constant consideration in the simulations [82].

For each device, resonance frequency was calculated using Eq. 1.26 which was introduced in Section 1.7 of Chapter 1. Resonance frequencies on the order of tens of kilohertz were calculated.

Damping simulations were performed using DampingMM module, for -40 °F, 60 °F and 160 °F temperatures considering the harsh operation environment of devices for aerospace applications. Air was used as the fluid medium. To reduce the thermal noise of sensors and obtain optimum performance, an under damped damping ratio of 0.6-0.7 was aimed [77]. For the z-axis sensors, only squeezed film damping was considered, due to squeeze effect of air with the movement of top plate towards bottom. Slide film damping on the sides of the top plate was ignored considering the high aspect ratio of the device. Both squeezed film and slide film damping were taken into account for lateral sensors. For the squeezed film damping, the combs were considered and for slide film damping only bottom surface of the proof mass was taken into account due to infinite opening at the top. Optimization of damping ratio for the desired value was achieved by changing the numbers and sizes of perforations in the case of z-axis sensors. For z-axis accelerometers, damping ratio increased with decreased size and number of perforations. In the case of lateral sensors, damping was optimized by changing the comb length due to dominance of squeezed film damping over slide film. In this case, damping ratio was directly proportional to the effective comb length, i.e. the length contributing to the capacitance. The devices were designed in such a way that at 60 °F, damping ratio was 0.65. Damping ratio simulations at other temperatures were done by modifying the pressures according to ideal gas law assuming constant volume. Since damping simulations give coefficient of damping force, damping ratio was calculated using

$$\xi = c_{d0} / 2m\omega_0 \quad (3.5)$$

where ξ is the damping ratio and c_{d0} is the coefficient of damping force and m is the final mass after device modification in order to obtain the desired damping ratio.

Finally, capacitance simulations were run to determine the sensor performance. For all sensors, initially rest capacitance was found by applying 1g acceleration in negative z-axis, e.g. in the direction of Earth's gravitational field. Then, additional 1g acceleration was applied in the sensing direction. For lateral sensors, 1g in the negative z-axis was kept during all capacitance

simulations considering Earth's gravitational field. Capacitance change was calculated directly by subtracting the rest capacitance from the results in increased acceleration simulations. As a result of capacitance simulations, information on the displacement of the structure was obtained as well, as shown in Figs. 3.3 and 3.4. Displacement values on the order of 10^{-2} $\mu\text{m/g}$ were observed. The layouts, settings used in all simulations as well as simulation results are given in Appendix E.

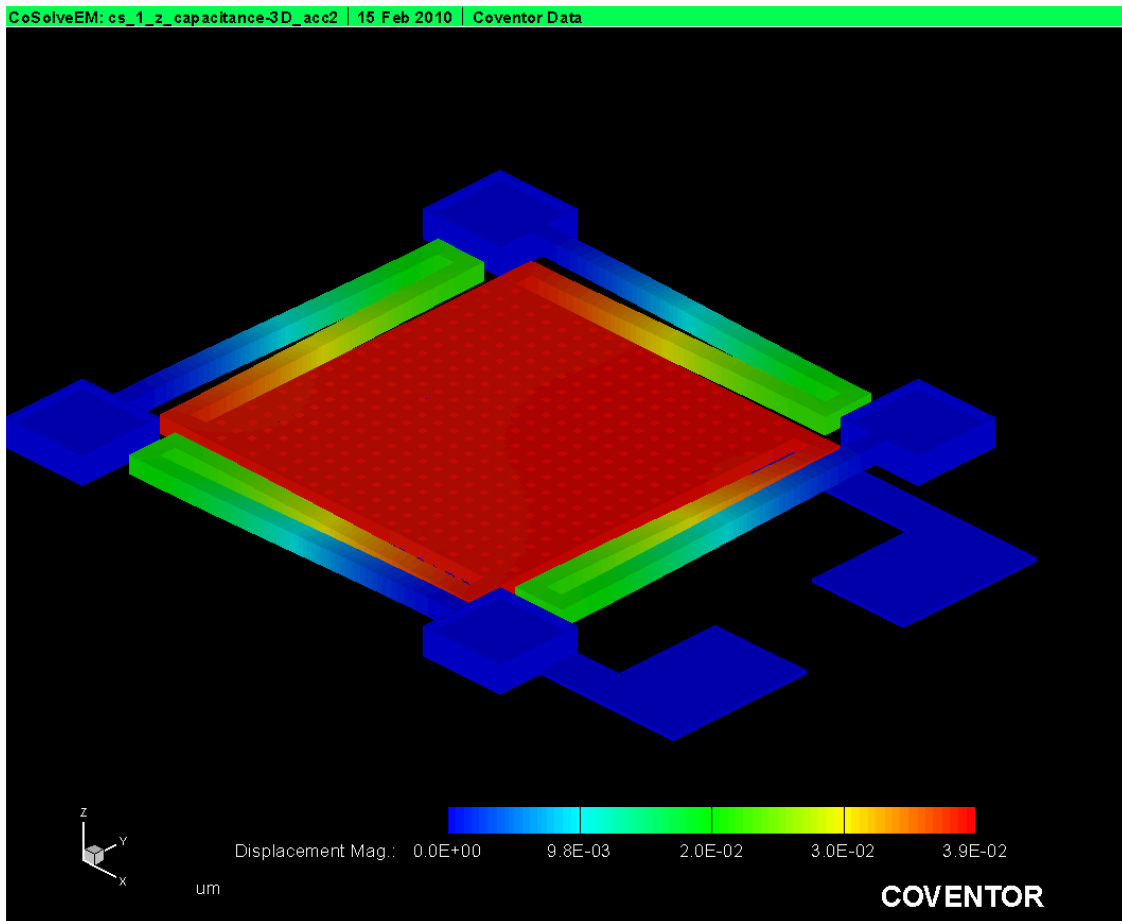


Fig. 3.3 Illustration of displacement for z-axis accelerometer for 1g acceleration in the sensing direction

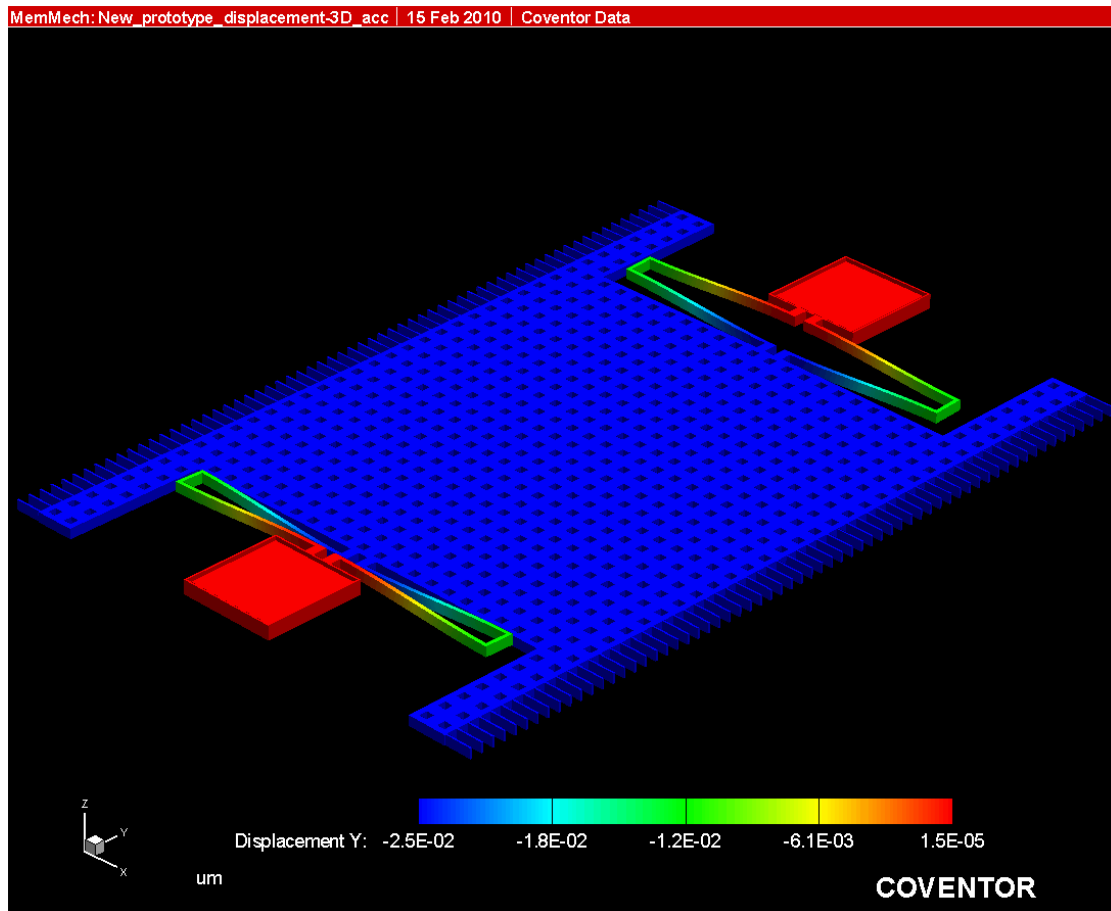


Fig. 3.4 Illustration of displacement for lateral axis accelerometer for 1g acceleration in the sensing direction

3.3 Fabrication

Surface micromachining is used to fabricate the accelerometers on a flexible polymer and 4 inch Si (100) substrates. Prior to fabrication, wafer cleaning was done as explained in Section 2.4.

Accelerometer fabrication on the flexible substrate started with the sputter deposition of a $0.4 \mu\text{m}$ thick Si_3N_4 layer to serve as a passivation and planarization layer. Then six layers of PI 5878 G polyimide was spin-coated and cured as explained in Section 2.4. Afterwards, another Si_3N_4 layer of the same thickness as the first one was sputter-deposited. Next, NR-9 1500 PY (Futurrex) negative photoresist was spin-coated and patterned, followed by electron

beam evaporation of 50 Å Ti and sputter deposition of 0.5 μm Al layers to fabricate the metal interconnects. Ti deposition was performed at room temperature, using AJA ATC Orion series e-beam evaporator. Fabrication of metal interconnects were completed by lift-off in acetone. Illustrations of simulated layer and micrograph of fabricated metallization layer are given in Fig. 3.5.

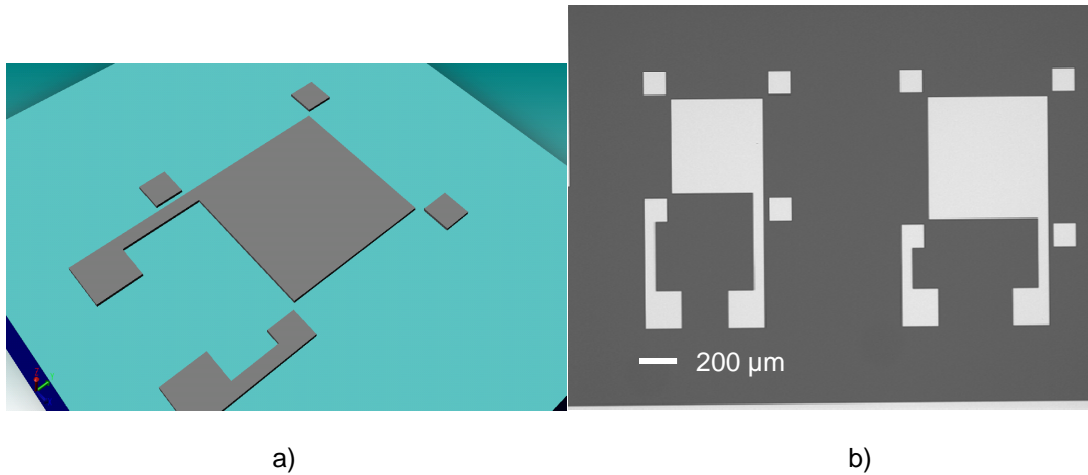


Fig. 3.5 Interconnect metallization layer for z-axis accelerometers a) simulated b) fabricated

Next, HD 4104 (HD Microsystems) photodefinable negative polyimide was spin-coated and patterned to define anchor spaces as shown in Fig. 3.6.

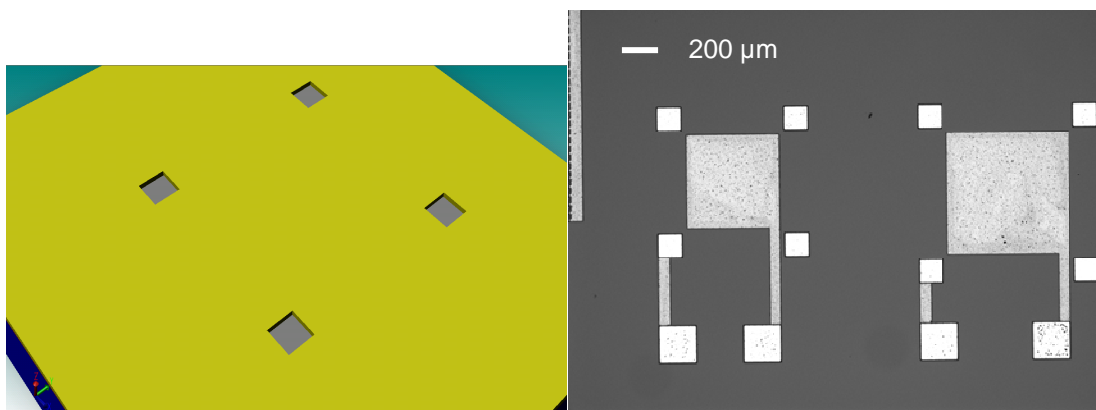
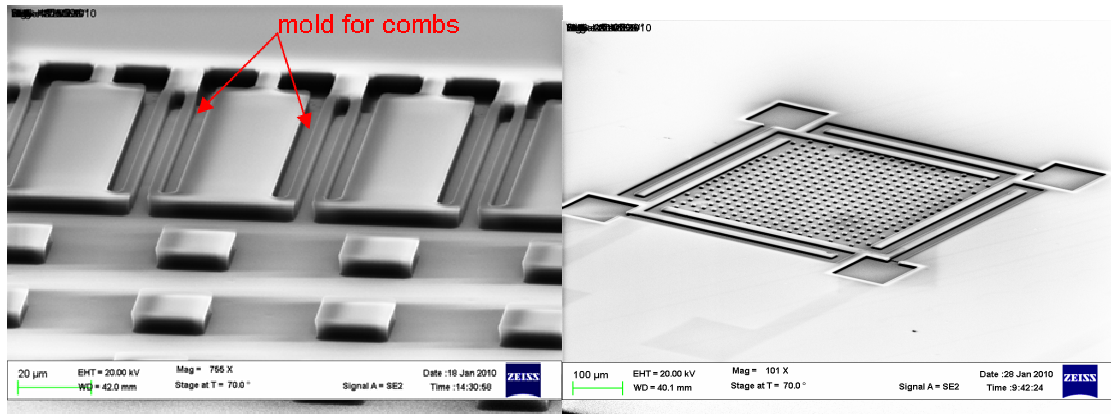


Fig. 3.6 Patterned polyimide layer for z-axis accelerometers a) simulated b) fabricated

Polyimide curing was done in nitrogen gas ambient by ramping up the temperature to 200 °C in 1 h, with a dwell time of 30 minutes at that temperature followed by a ramp up to a peak temperature of 375 °C and keeping it there for 1 h before cooling down to room temperature to obtain a final thickness of 2 μm. Fabrication of proof mass was achieved by UV-LIGA process [83]. As a preparation for the process, first a 1000 Å thick gold layer was deposited at room temperature using e-beam evaporator to serve as a seed layer for the electroplating of Ni proof mass. Then, 6 μm thick NR-4 8000P negative photoresist, which acted as a mold layer during electroplating, was spin coated and patterned. The patterned mold resist is shown in Fig. 3.7.



a)

b)

Fig. 3.7 Patterned NR-4 8000 P mold photoresist showing a) combs for x, y-axes b) z-axis accelerometer

Electroplating was done in a nickel sulphamate solution which was circulating in the plating tank at a rate of 6 gallons/minute. Nickel sulphamate was preferred due to its low stress and high deposition rate compared with Watts solutions [84]. Respective electroplating current density and temperature were determined experimentally as 15 mA/cm² and 45 °C, with the consideration that at current densities exceeding 30 mA/cm², mechanical properties of deposited Ni would deteriorate [85, 86]. Following electroplating, mold resist was removed in acetone and gold seed layer was etched in KI:I:DI water solution with the weight ratio of

4g:1g:32g. Figure 3.8 shows simulated and fabricated z-axis accelerometer after removal of mold resist and seed layer.

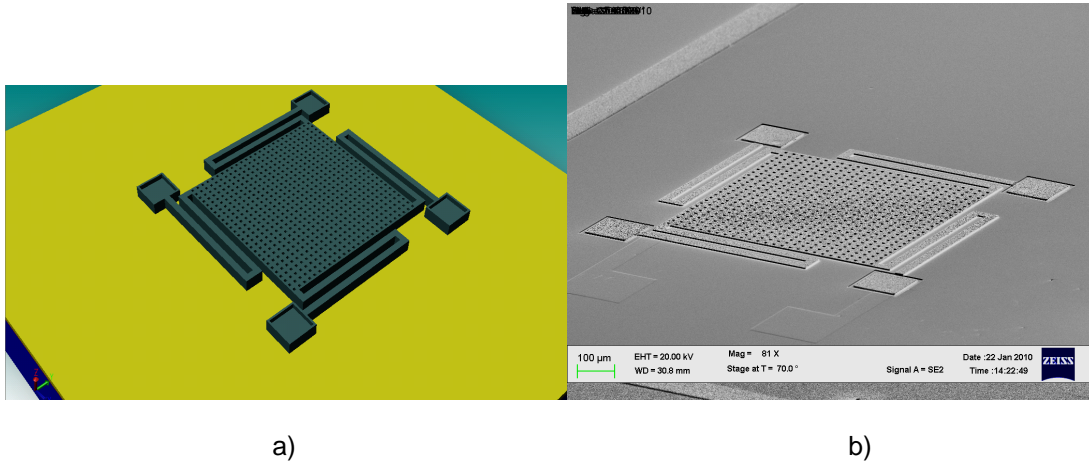


Fig. 3.8 Electroplated z-axis accelerometer a) simulated b) fabricated

Finally the devices were suspended by oxygen plasma ashing of sacrificial polyimide as shown in Fig. 3.9.

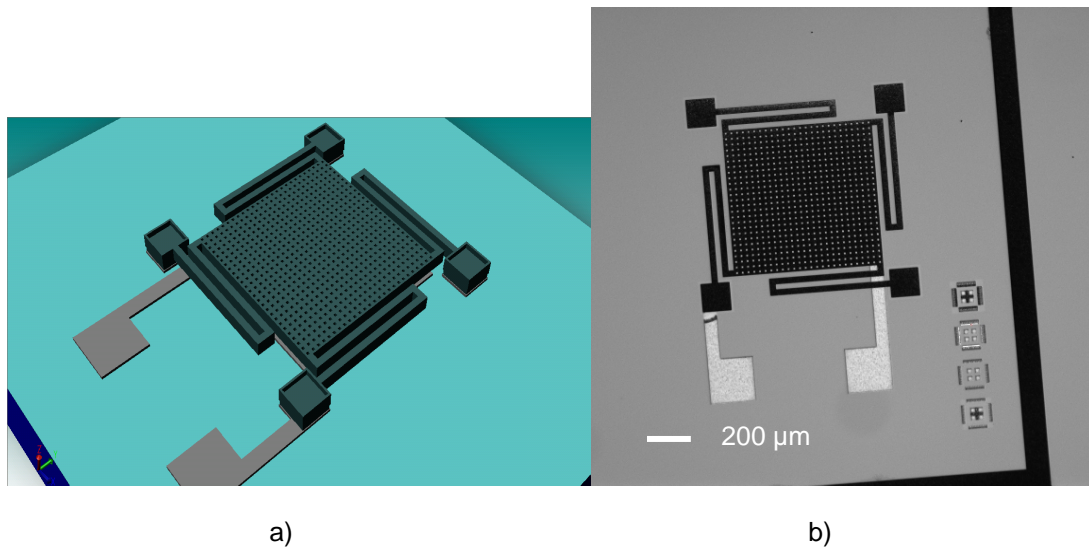


Fig. 3.9 Suspended accelerometer a) simulated b) top view of fabricated device

Accelerometer fabrication on rigid substrate was done following the same procedure, only by skipping flexible polyimide and second nitride deposition steps. Details of all resist processes are given in table 3.2.

Table 3.2 Process details of photoresists that were used in accelerometer fabrication

Resist	Spin Coating		Exposure Energy (mJ/cm ²)	Resist Bake Temperature (C°)		Development Time (sec)	Resist Thickness (µm)
	RPM	Duration (sec)		Pre-bake	Post-bake		
NR-9 1500PY	2500	40	313.6	170	113	8	1.76
NR-4 8000P	4000	40	446.4	170	122	84	6
HD 4104 (PI)	4500	50	160.5	100	none	95	2

3.4 Characterization

3.4.1. Measurement Setup

Test setup consisted of a Controlled Vibration model ED-10 shaker with a shaker power amplifier, HP 3312A signal generator, Irvine Sensors model MS 3110 capacitive readout circuitry, computer to control MS 3110 and Agilent 35670A dynamic signal analyzer. When excited, the shaker plate moved in z-axis only. For z-axis measurements, packaged MEMS accelerometers were directly mounted on the shaker plate along with Controlled Vibration model 2260-010 accelerometer, which served as reference to measure actual acceleration on the plate. Sensitivity of 2260-010 was 400 mV/g, frequency range up to 1kHz, and acceleration

range was $\pm 10g$ level. To measure accelerometer response in lateral axes, a vertical stage was used, on which the packaged sample was mounted. A block diagram of measurement setup is given in Fig. 3.10.

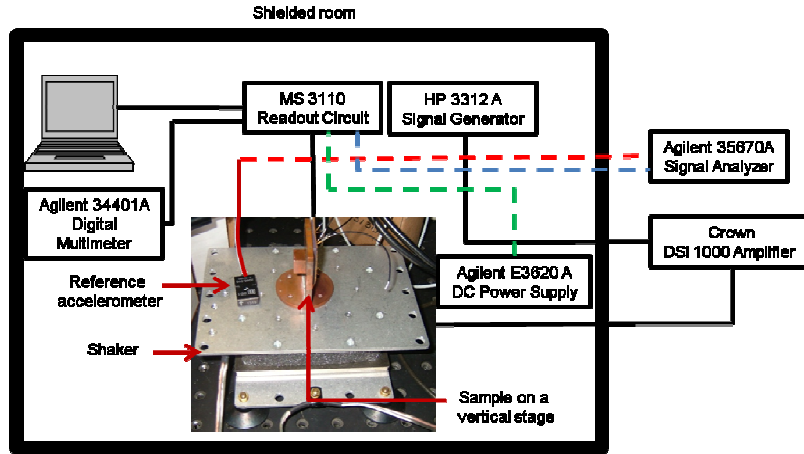


Fig. 3.10 Block diagram of the setup which was used to measure accelerometer response

3.4.2. Response Measurements

The circuit diagram of MS 3110 is shown in Fig. 3.10. Devices were checked for continuity and those showing open circuit were taken as samples. Laterally sensing accelerometers were connected to the readout circuitry as shown in Fig. 3.11, with node 2 connected to proof mass and nodes 1 and 3 connected to the fixed capacitors.

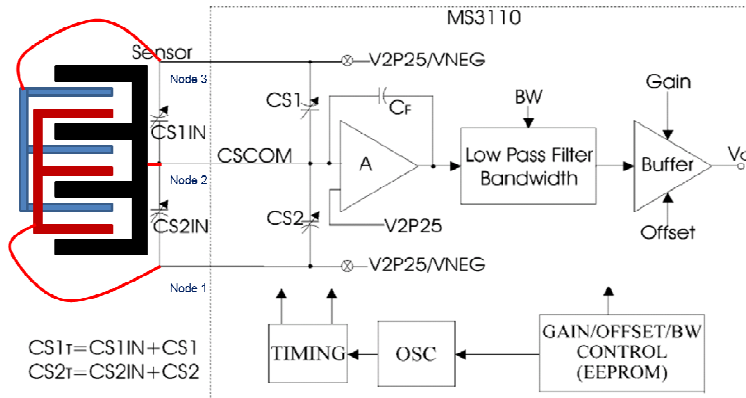


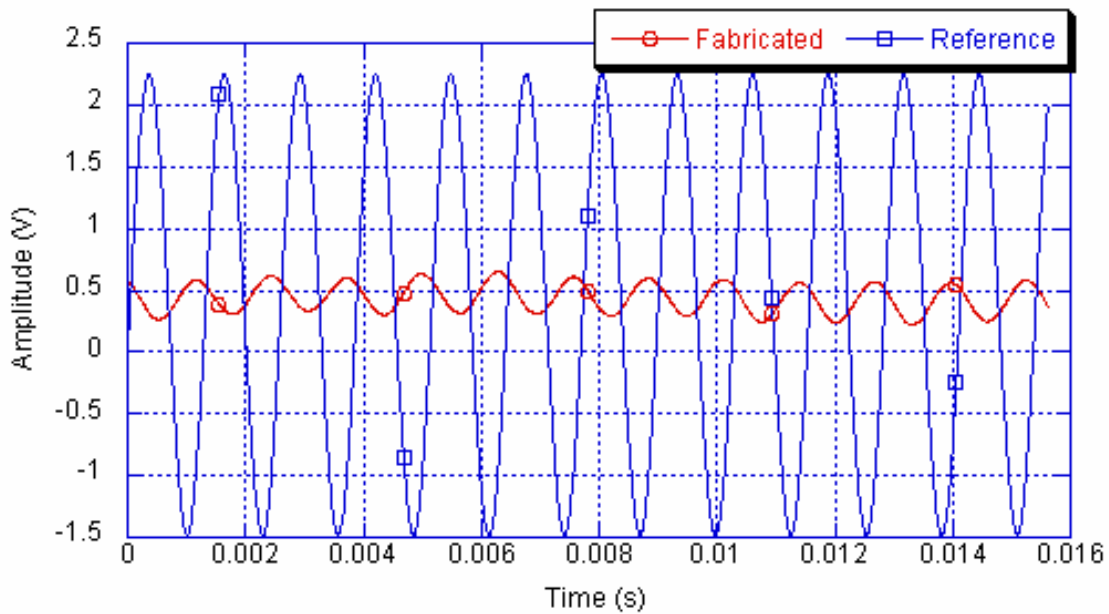
Fig. 3.11 Circuit diagram of MS 3110 capacitive readout circuitry (reprinted with permission from Irvine Sensors)

In the case of z-axis accelerometer, node 3 was left open to measure parallel plate capacitance. After connecting the device, using MS 3110 software, reference voltage, trim capacitor value and output buffer gain values were set as 0.5 V, 5.130 pF and 2 V/V respectively. Next, parasitic and offset capacitances were eliminated by changing CS1 or CS2 balance capacitors, one at a time, until the set reference voltage was reached. The reference accelerometer was placed on the shaker plate and connected to the signal analyzer as shown in Fig. 3.10.

The shaker was excited using sinusoidal signal at 782 Hz by applying 1 V_{p-p}. Shaker excitation was done at two different amplification points by rotating the amplitude knob by 15 and 17 turns, resulting in different maximum accelerations.

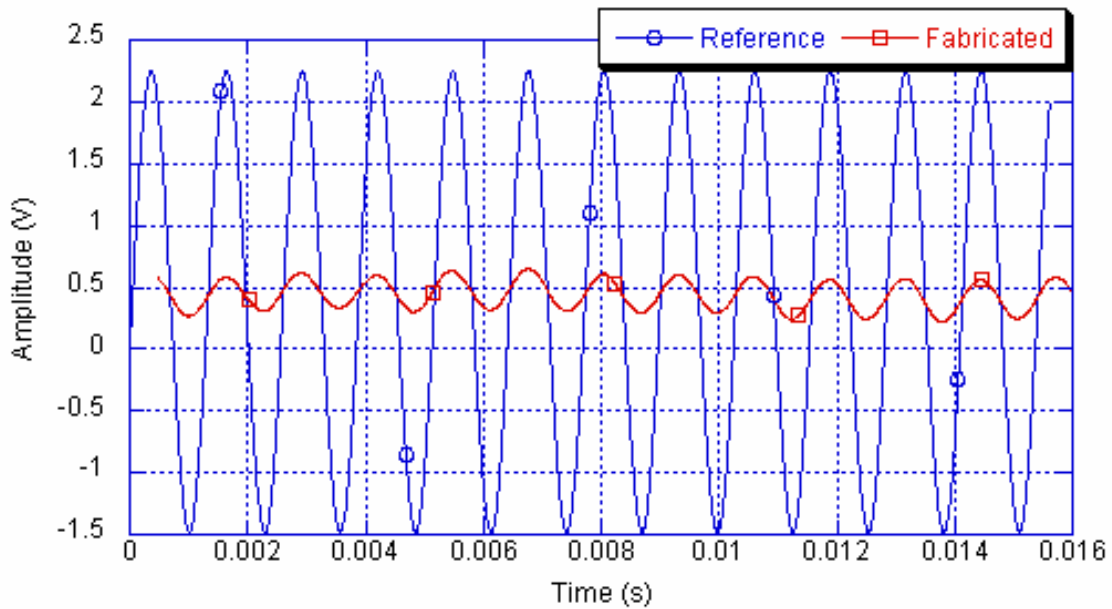
For data analysis, first signal amplitude with respect to time was plotted by overlapping the data from the reference accelerometer and actual device. For each sample, a phase difference between the reference and actual accelerometers was observed as shown in Fig.

3.12.



3.12 Time domain plot of overlapped amplitude data for the reference and fabricated accelerometer

Before further analysis, both of the plots were brought in phase as illustrated in Fig. 3.13.



3.13 Time domain plot of reference and fabricated accelerometer after phase adjustment

Acceleration was calculated by dividing the amplitude of the reference accelerometer by its sensitivity for a given time interval. Then, amplitude of the fabricated device was plotted with respect to acceleration, using the same time interval as shown in Figs. 3.14-3.19.

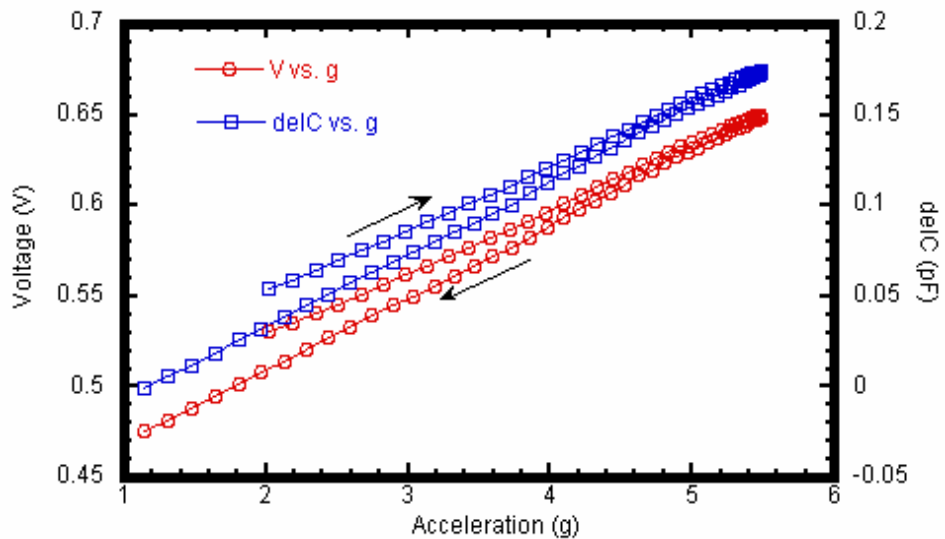


Fig. 3.14 Voltage and capacitance response of the z-axis accelerometer on Si substrate. Capacitance change is 39 fF/g

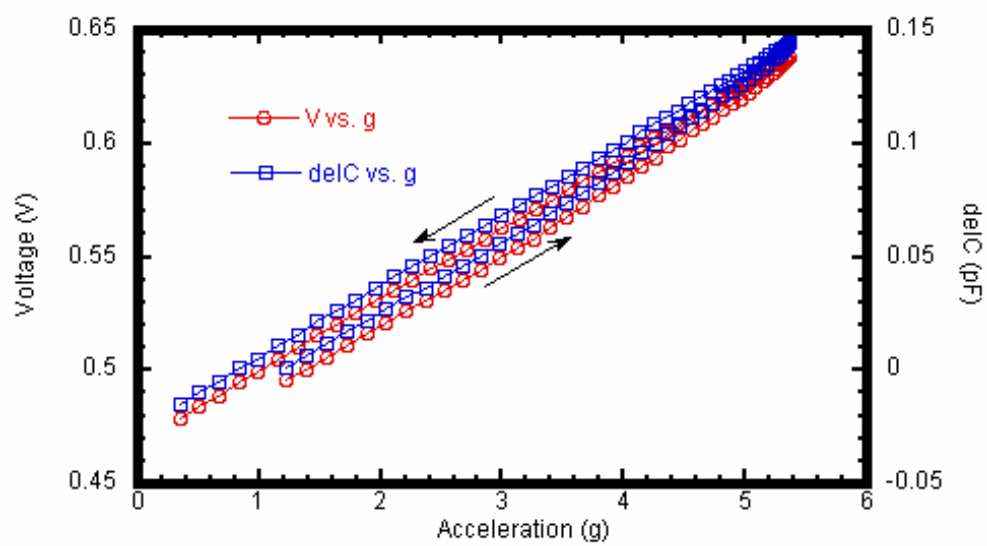


Fig. 3.15 Voltage and capacitance response of the z-axis accelerometer on Si substrate. Capacitance change is 32.4 fF/g

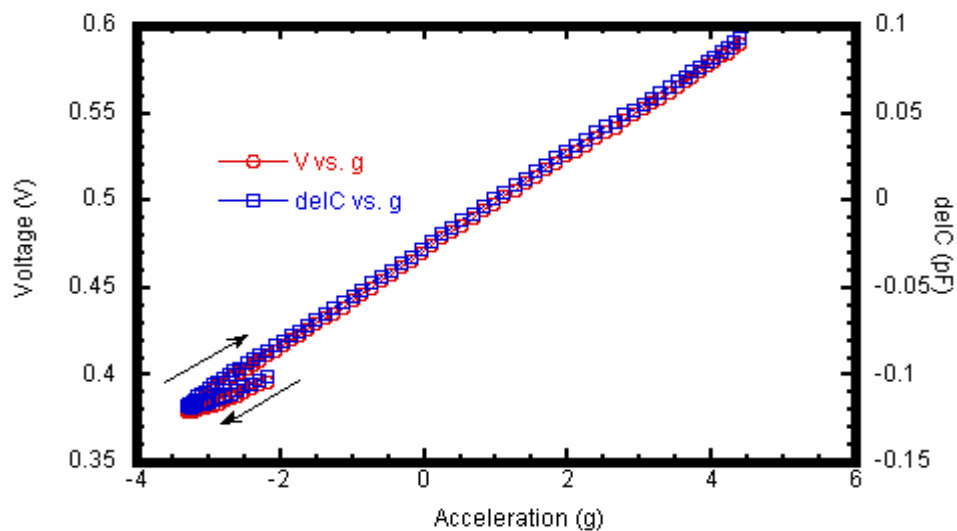


Fig. 3.16 Voltage and capacitance response of the z-axis accelerometer on flexible polymer substrate. Capacitance change is 27.7 fF/g

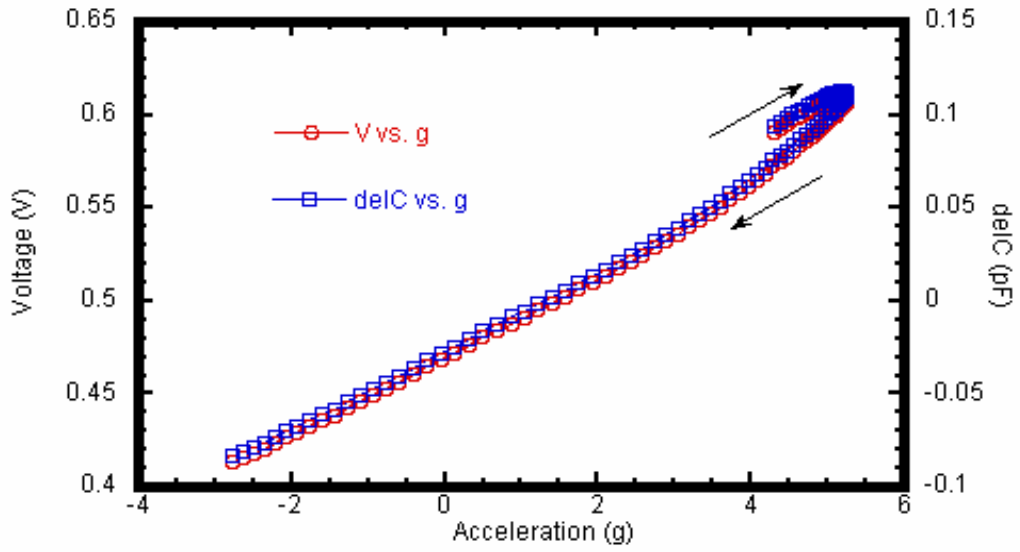


Fig. 3.17 Voltage and capacitance response of the z-axis accelerometer on flexible polymer substrate. Capacitance change is 25.2 fF/g

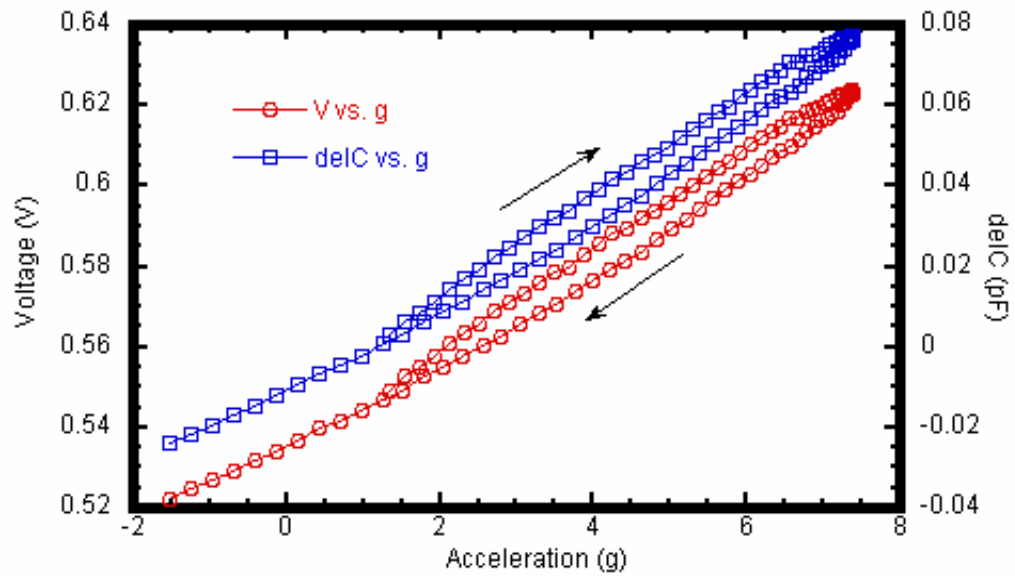


Fig. 3.18 Voltage and capacitance response of the x, y-axis accelerometer on Si substrate. Capacitance change is 11.9 fF/g

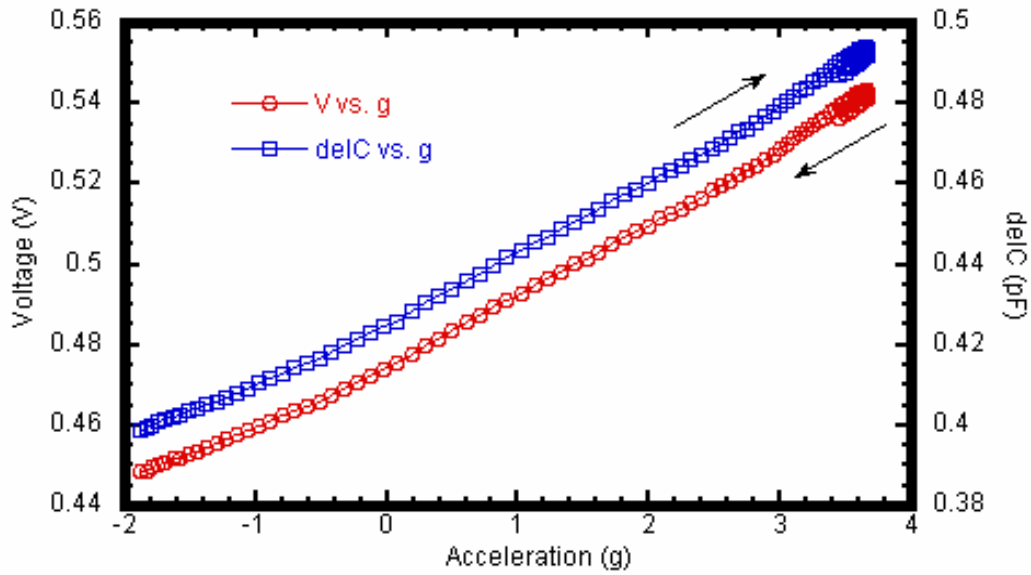


Fig. 3.19 Voltage and capacitance response of the x, y-axis accelerometer on flexible polymer substrate. Capacitance change is 17.5 fF/g

Using slope and intercept of voltage-acceleration plot, actual reference voltage was calculated for 1g. Finally, using

$$V_{out} = 1.14 * V_{2P25} * Gain * \frac{CS_{2T} - CS_{1T}}{CF} + V_{ref} \quad (3.6)$$

corresponding capacitance value for a particular acceleration was calculated, where V_o is the output voltage, V_{2P25} is the circuit reference voltage which had a fixed value of 2.25 V, CF is the trim capacitor, V_{ref} is the reference voltage calculated from voltage-acceleration plot. The change in capacitance is given as

$$\Delta C = CS_{2T} - CS_{1T} \quad (3.7)$$

Figures of response measurements are given in Appendix F. Results of measurements for both z-axis and x, y-axis accelerometers are shown in Table 3.3 for both rigid and flexible substrates.

Table 3.3 Sensitivity of accelerometers fabricated on silicon and flexible polymer substrates

Sample	Sense Axis	Dimensions (μm)	Substrate Type	Sensitivity (fF/g)
1	z	500 x 500	Si	21.9
2	z	650 x 650	Si	32.4
3	z	500 x 500	Si	27.3
4	z	650 x 650	Si	15.8
5	z	650 x 650	Si	39.0
6	z	500 x 500	Si	34.5
7	z	500 x 500	Si	33.8
8	z	650 x 650	Si	22
9	z	500 x 500	Flexible	19.5
10	z	500 x 500	Flexible	22.4
11	z	650 x 650	Flexible	41.8
12	z	500 x 500	Flexible	22.5
13	z	650 x 650	Flexible	18.1
14	z	500 x 500	Flexible	27.7
15	z	650 x 650	Flexible	25.2
16	x, y	1605 x 1281	Si	11.9
17	x, y	1605 x 1281	Si	11
18	x, y	1605 x 1281	Si	9.7
19	x, y	1500 x 632	Flexible	12.6
20	x, y	1500 x 632	Flexible	12.3
21	x, y	1605 x 1281	Flexible	17.5
22	x, y	1500 x 632	Flexible	16.6

For Sample 5, capacitance simulation was repeated after modifying the layout using actual fabricated dimensions. The simulation results gave 28.2 fF/g sensitivity as opposed to a measured value of 39.0 fF/g, indicating that the simulated structure is not an exact and complete recreation of the measured one due to process variations.

In most of the cases, measured capacitance changes showed larger values than the simulated ones. This could be associated with the fabrication non-uniformities, such as variation in the thickness of the sacrificial layer and electroplated Ni as well as photolithography. The effects caused by Ni thickness and photolithography are more pronounced as they influence most of the parameters, such as damping, mass and spring constant.

The springs used for both lateral and vertical sensing are folded beam type as illustrated in Fig. 3.20

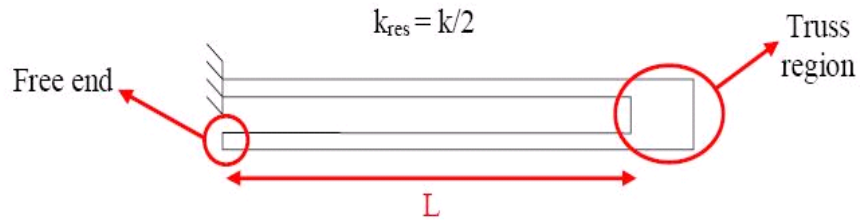


Fig. 3.20 Folded beam spring

The respective spring constants of a folded beam spring in vertical and lateral directions can be expressed as

$$K_v = \frac{Ewh^3}{2l^3} \quad (3.8)$$

and

$$K_l = \frac{Ehw^3}{2l^3} \quad (3.9)$$

where E is elastic modulus, l is length from truss region to free end, h is thickness and w is the spring width. As it is evident from Eqs. 3.8 and 3.9, a change in the dimensions of springs will affect spring constants more dramatically than mass. As evident from Eq. 3.2, it is safe to say that change in displacement was controlled more by the spring constant rather than the mass for a given change in the dimensions of springs.

Capacitance change with acceleration showed hysteresis between negative and positive acceleration paths as shown in Figs. 3.14-3.19. One of the reasons for hysteresis might be the axial rotation of the devices during measurement. Another possibility is the cross-axis effect, which is multidimensional motion instead of the sense direction only. Both the former and the latter are related to spring constant non-uniformities [87].

3.5 Summary

Vertical and lateral sensing accelerometers were designed and simulated for performance comparisons to determine optimal mass, damping, spring constant and sensitivity. Designed devices had spring constant values of around 24.7 N/m for lateral axes accelerometers and around 8 N/m for the z-axis ones. Damping ratio changed between 0.54-0.76 for a temperature range of 200 °F. Resonance frequency calculations showed frequency values on the order of tens of kilohertz. For z-axis devices, a maximum sensitivity of 18.08 fF/g was obtained, while for lateral axes, it was found out to be 7.4 fF/g for the integrated device and 5.3 fF/g for the individual one.

Designed devices were fabricated on silicon and flexible polyimide substrates by surface micromachining. Devices on both types of substrates were characterized for performance. Sensitivity values ranged between 15.8 fF/g to 41.8 fF/g. For x,y-axis accelerometers, sensitivity values ranging from 9.7 fF/g to 17.7 fF/g were measured. Almost all

measured devices showed higher sensitivities than the simulated results, which were related to fabrication non-uniformities.

CHAPTER 4

CONCLUSIONS

Two types of microelectromechanical sensors, piezoresistive pressure sensors and capacitive accelerometers, were designed, fabricated and characterized. Devices were fabricated on Si and flexible polymer substrates. Fabrication was performed via IC compatible surface micromachining process. Response measurements were performed to determine the device sensitivities. Measured sensitivities were compared with simulated values and the differences were explained.

Pressure sensor simulations were performed to determine optimal polysilicon piezoresistor dimensions, position on the structure and sensitivity. Calculations were based on a gauge factor of 50 and an applied pressure of 50 kPa. Calculations on the fabricated devices revealed that the gauge factor of 50, which was used for simulation purposes is an overestimated value, while the applied pressure used for measurements is a lot higher than the one used for simulations. Response measurements on fabricated devices resulted in lower values compared with the simulated results.

The most critical step in the pressure sensor fabrication was that for polysilicon piezoresistors. This was achieved by adopting a relatively low temperature process, metal induced crystallization. Despite its compatibility with processing polymer-based materials, the major drawback of metal induced crystallization is small grain size and relatively low gauge factor. The effects of these parameters were observed during response characterizations by getting lower sensitivities compared with simulations.

Accelerometer simulations were performed to determine parameters such as spring constant, damping, mass and capacitance change as these parameters determine the system's proper motion and sensitivity. Spring constant values obtained from simulations were compared

to those obtained from accelerometer displacement simulations. For lateral axes, both values were in agreement while for z-axis, a slight difference was observed. Damping simulations were done for a temperature range of -40 to 160 °F. Devices were designed to be slightly underdamped to reduce noise with damping coefficients around 0.7.

Accelerometer structures were fabricated by UV-LIGA process which was composed of formation and patterning of mold photoresist, and electroplating steps. Electroplating process was difficult to control due to size difference in cross sectional area from one wafer to the other, which resulted in different current densities and deposition rates.

Voltage response and capacitance change of characterized devices are illustrated in Figs. 3.14-3.19. The characteristics that are shown in Figs. 3.14 and 3.15 belong to z-axis accelerometers on Si substrate with plate size of 650 μm x 650 μm . Although both devices are the same type, almost 20 % difference was observed between sensitivities. Similarly, a comparison of Fig. 3.17 to Figs. 3.14 and 3.15 revealed that the same type of devices fabricated on flexible and rigid substrate have up to 55 % difference in sensitivity. Based on the results of simulations, it was expected that 650 μm x 650 μm devices would show almost three times higher sensitivity than 500 μm x 500 μm ones, however, results obtained in Fig. 3.16 and 3.17 showed around 10 % difference in favor of the former. In Figs. 3.18 and 3.19, voltage and capacitance response of lateral accelerometers on Si and flexible substrates are shown, respectively. Accelerometer on flexible substrate showed 47 % higher sensitivity than the one on Si substrate.

These drastic differences between the devices as well as the fabricated and simulated ones could be related to fabrication non-uniformities and lack of optimization. There are many parameters which affect the device motion and sensitivity, such as damping, spring constant and mass. All of these parameters are controlled through fabrication processes, such as photolithography, electroplating and observed to show variations from one batch to other.

Also, hysteresis was observed on voltage and capacitance change graphs which were plotted with respect to acceleration. This hysteresis was attributed to cross-axis motion as well as axial rotation of devices during measurement.

Although fabrication of pressure sensors and accelerometers were done separately, the next step could be integrating them on a single substrate for the aim of smart skin. Another future step could be process optimization to obtain devices which are comparable with simulated ones. This way, an agreement between simulated and fabricated devices could be obtained.

APPENDIX A
PRESSURE SENSOR DESIGNS AND SIMULATIONS

A.1 Introduction

Twenty one pressure sensor structures were designed for this work. The sensors composed of three different membrane sizes and two differently shaped piezoresistors, y and u shaped. Simulations were performed by applying 50 kPa pressure on the whole surface. Diaphragm displacement values were directly obtained from simulation results. To calculate average strain, change in resistance and output voltage, Eqs. 2.6, 2.7 and 2.4 were used respectively.

In this section, the designed pressure sensors are shown. Results of simulations and calculations for each design are given in Table A.1.

Table A.1 Dimensions of designed pressure sensors and results of simulations. Membrane thickness for sensors having 110 x 110 μm diaphragm is 2.5 μm while it is 1.9 μm for the others during simulations


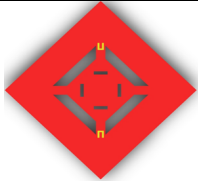

Dimensions					Response to 50 kPa			
Schematic	Plate size (μm)	Bridge arm (μm)	Piezoresistor (μm)	Shape	Displacement (μm)	Average Strain	% [$\Delta R/R$]	V_{out} (mV)
	80 x 80	21.21 x 14.14	11 x 2.5	U	0.941	3.47×10^{-4}	1.74	8.62
	80 x 80	21.21 x 14.14	11 x 2.5	U	0.975	3.76×10^{-4}	1.88	9.31
	80 x 80	28.28 x 14.14	13.5 x 2.5	U	1.200	5.15×10^{-4}	2.58	12.74

Table A.1 – *Continued*



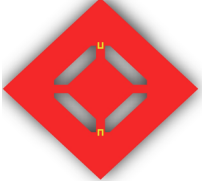

	80 x 80	28.28 x 14.14	9 x 2.6	Y	1.389	3.58×10^{-4}	1.79	8.87
	80 x 80	28.28 x 14.14	9 x 2.6	Y	1.398	3.50×10^{-4}	1.75	8.67
	80 x 80	21.21 x 14.14	11 x 2.5	U	1.060	3.50×10^{-4}	1.75	8.67
	80 x 80	21.21 x 14.14	9 x 2.5	U	0.947	3.12×10^{-4}	1.56	7.74

Table A.1 – Continued





	90 x 90	14.14 x 14.14	8 x 2.6	Y	1.331	1.72×10^{-4}	0.86	4.28
	90 x 90	14.14 x 14.14	8 x 2.6	Y	1.312	1.69×10^{-4}	0.84	4.18
	90 x 90	35.36 x 21.21	16.5 x 4.5	U	1.970	5.26×10^{-4}	2.63	12.98
	90 x 90	35.36 x 21.21	16.5 x 4.5	U	2.020	5.44×10^{-4}	2.72	13.42

Table A.1 – Continued





	90 x 90	42.43 x 21.21	13.5 x 2.5	U	2.440	6.99×10^{-4}	3.50	17.20
	90 x 90	42.43 x 21.21	9 x 2.6	Y	2.767	4.29×10^{-4}	2.15	10.64
	90 x 90	42.43 x 21.21	13.5 x 4	Y	2.780	4.66×10^{-4}	2.33	11.52
	90 x 90	35.36 x 21.21	16.5 x 4.5	U	2.169	5.25×10^{-4}	2.63	12.98

Table A.1 – *Continued*







	90 x 90	35.36 x 21.21	16.5 x 4.5	U	1.961	5.09×10^{-4}	2.55	12.59
	90 x 90	28.28 x 21.21	13 x 3	Y	2.315	3.66×10^{-4}	1.83	9.07
	90 x 90	28.28 x 21.21	13 x 3	Y	1.823	2.31×10^{-4}	1.16	5.77
	110 x 110	42.43 x 21.21	16.5 x 4.5	U	2.230	5.74×10^{-4}	2.87	14.15

Table A.1 – *Continued*

	110 x 110	42.43 x 21.21	13.4 x 4.5	Y	2.373	3.89×10^{-4}	1.95	9.66
	110 x 110	42.43 x 21.21	16.5 x 4.5	U	2.316	5.48×10^{-4}	2.74	13.52

A.2 Summary

Pressure sensors were designed and simulated. Among all structures, devices 3, 6, 7, 9, 12, 13, 15, 16, 19 and 21 from top to bottom on Table A.1 were selected for fabrication. The criteria for selection were relatively higher voltage output, simplicity of structure and ability to go up to high pressures. Selection was based on showing one of these criteria for each structure.

APPENDIX B
PRESSURE SENSOR SIMULATION SETTINGS AND CALCULATIONS

B.1 Introduction

In this section, layouts for pressure sensor simulations are illustrated. Meshing and simulation parameters are given. Software code used for average strain calculations is provided and finally mask layouts that are used for fabrication are shown.

B.2 Procedure for Simulations

For the design, first a layout with the actual planned sizes was designed as shown in Fig. B.1. The layout consisted of four layers, namely a substrate, a polyimide mask for undercut, a trench mask to open trenches and piezoresistor mask to define piezoresistors.

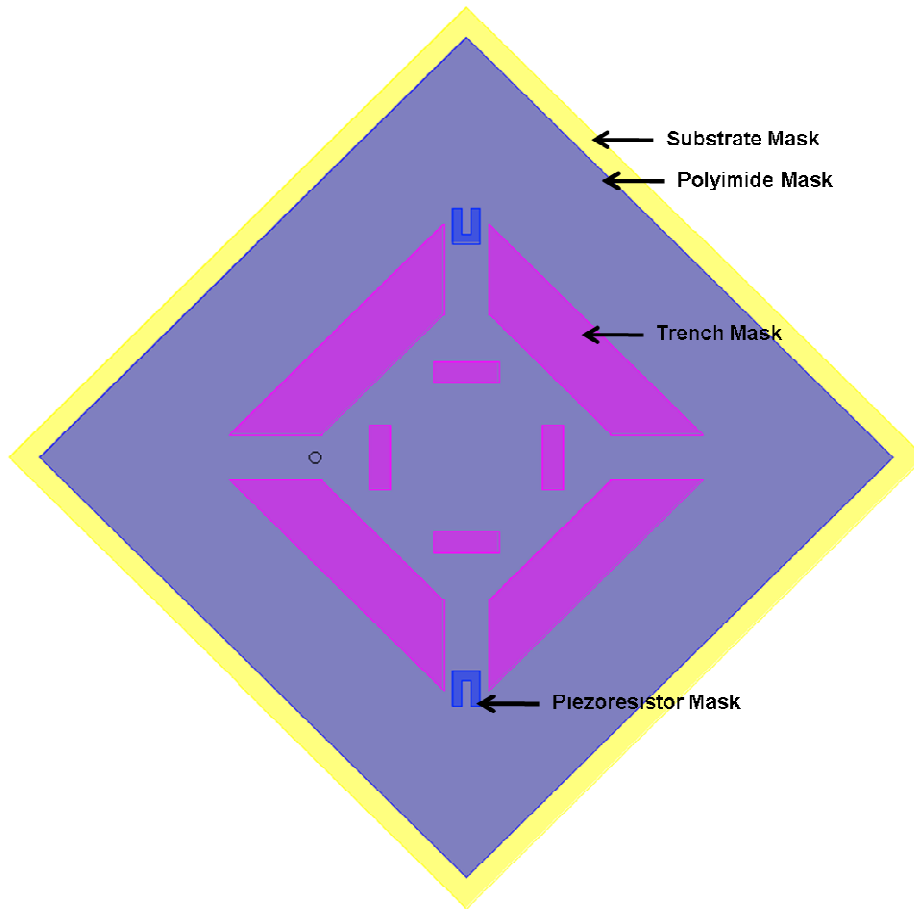


Fig. B.1 Mask layout for one of the pressure sensors, illustrating different layers used to create a 3-D model

Next, a process flow was created. In the process flow, type of layer depositions, layer

thicknesses, resist polarity and masks to pattern deposited layers were defined. A process layer for the layout, given in Fig. B.1. is shown in Fig. B.2.

Number	Step Name	Layer Name	Material Name	Thickness	Mask Name	Photoresist
0	Substrate	Substrate	POLYIMIDE	40	SubstrateMask	
1	Si3N4 Passivation	Layer1	SI3N4	1		
2	Sacrificial Layer	Layer1	POLYIMIDE	2.5		
3	Sacrificial Layer Pattern				PolyimideMask	-
4	Membrane Deposition	Layer1	SI3N4	1.9		
5	Trench Cut				TrenchMask	-
6	Piezoresistor Deposition	Layer5	POLYSILICON	0.5		
7	Piezoresistor Pattern				PiezoresistorMask	+

Fig. B.2 Process flow for pressure sensor simulations

Using the layout and process file, a 3-D solid model was created as shown below

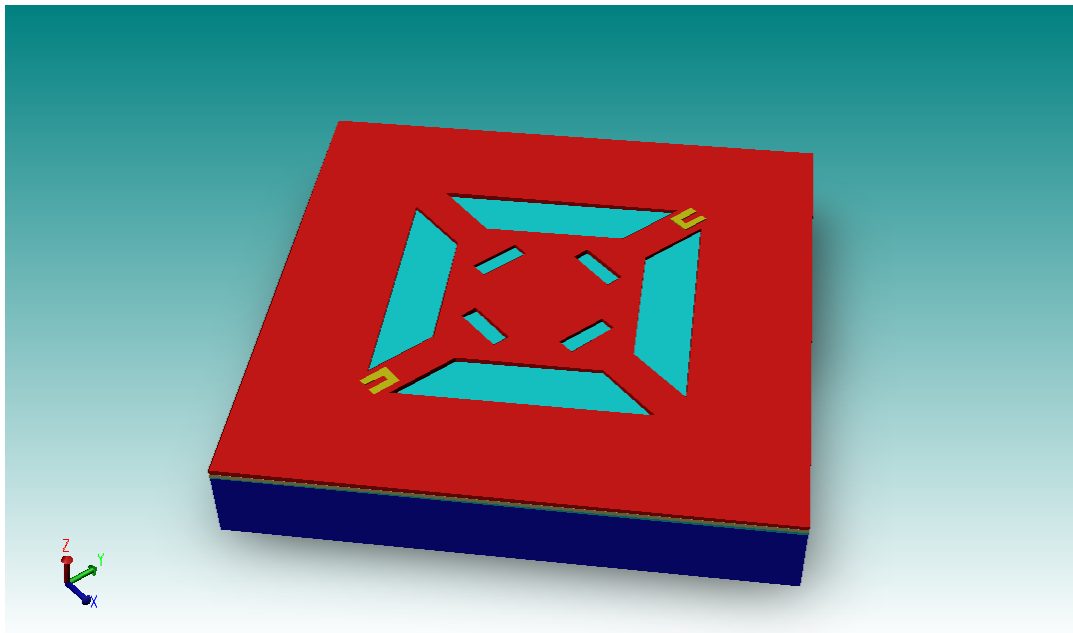


Fig. B.3 3-D solid model of the pressure sensors

Next, the layers that are necessary for simulation were transferred into mesh model and

meshed using extruded brick with a mesh size of 2 μm . The meshed 3-D model and meshing parameters are given in Fig. B.4. and Fig. B.5., respectively. After meshing, the boundaries that will be used during simulations are defined. All sides of the model were fixed and the entire top surface was selected for pressure application. An illustration of the boundary conditions is given in Fig. 2.4. in Section 2.3.

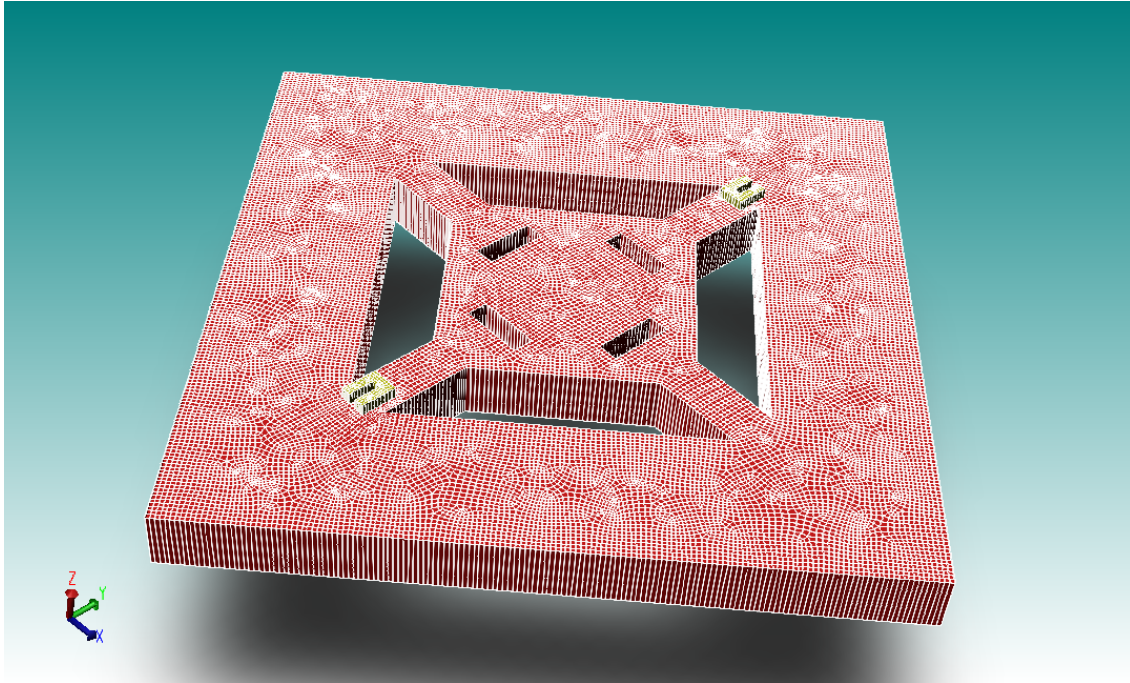


Fig. B.4 Meshed 3-D solid model of pressure sensor

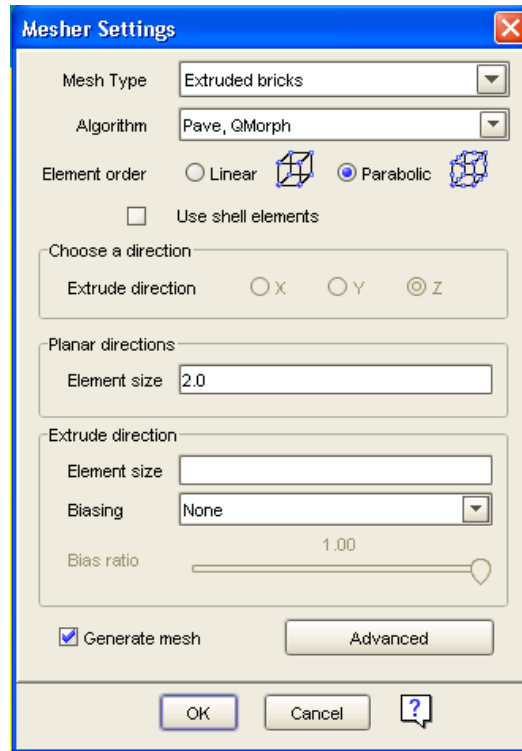


Fig. B.5 Mesher settings for the pressure sensor simulations. Extruded bricks with parabolic elements were used for simulations. Mesh size was kept as 2 μm .

For simulations, MemMech module of CoventorwareTM was used. In the module settings, mechanical analysis was selected. Simulations were done assuming linear and steady state properties. No additional analysis was selected. An image of the settings window is given in Fig. B.6.

After settings, boundary conditions were determined. For membrane deflection, surface boundary conditions were used by fixing all sides denoted as fixed and applying 0.05 MPa, which is the default unit, to the top. Surface boundary conditions are shown in Fig. B.7.

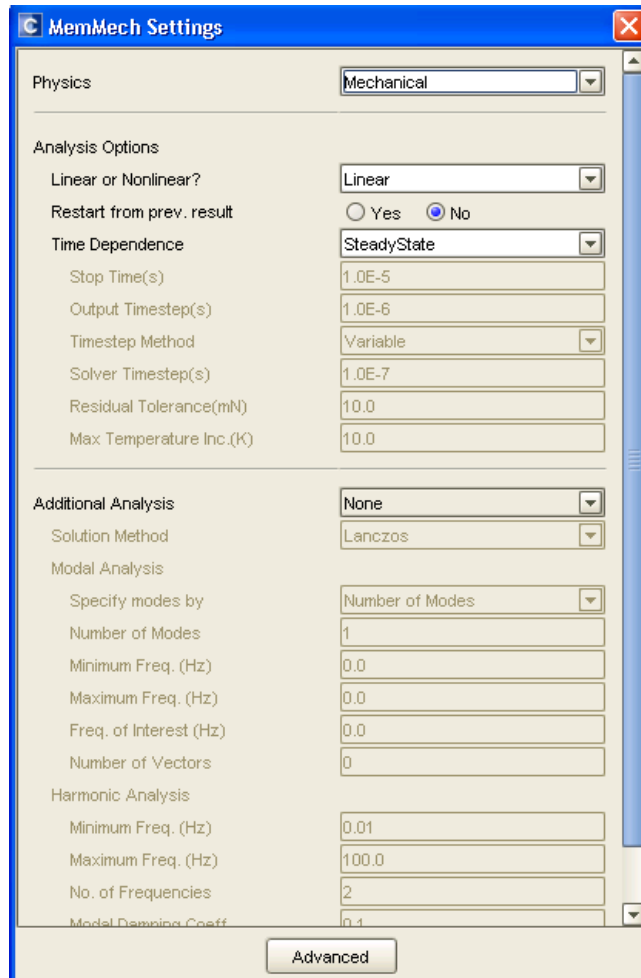


Fig. B.6 MemMech settings used for pressure sensor simulations

SurfaceBCs	FixType	Patch1	and1	Patch2	and2	Patch3	LoadValue	Variable	Transient	
Set1	fixAll	side	and	none	and	none	Scalar	0.0	Fixed	Fixed
Set2	LoadPatch	top	and	none	and	none	Scalar	0.05	Fixed	Fixed
Set3	none	none	and	none	and	none	Scalar	0.0	Fixed	Fixed

Fig. B.7 Surface boundary conditions for pressure sensor simulations

B.3 Calculations

After the simulations, average strain was calculated using Eq. 2.6. Simulation results were used to find strain values, ϵ_{xx} and ϵ_{yy} . U shaped piezoresistors were divided into three regions, while Y shaped ones were divided into five regions. The images of piezoresistors are given in Fig. B.8.

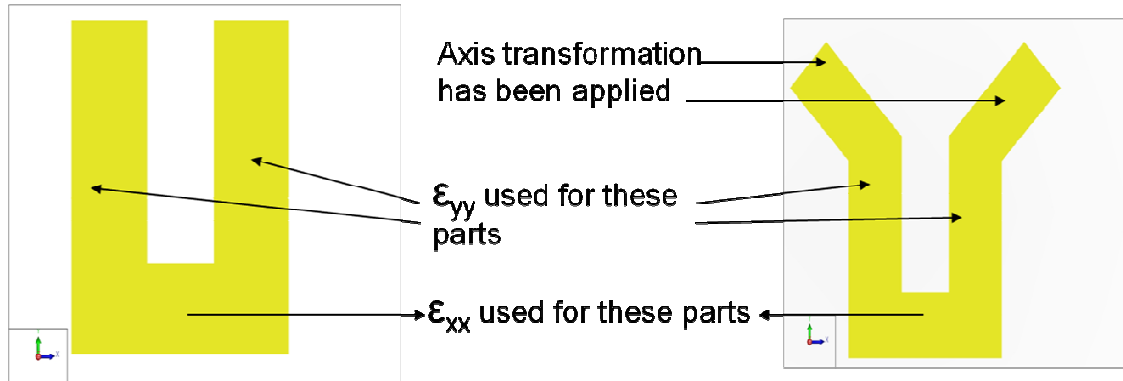


Fig. B.8 U and Y shaped piezoresistors. Different regions for strain calculations are shown

Using point extraction, at least 200 data points were extracted from each region in the form of a text file. Then, these text files were converted into excel files. Using the following Matlab™ code and excel file data, average strain and total area of the piezoresistor were calculated.

```
% reads an excel file and extracts useful data to plot
% also reads the data headers that precede the data

%reading the xls file (in the same directory)
[raw_data,header_info] = xlsread('big_ui_longitudinal.xls')

%data in the xls file is arranged as
% Col 3, Col 4, Col 2
% X    Y    strain
X=raw_data(:,3); %column 1
Y=raw_data(:,4); % column 2
strain=raw_data(:,2); % column 3

mydata = [X Y strain];

minX=min(X); minY=min(Y);
maxX=max(X); maxY=max(Y);
```



```

% Define the grid density
m=250;% No. of rows
n=250;% No. of columns

% Make a X x Y grid, called [Xi,Yi]
x1 = linspace(minX,maxX,n);
y1 = linspace(minY,maxY,m);
[Xi,Yi] = meshgrid(x1,y1);

%map mag on to the grid
straini=griddata(X,Y,strain,Xi,Yi);

%generate the mesh plot or just the contours
%[C,h]=contour(y1,z1,magi), title('Device 1b4 Area Scan 8'),...
mesh(x1,y1,straini), title('Plot of strain_y as a function of X and Y'),...
xlabel('x (microns)'),ylabel('y (microns)'),zlabel('Strain_Y');
%set(axes_handle,'YGrid','on')
%clabel(C,h);
view([-37.5,30]);

minstr = min(min(straini));
maxstr = max(max(straini));
AvgStr = 0;
TotalArea = 0;
for i = 1:249
    for j = 1:249
        if mean(straini(i:i+1, j:j+1)) >= minstr & mean(straini(i:i+1, j:j+1)) <= maxstr
            AvgStr = AvgStr + mean(straini(i:i+1, j:j+1)) * (Xi(i, j+1) - Xi(i, j)) * (Yi(i+1, j) - Yi(i, j));
            TotalArea = TotalArea + (Xi(i, j+1) - Xi(i, j)) * (Yi(i+1, j) - Yi(i, j));
        end
    end
end
TotalArea
AvgStr

```

B.4 Design of Mask Layouts

A mask that is used in fabrication is composed of an array of dies, containing the devices that are going to be fabricated. Thus, while creating the mask layout, the design was performed for a single die. First the trench masks and piezoresistor masks for select devices were transferred into the die as shown in Figs. B.9 and B.10, respectively. Then, the metallization layer and finally the bond pad masks were created as shown in Figs. B.11 and B.12. All of the masks that were used in fabrication are light field masks.

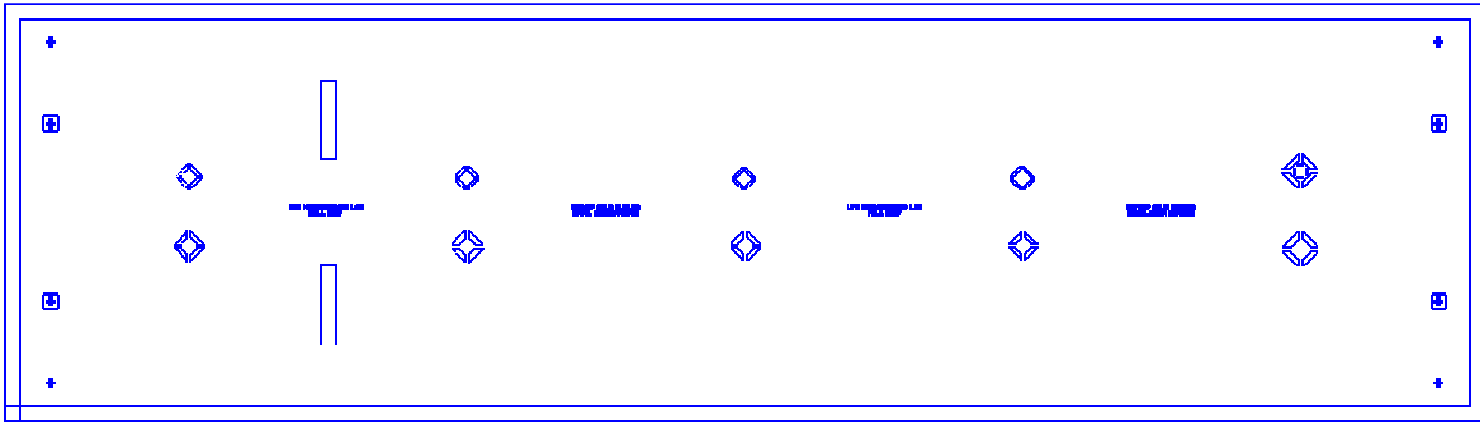


Fig. B.9 Trench mask to fabricate trenches

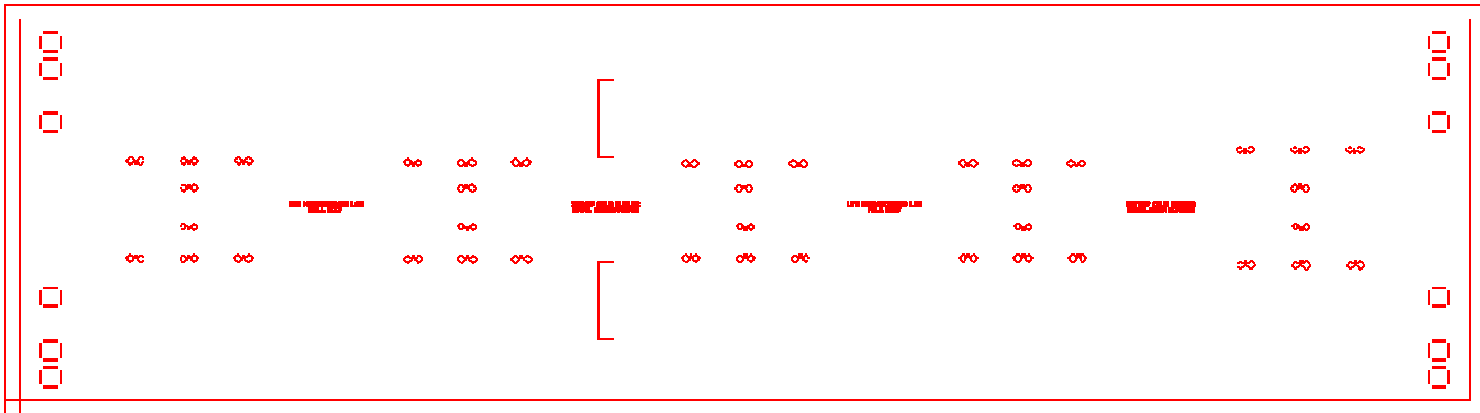


Fig. B.10 Piezoresistor mask to fabricate piezoresistors

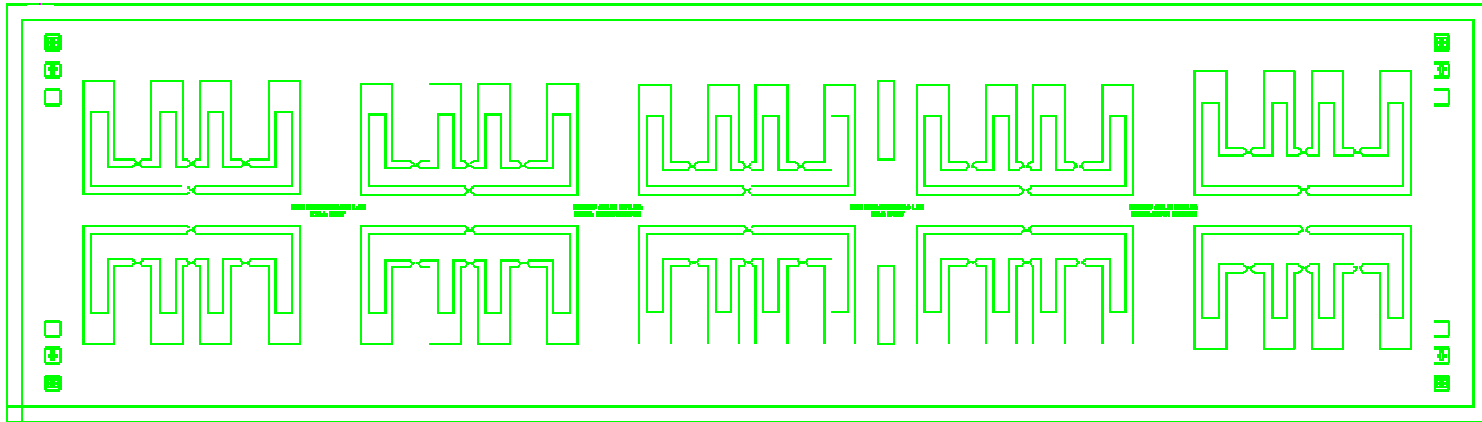


Fig. B.11 Metallization mask to create metal interconnects

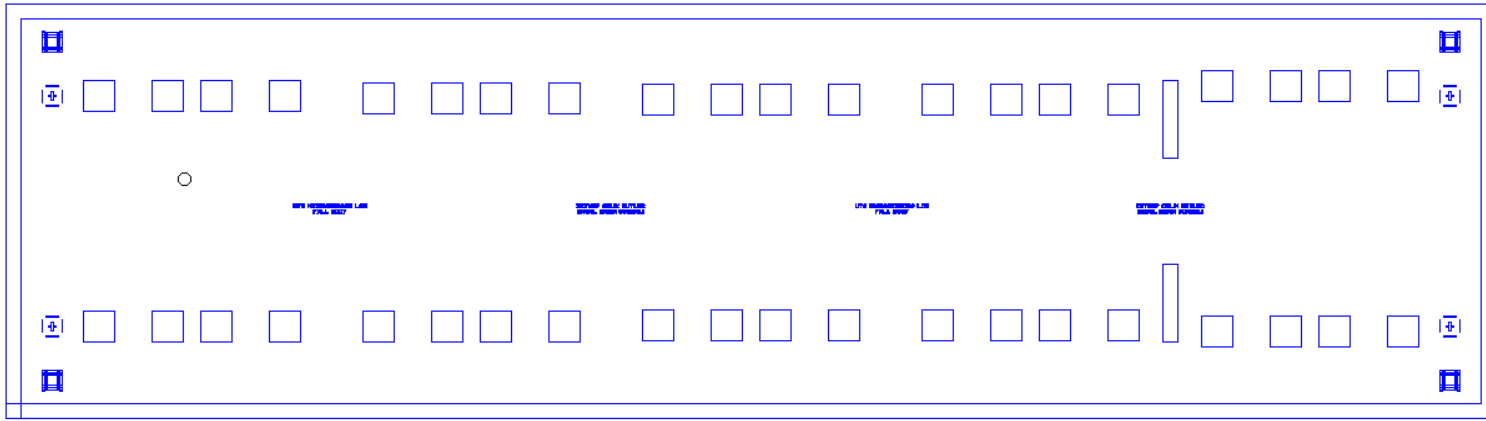


Fig. B.12 Bond pad mask to create bond pads

B.5 Summary

This appendix starts with the explanation of layout formation and process creation to form the 3-D solid model. Then, boundary conditions and simulation parameters were expressed. Afterwards, the MatlabTM code to calculate average strain was given and calculation procedure was explained. Finally, designed mask layouts that were used in fabrication were shown.

APPENDIX C

I-V CHARACTERIZATION RESULTS OF PRESSURE SENSORS

C.1 Introduction

After ashing of the sacrificial layer, I-V characterization was performed on select pressure sensor samples before and after packaging and wire bonding. I-V characterization was performed by applying a current sweep between $\pm 6 \times 10^{-6}$ A. The circuit diagram of the sensors is given in Fig. C.1. Twelve samples were characterized. The positions of samples on the die and results of I-V characterization are shown in Figs. C.2-C.14.

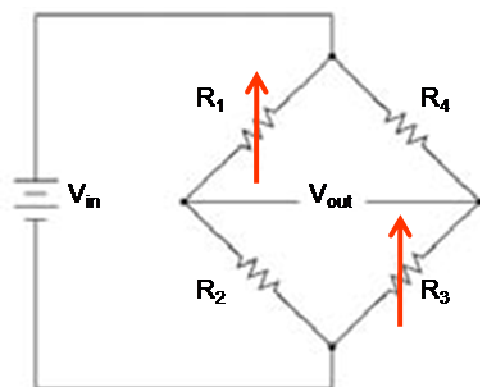


Fig. C.1 Equivalent circuit of pressure sensors. Arrows indicate active resistors

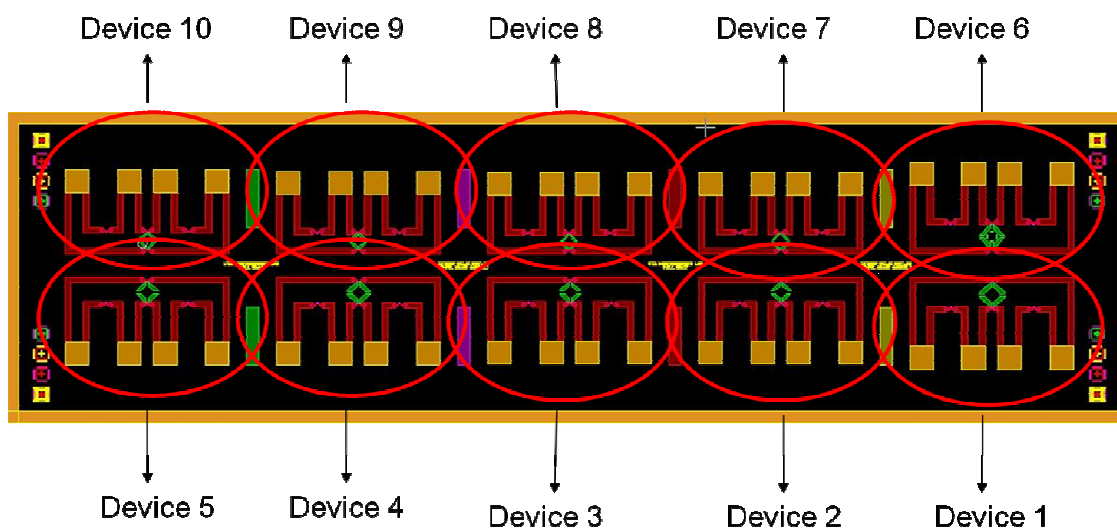


Fig. C.2 Positions of selected devices on the die

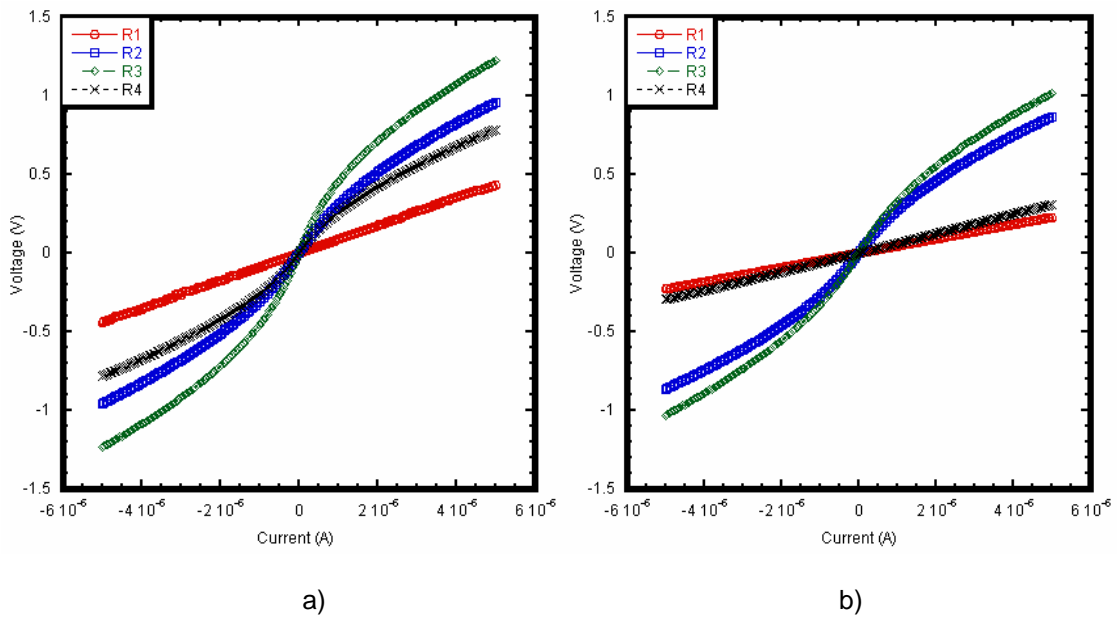


Fig. C.3 I-V characteristics of Sample 1 a) before b) after wire bonding. Corresponding device is Device 3

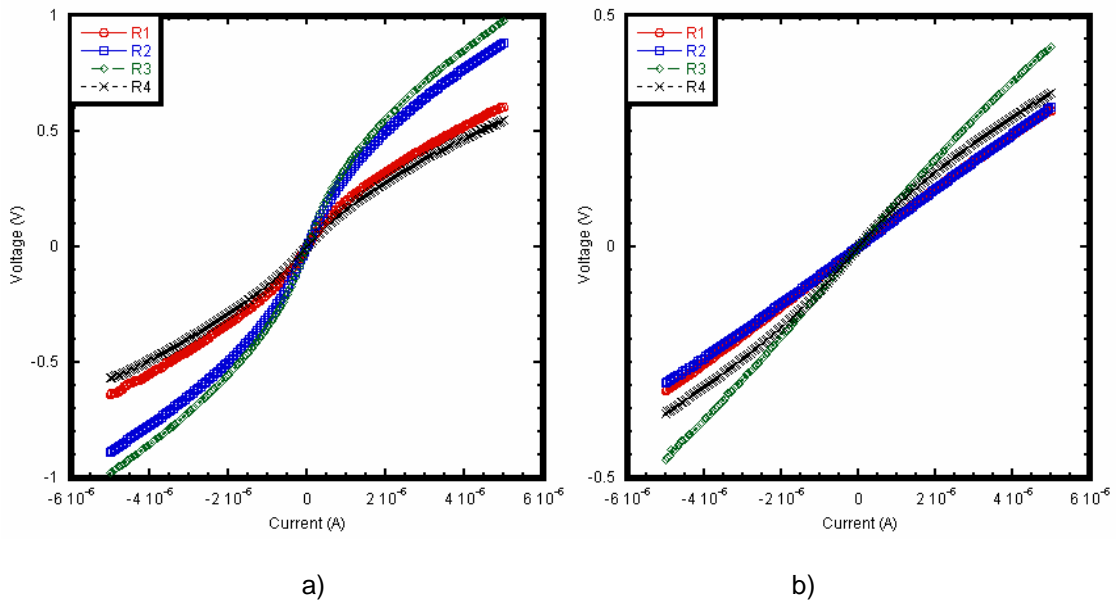


Fig. C.4 I-V characteristics of Sample 2 a) before b) after wire bonding. Corresponding device is Device 1

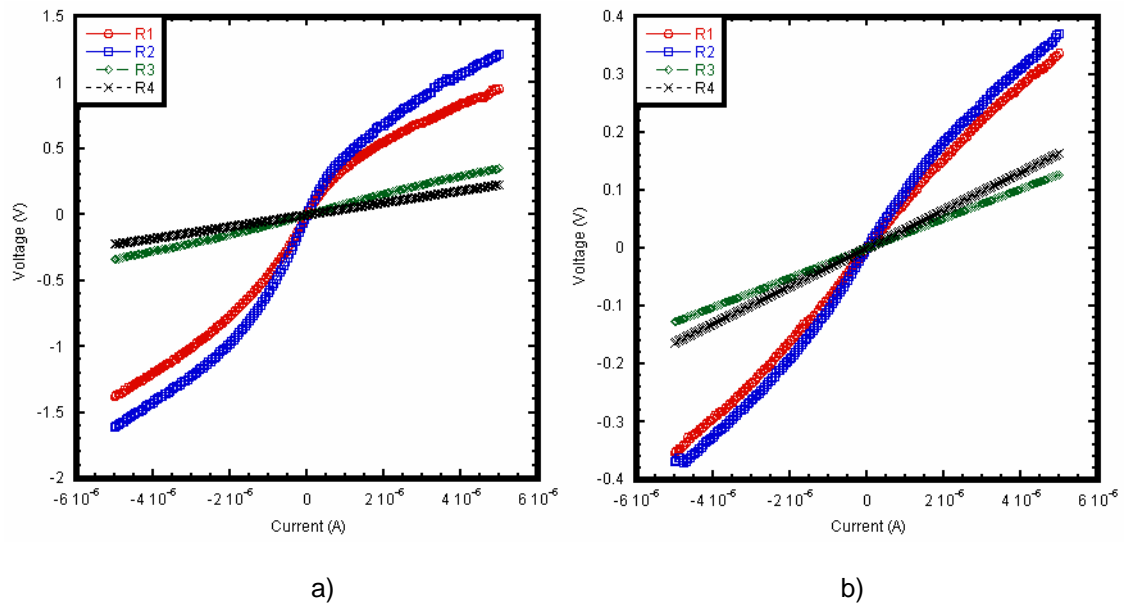


Fig. C.5 I-V characteristics of Sample 3 a) before b) after wire bonding. Corresponding device is Device 3

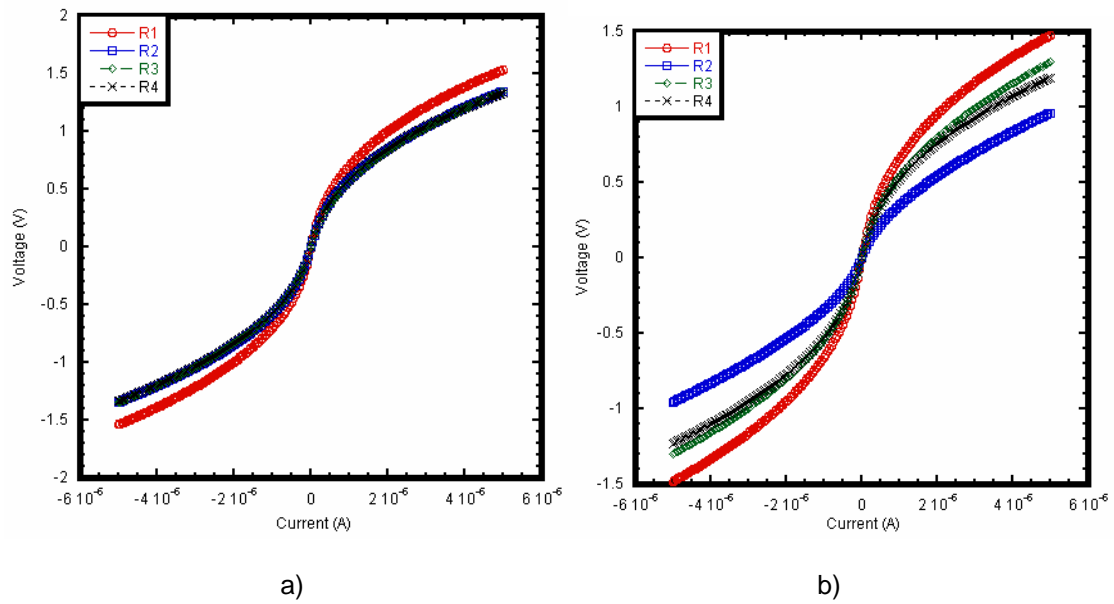


Fig. C.6 I-V characteristics of Sample 4 a) before b) after wire bonding. Corresponding device is Device 6

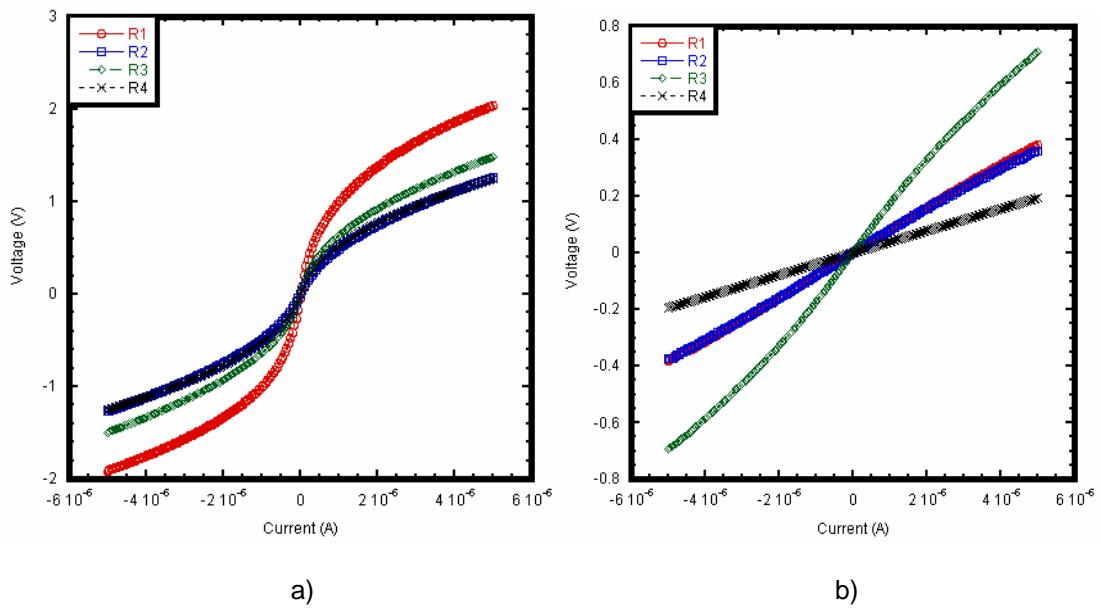


Fig. C.7 I-V characteristics of Sample 5 a) before b) after wire bonding. Corresponding device is Device 1

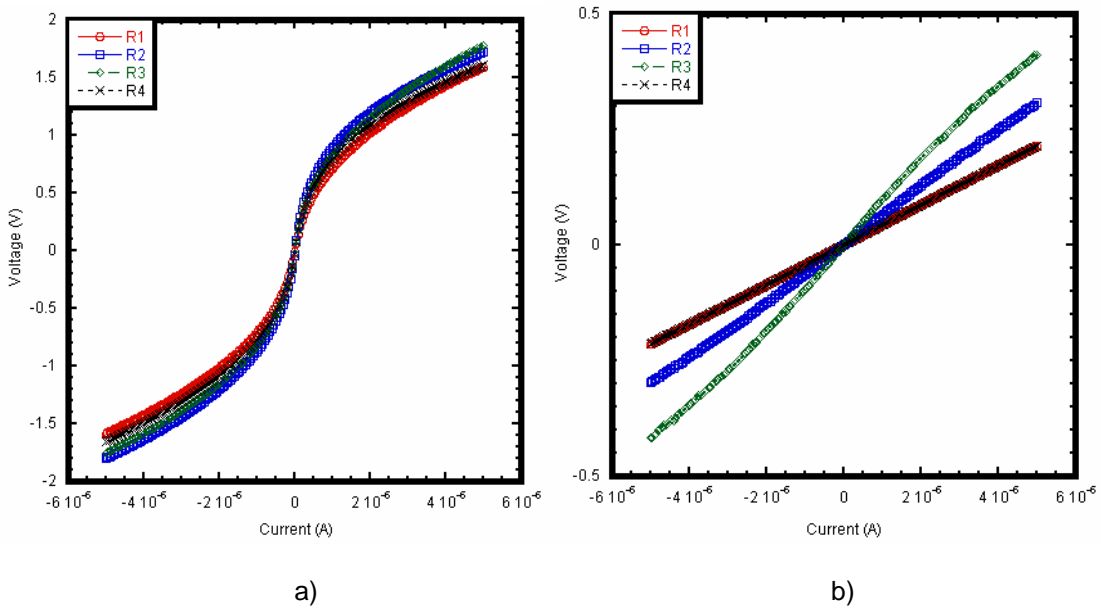


Fig. C.8 I-V characteristics of Sample 6 a) before b) after wire bonding. Corresponding device is Device 1

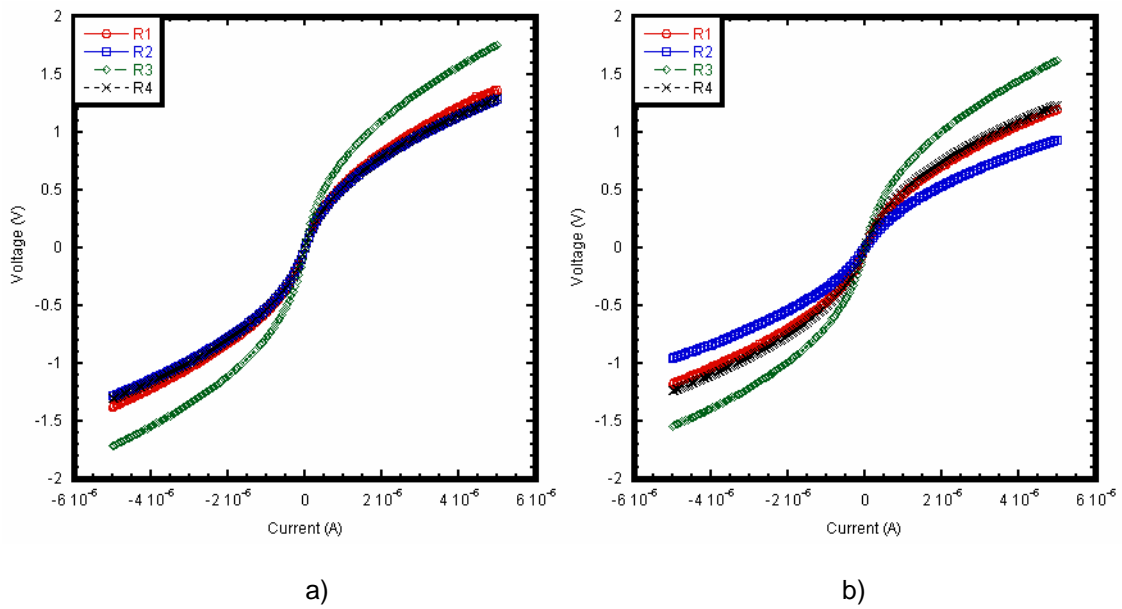


Fig. C.9 I-V characteristics of Sample 7 a) before b) after wire bonding. Corresponding device is Device 6

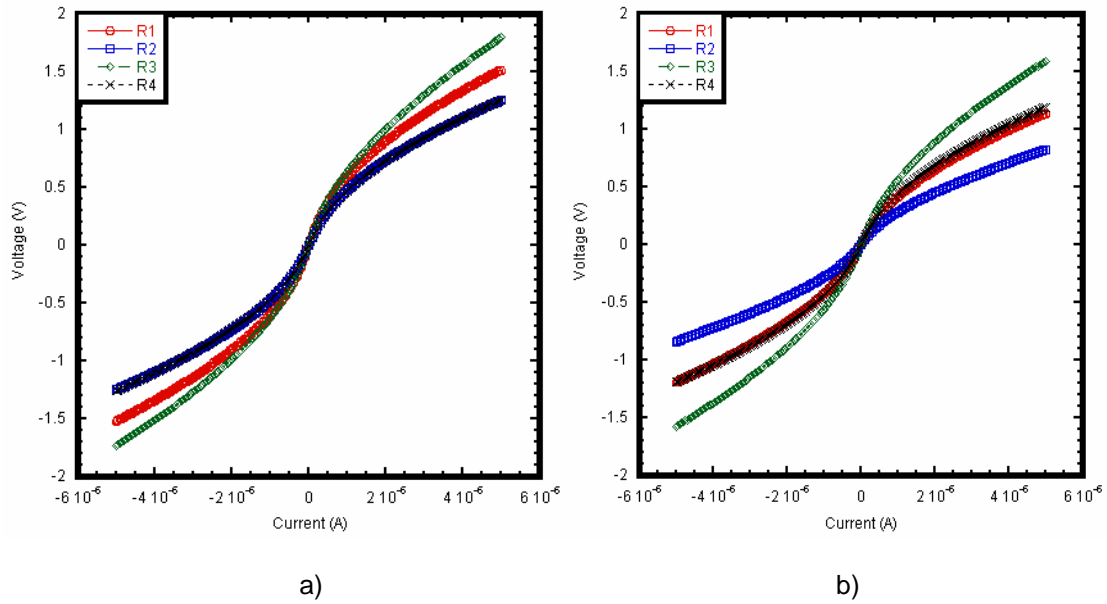


Fig. C.10 I-V characteristics of Sample 8 a) before b) after wire bonding. Corresponding device is Device 3

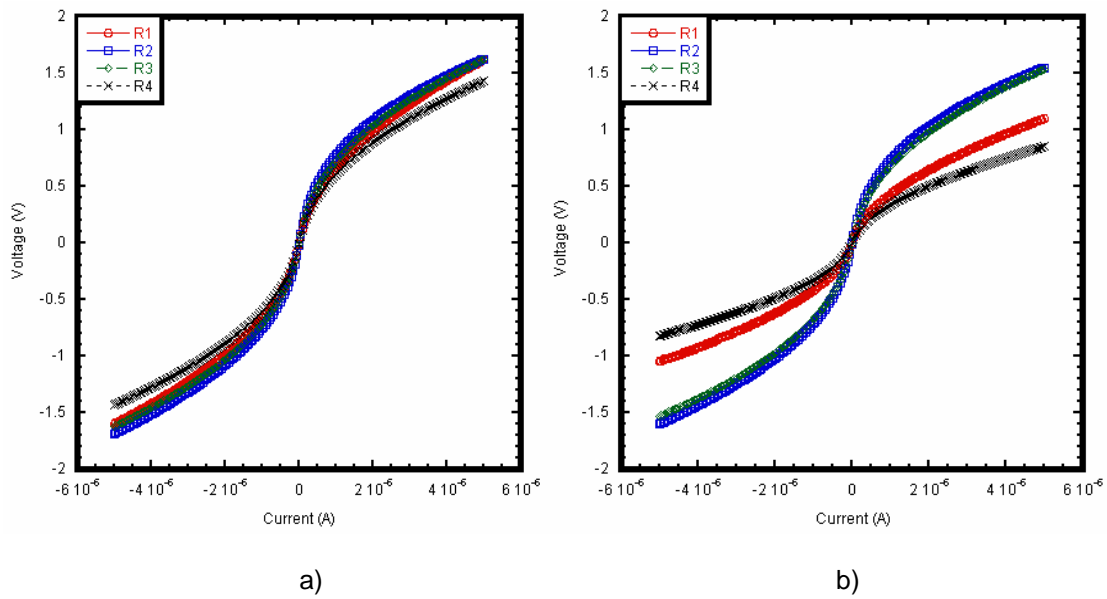


Fig. C.11 I-V characteristics of Sample 9 a) before b) after wire bonding. Corresponding device is Device 2

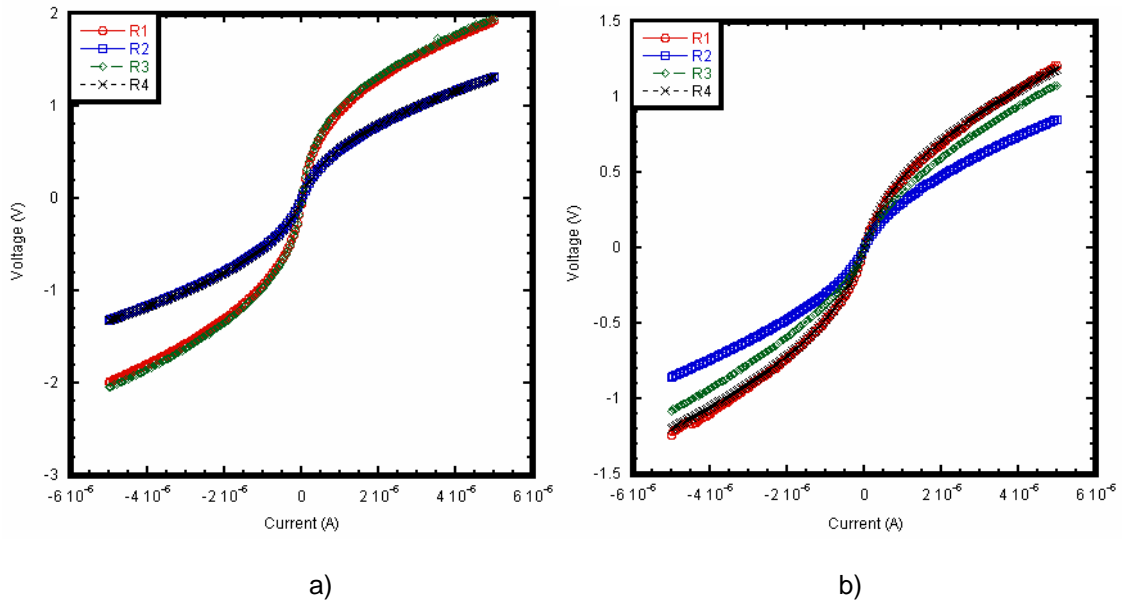


Fig. C.12 I-V characteristics of Sample 10 a) before b) after wire bonding. Corresponding device is Device 3

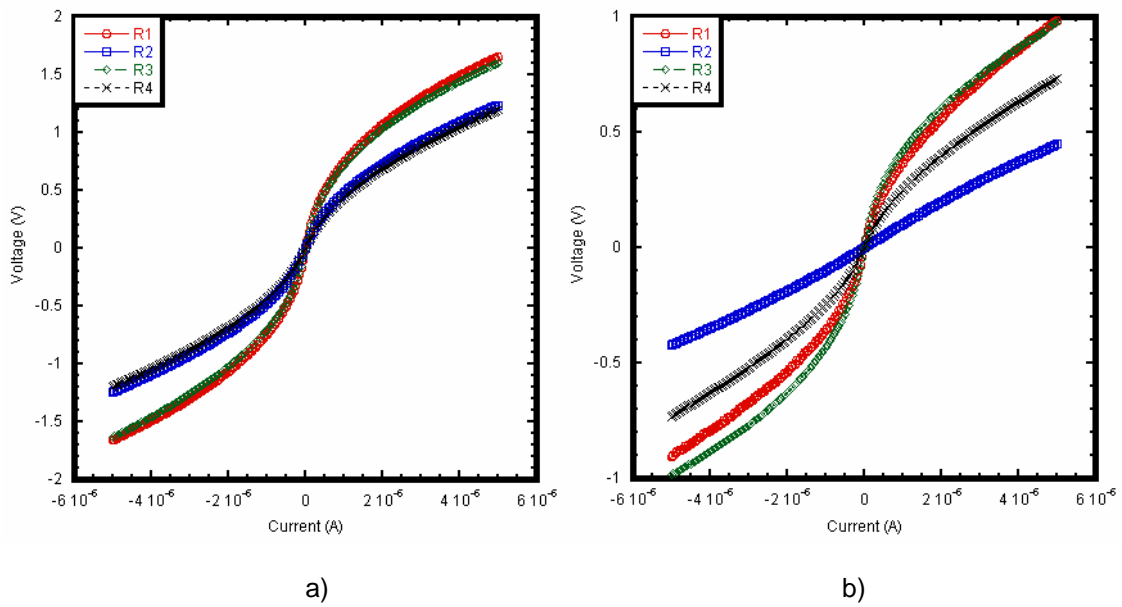


Fig. C.13 I-V characteristics of Sample 11 a) before b) after wire bonding. Corresponding device is Device 3

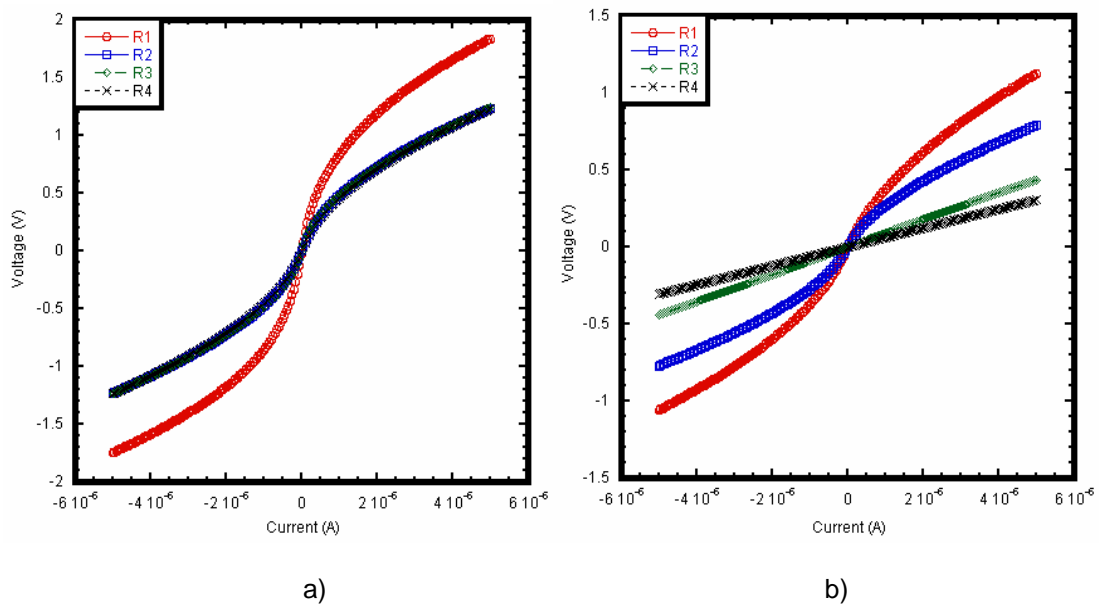


Fig. C.14 I-V characteristics of Sample 12 a) before b) after wire bonding. Corresponding device is Device 6

C.2 Summary

I-V characteristics of select samples were shown. Characteristics showed variations before and after packaging.

APPENDIX D
CAPACITIVE ACCELEROMETER DESIGNS

D.1 Introduction

Six different accelerometer structures were designed. Two were designed to measure acceleration in z-direction, while others, including one integrated x,y-axes accelerometer, were designed for acceleration detection in lateral axes.

In this section, first the device notation is given by illustrating device layout on the die. Then, dimensions and properties of designed accelerometers are given.

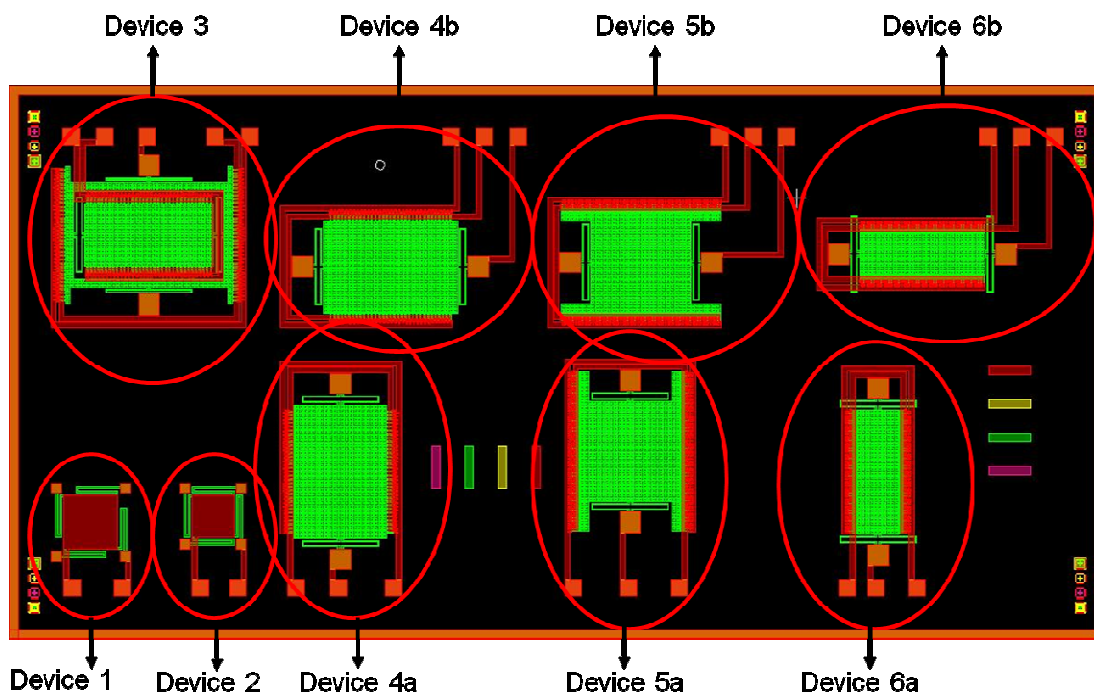
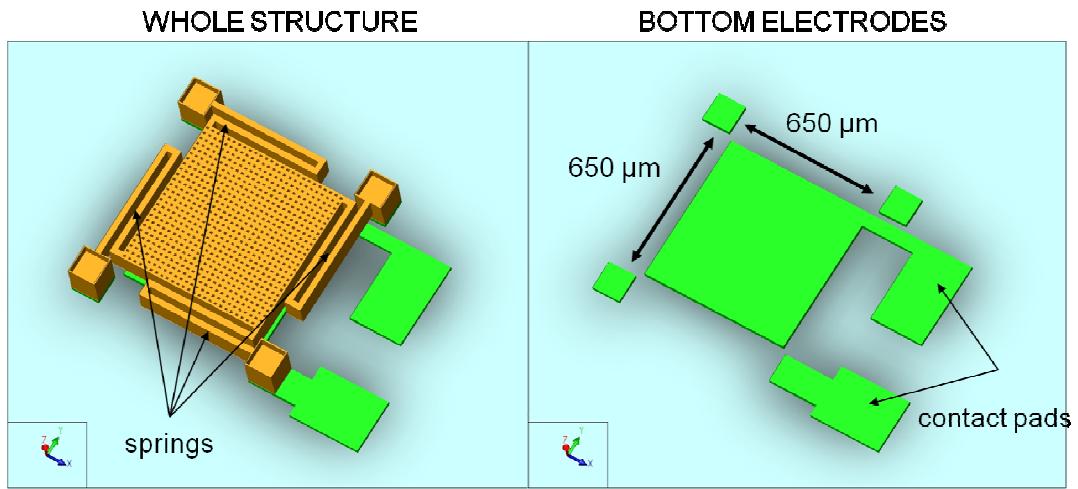
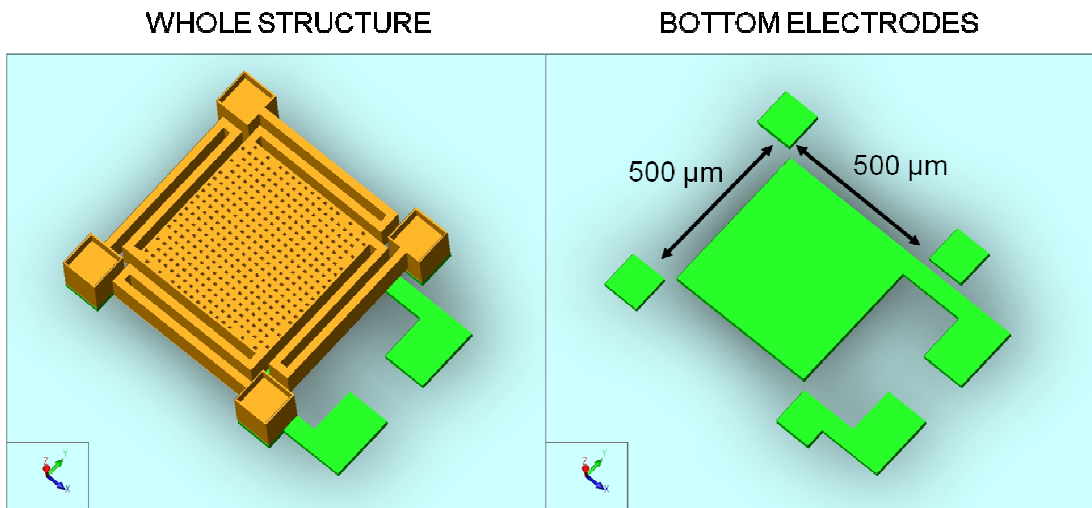


Fig. D.1 Accelerometer device layout on the die



a)

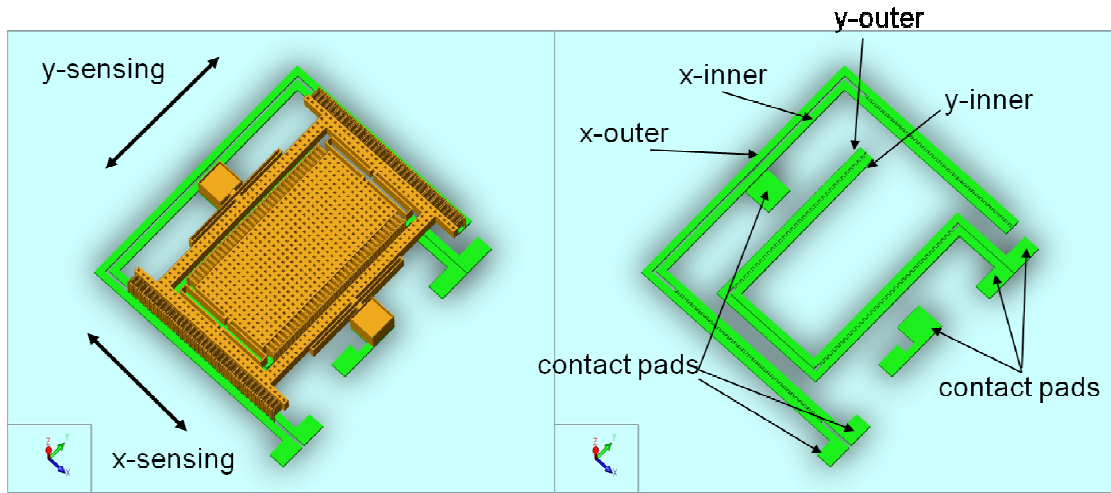


b)

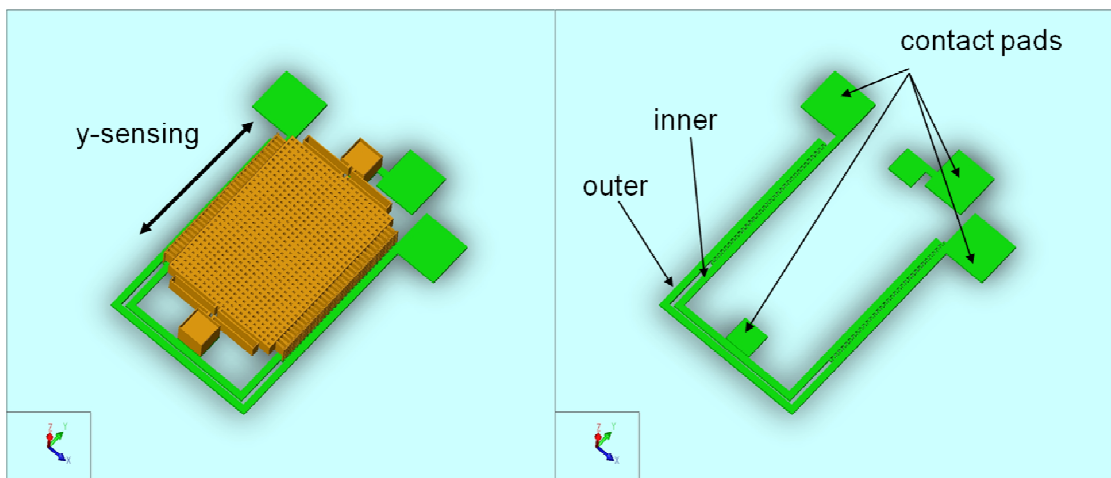
Fig. D.2 Designed z-axis accelerometers a) Device 1 b) Device 2

Table D.1 Structural properties of designed z-axis accelerometers

Structure	Length (μm)	Width (μm)	Perforations (μm)	Number of Perforations	Thickness (μm)
Device 1	650	650	10 x 10	676	5
Device 2	500	500	9 x 9	380	5

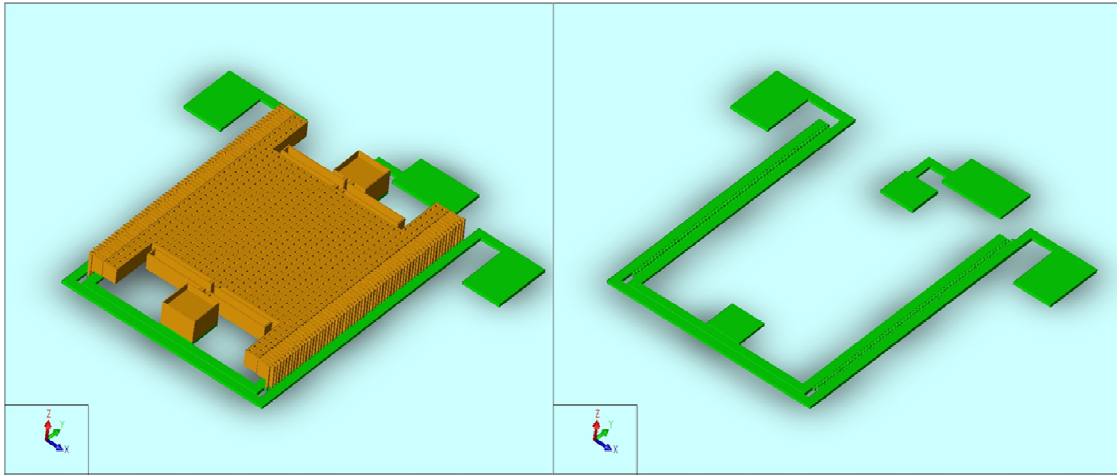


a)

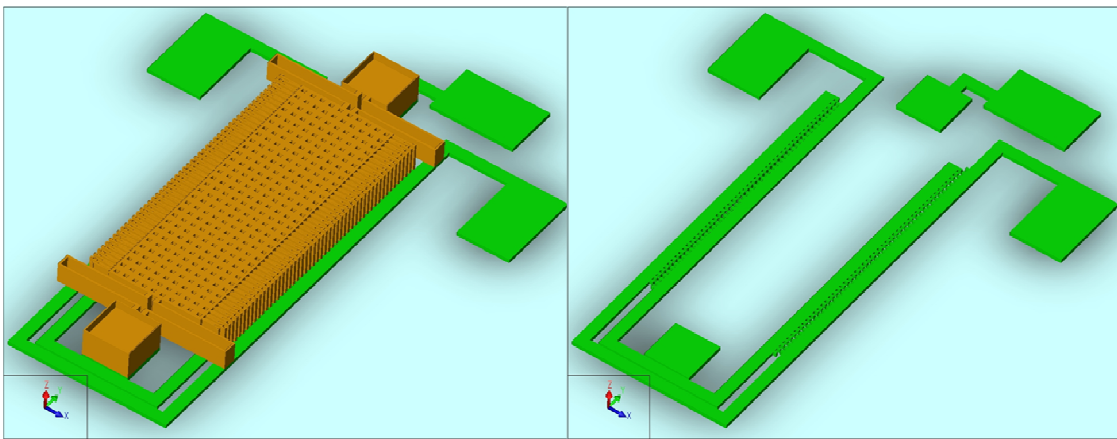


b)

Fig. D.3 Different types of lateral axis accelerometers a) Device 3 b) Device 4a, 4b



a)



b)

Fig. D.4 Different types of lateral axis accelerometers a) Devices 5a, 5b b) Devices 6a, 6b

Table D.2 Structural properties of integrated x,y-axis accelerometer (Device 3)

Structure	Length (μm)	Width (μm)	Perforations (μm)	Number of Perforations (μm)	Thickness (μm)	Effective comb length (μm)	Number of combs
x-sensing	1605	1281	20 x 20	725	5	71	72
y-sensing	1550	910	20 x 20	465	5	75	68

Table D.3 Structural properties of single axis lateral accelerometers

Structure	Length (μm)	Width (μm)	Perforations (μm)	Number of Perforations (μm)	Thickness (μm)	Effective comb length (μm)	Number of combs
Device 4a, 4b	1605	1281	20 x 20	704	5	81	66
Device 5a, 5b	1900	1338	20 x 20	632	5	64	128
Device 6a, 6b	1500	632	20 x 20	300	5	61	100

APPENDIX E

ACCELEROMETER SIMULATION SETTINGS AND CALCULATIONS

E.1 Introduction

Various simulations were performed to analyze the performance of accelerometers. This appendix describes the procedure for accelerometer simulations, and the parameters used.

E.2. Procedure for Simulations

Before starting the simulations, first the layout and process flow were built to create a 3-D model as explained in Appendix B. A number of simulations were done to analyze the structures.

First, spring constant simulations were performed using SpringMM module of Coventorware™. Initially, a 3-D model was created only for the spring as shown in Fig. E.1.

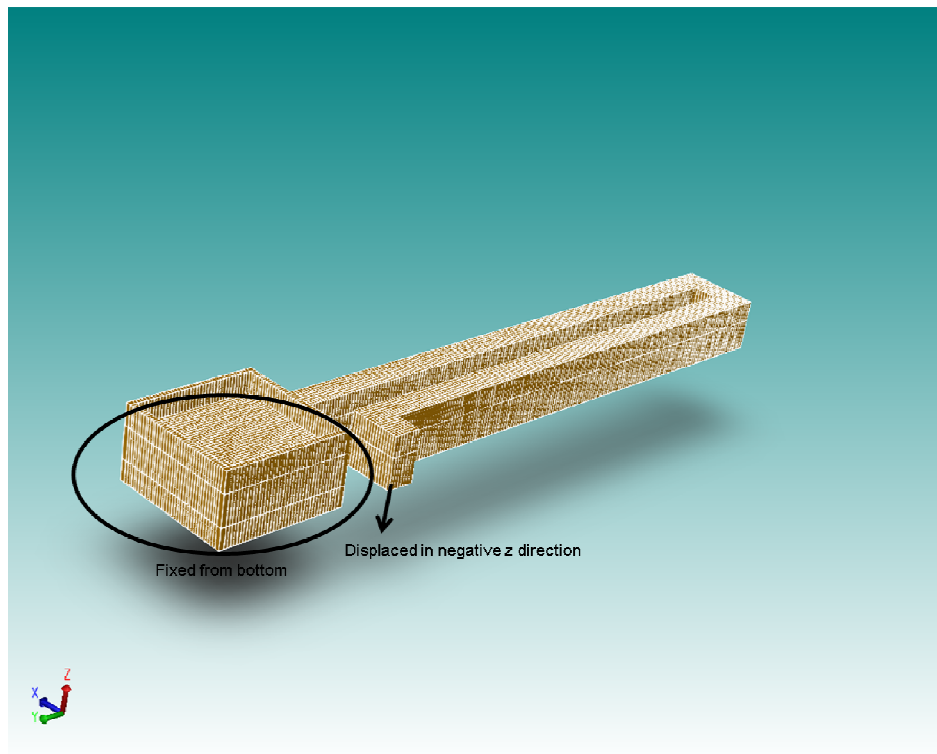


Fig. E.1 Solid model of the spring to determine z-axis spring constant. Boundary conditions are shown on the image

Then, the structure was meshed. For accelerometer simulations, Manhattan bricks with parabolic elements were used as mesh structure. Mesh size was kept at 3 μm for spring constant, damping and inertia simulations while it was increased up to 20 μm for capacitance simulations along all axes. It was made such that the mesh size was small enough for the calculations to converge.

For the simulation settings, a mechanical spring of nonlinear, single-ended type was considered. All 3 degrees of freedom were maintained for full factored analysis.

The boundary conditions of SpringMM consists of three parts, in the first part, the fixed parts were defined. In the second part, displaced parts were defined and in the final part, distance and steps for a specific displacement direction were given. For the simulations, the spring was displaced in z direction between $\pm 0.2 \mu\text{m}$ in 4 steps.

Following spring constant, mass of the structures was determined using InertiaMM module. For the mass analysis, only the moving part of the accelerometer was taken into account and springs were ignored as shown in Fig. E.2.

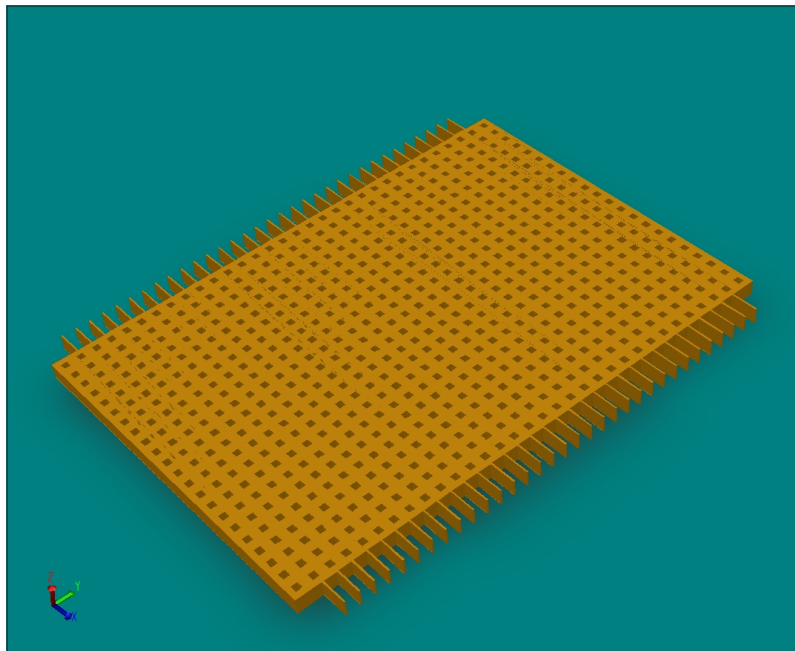


Fig. E.2 Solid model created for mass and damping simulations. Springs are not included

Afterwards, damping simulations were performed using DampingMM module. For damping simulations, same structures as those used for mass simulations were used.

Squeezed film and slide film damping analyses were performed to investigate the damping behavior of the accelerometers. The damping settings are shown in Fig. E.3.

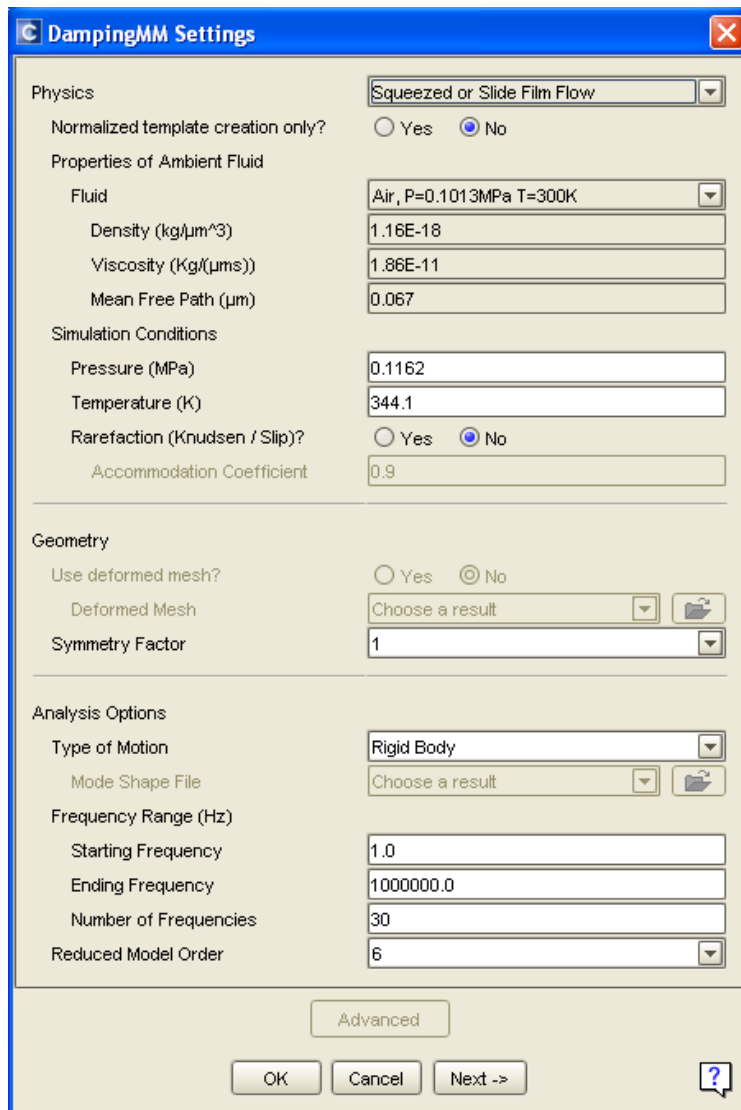


Fig E.3 Initial settings for the damping analysis

For z-axis accelerometers, only squeezed film damping was considered. The bottom of the proof mass was taken as squeeze surface with the sacrificial layer thickness as squeeze distance. The damping surface parameters for squeezed film damping of the z-axis accelerometers are shown in Fig. E.4.

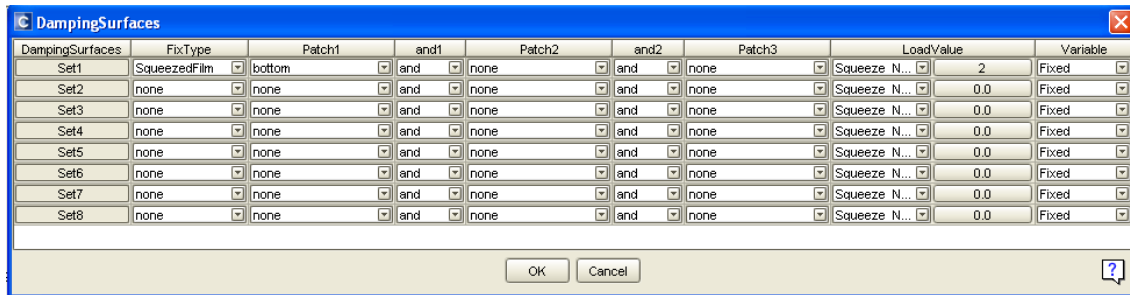


Fig. E.4 Damping surface used for squeezed film damping simulations of z-axis accelerometers

To setup edge boundary conditions, both edge and perforation corrections were taken into account. The value given in Fig. E5 for perforation correction is the radius of one perforation.



Fig. E.5 Boundary conditions for squeezed film damping for z-axis accelerometers

For lateral accelerometers, both squeezed and slide film dampings were taken into account. For squeezed film damping, the damping surfaces were the surfaces of moveable combs and the squeeze distance was taken as 2 μm , which is the initial gap between moving

and stationary combs as shown in Fig. E.6. Only edge correction was applied since the perforations are perpendicular to the direction of movement.

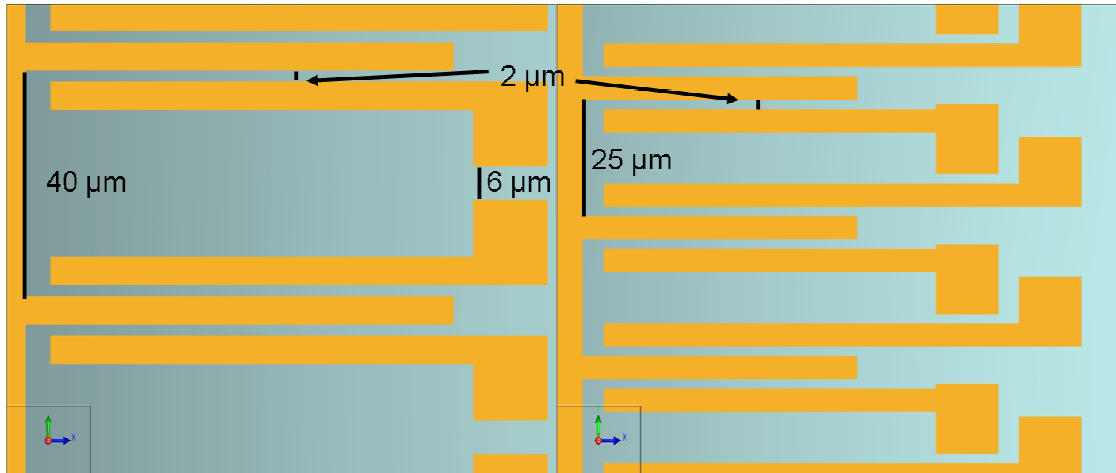


Fig. E.6 Illustration of two different comb structures used to detect acceleration in lateral axes. The distance between fixed and moveable combs is 2 μm

For slide film damping, the bottom surface was taken as damping surface with the size of gap taken as the thickness of sacrificial layer. No boundary conditions were applied for the edge.

Finally, capacitance simulations were performed using CoSolveEM module. CoSolveEM module couples MemMech with MemElectro. Thus, parameters and boundary conditions needed to be set both in MemMech and CoSolveEM. First, a solid model for capacitance measurements was created as shown in Fig. E.7. Then, MemMech parameters were set. In the module settings, mechanical analysis was selected. Simulations were done assuming linear and steady state properties without any additional analysis. Next, the surface boundary conditions were set by fixing the anchors and bottom of interconnect metallization on the solid model as shown in highlight in Fig. E.8.

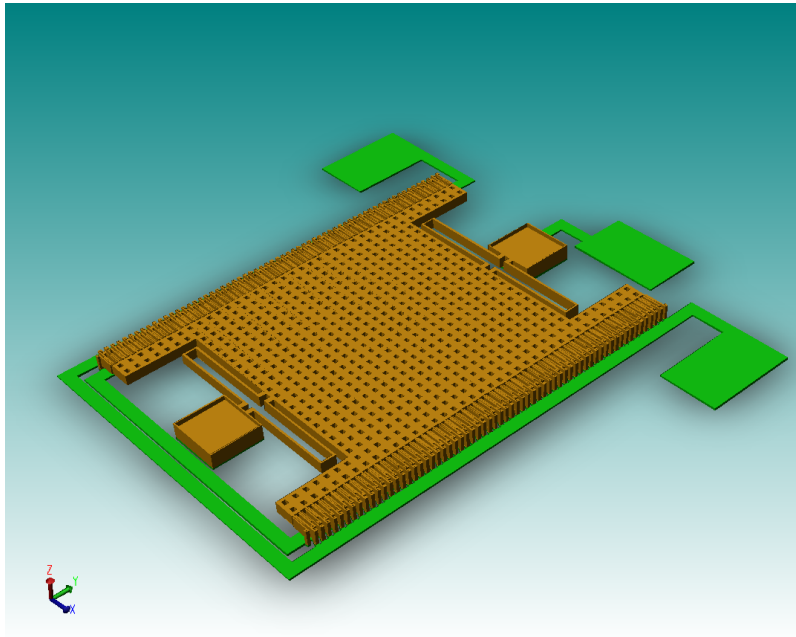


Fig. E.7 Solid model for capacitance simulations

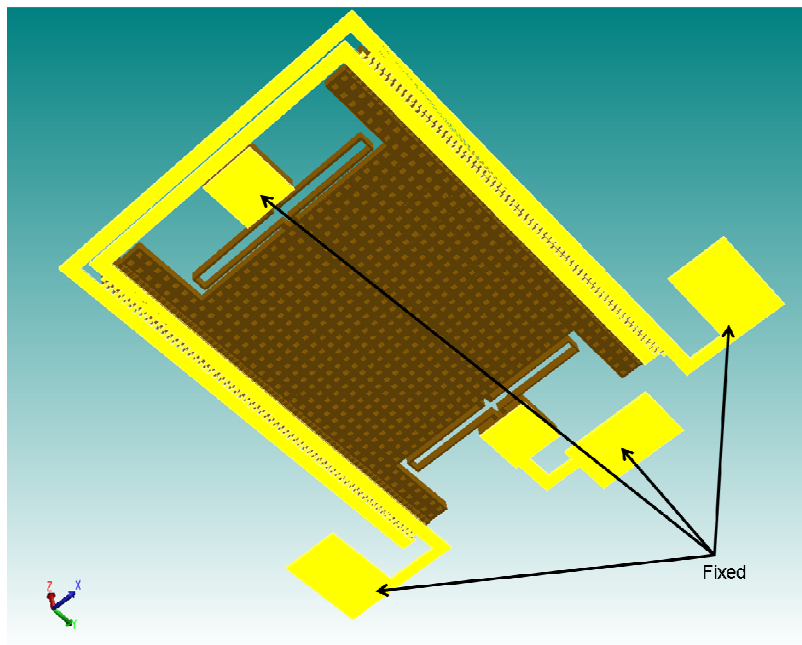


Fig. E.8 Fixed surfaces at the bottom of the solid model for capacitance simulations. All anchors, bond pads and metal interconnects were fixed

Afterwards, the volume boundary conditions were set to apply acceleration in the direction of sense.

CoSolveEM analysis was performed by single step analysis using a relaxation iteration method. As an independent variable, voltage was used. In the boundary conditions, dielectric and symmetry were ignored since neither of those was used. In the conductor boundary conditions, all conductors were fixed and a potential difference of 1 V was applied between the proof mass and metallization layers.

E.3 Design of Mask Layouts

The masks used in accelerometer fabrication are shown in Figs. E.9-E.12. All of the masks have light field polarity.

E.4 Calculations

Using the results obtained from simulations, several parameters were calculated. The calculations and equations used are explained in Chapter 3. The results of all calculations are given in Table E.1.

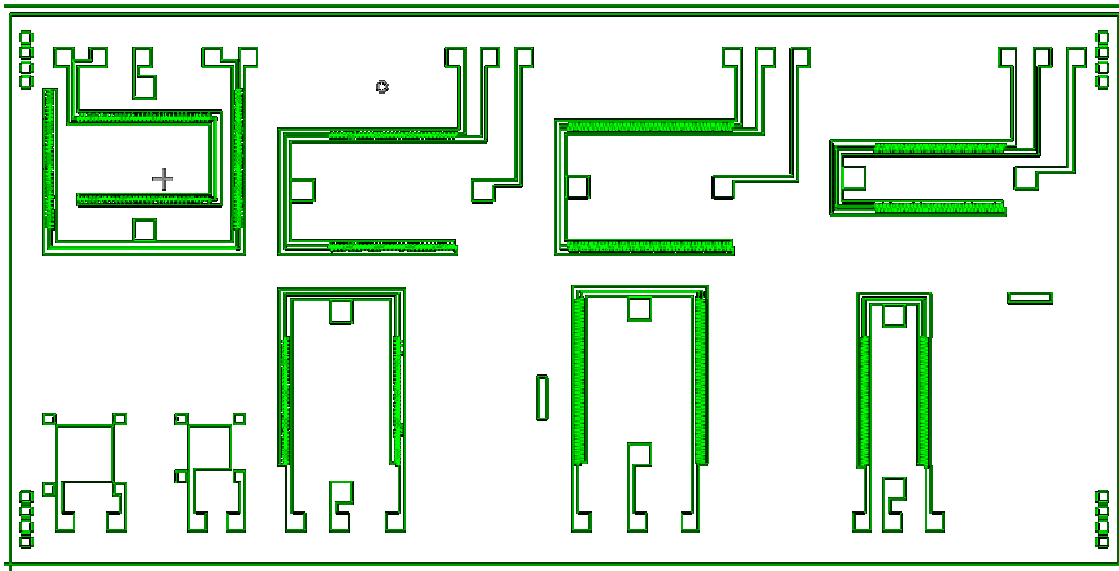


Fig. E.9 Metallization mask to create metal interconnects

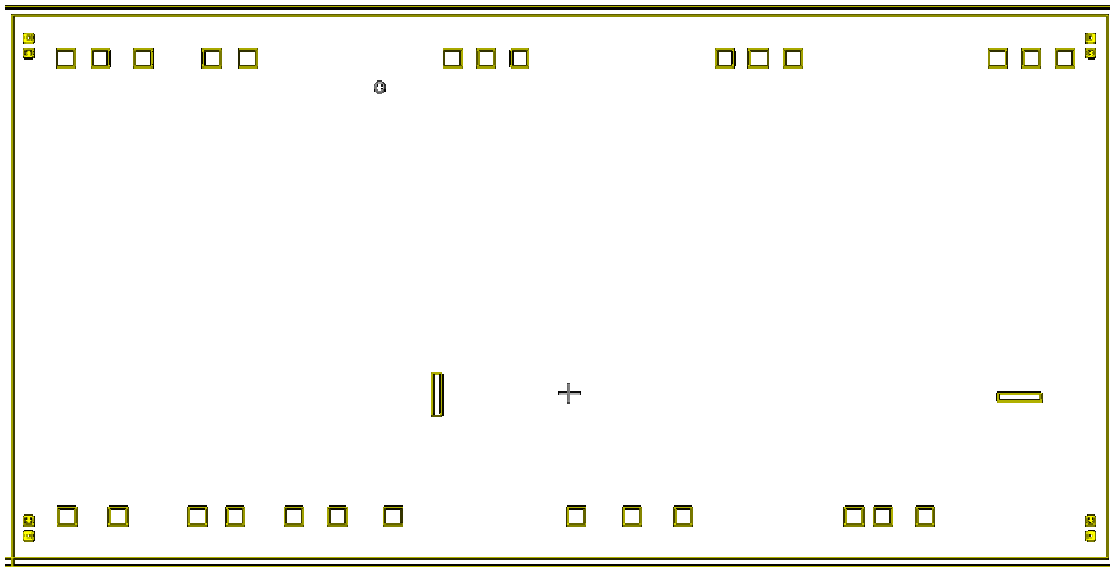


Fig. E.10 Bond pad mask to create bond pads

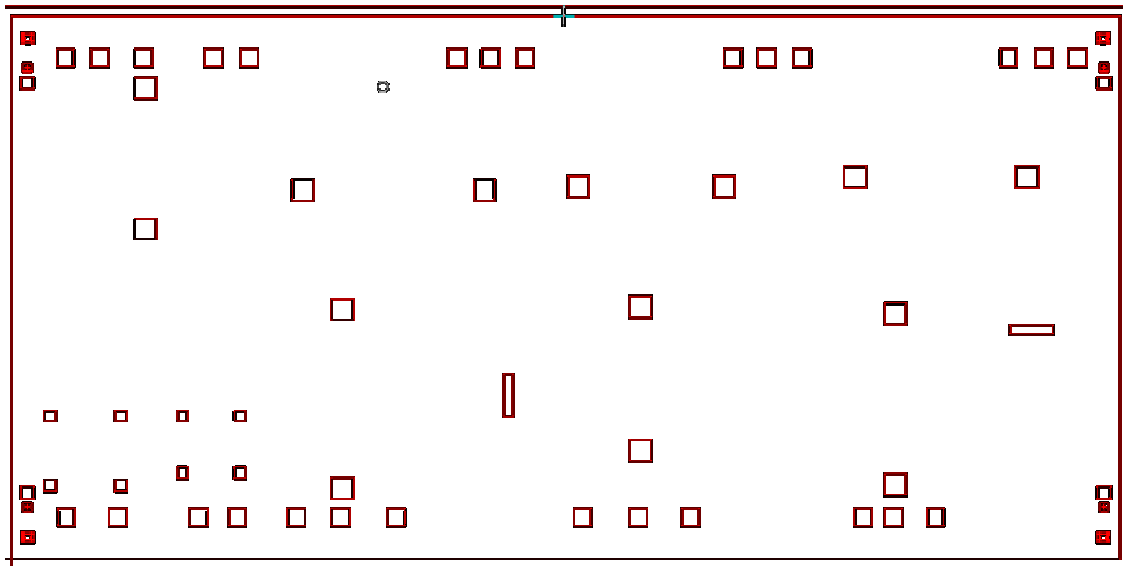


Fig. E.11 Sacrificial mask to pattern sacrificial layer

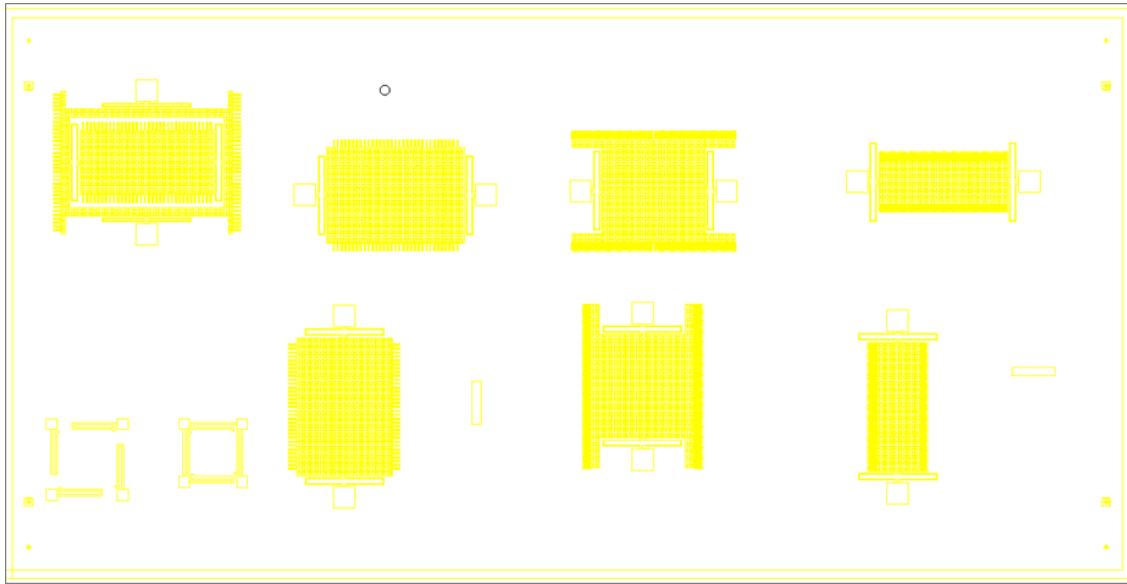
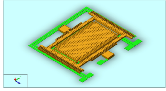
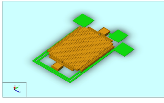
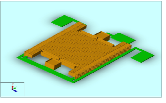
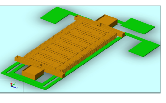
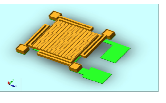
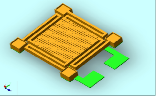


Fig. E.12 Mold mask to pattern mold photoresist before electroplating

Table E.1 Data obtained from simulations and calculations. The spring constant data marked with (*) were obtained from displacement using Eq. 3.2.

								
		X, Y INTEGRATED		X AND Y- AXIS	X AND Y- AXIS	X AND Y- AXIS	Z-AXIS 650X650 μm	Z-AXIS 500X500 μm
		x-axis	y-axis					
Spring Constant (N/m)		12.351*	24.794*	24.063 (24.223)*	24.063 (24.230)*	24.063 (23.723)*	10.118 (7.998)*	10.118 (7.488)*
Damping Ratio	-40 °F	0.553	0.545	0.548	0.559	0.543	0.550	0.553
	60 °F	0.661	0.651	0.655	0.668	0.649	0.658	0.661
	160 °F	0.756	0.745	0.749	0.764	0.742	0.753	0.756
Frequency (kHz)		13.086	23.549	18.799	19.846	28.541	25.297	32.188
Rest capacitance (pF)	inner	0.332	0.532	0.386	0.5573	0.447	1.894	1.125
	outer	0.199	0.732	0.230	0.3184	0.276		
ΔC (fF/g)	inner	3.808	0.975	2.05	2.7	1.016	18.08	6.648
	outer	3.635	1.160	2.045	2.6	1.011		
Mass (kg)		$7.213 \cdot 10^{-8}$	$4.471 \cdot 10^{-8}$	$6.809 \cdot 10^{-8}$	$6.109 \cdot 10^{-8}$	$2.954 \cdot 10^{-8}$	$1.581 \cdot 10^{-8}$	$9.766 \cdot 10^{-9}$

APPENDIX F
RESPONSE CHARACTERIZATION RESULTS OF ACCELEROMETERS

F.1 Introduction

After ashing and packaging, response characterizations were performed on select accelerometers. Response characterizations were performed by shaking each sample on a shaker plate which was excited at a frequency of 782 Hz. The output voltages were recorded and converted into capacitance change using Eq. 3.6. The results of response measurements are given below. For each graph, the type of the device, which were illustrated in Fig. D.3. of Appendix D is written in parentheses next to the sensitivity value.

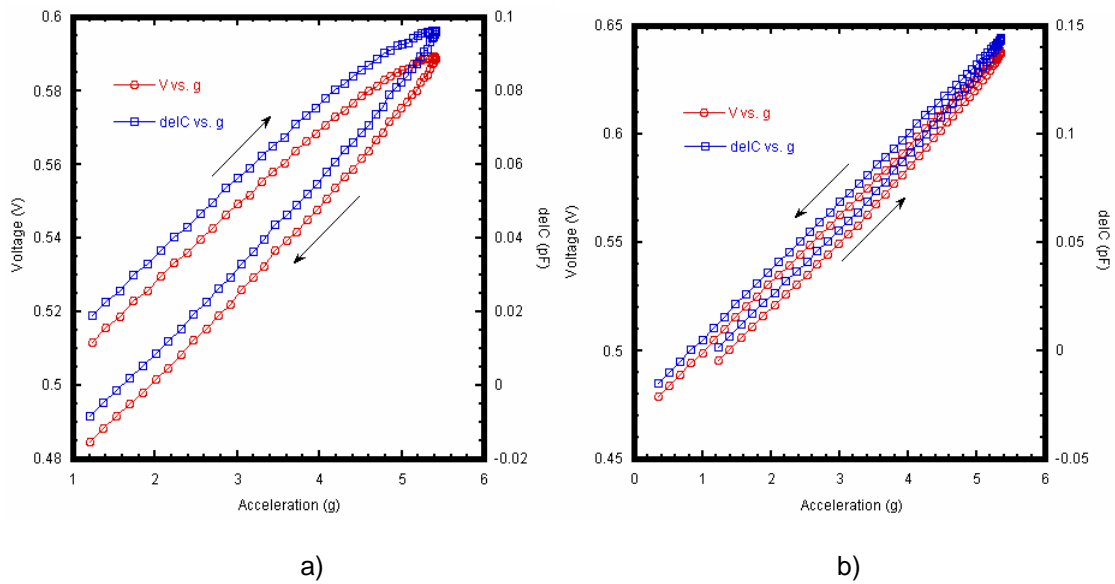


Fig. F.1 Voltage and capacitance response of the z-axis accelerometers on Si substrate. Capacitance change is a) 21.9 fF/g (Device 2) b) 32.4 fF/g (Device 1)

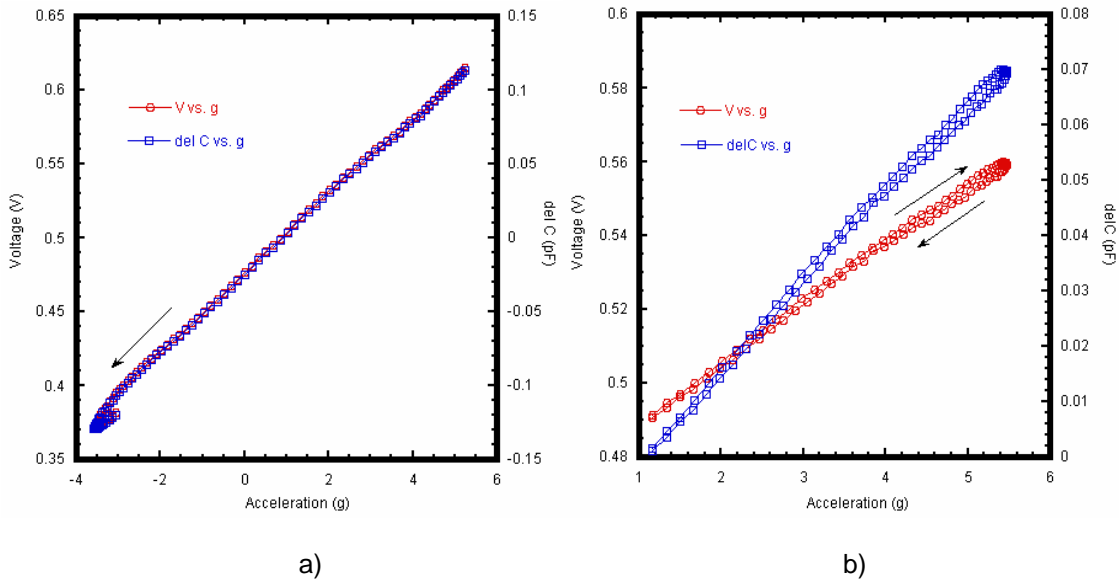


Fig. F.2 Voltage and capacitance response of the z-axis accelerometers on Si substrate. Capacitance change is a) 15.8 fF/g (Device 2) b) 15.8 fF/g (Device 1)

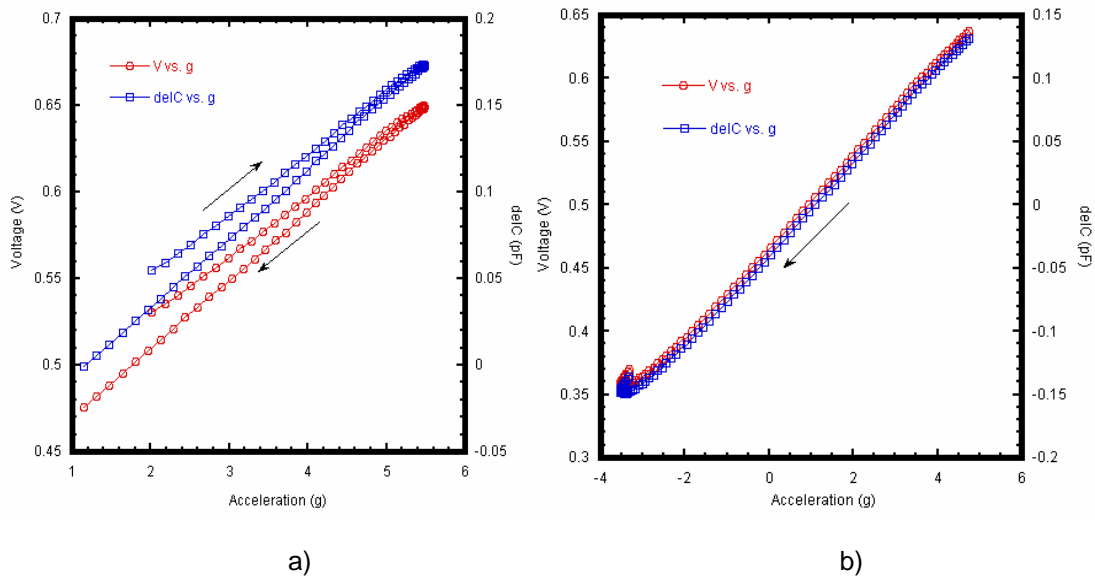


Fig. F.3 Voltage and capacitance response of the z-axis accelerometers on Si substrate. Capacitance change is a) 39 fF/g (Device 1) b) 34.5 (Device 2)

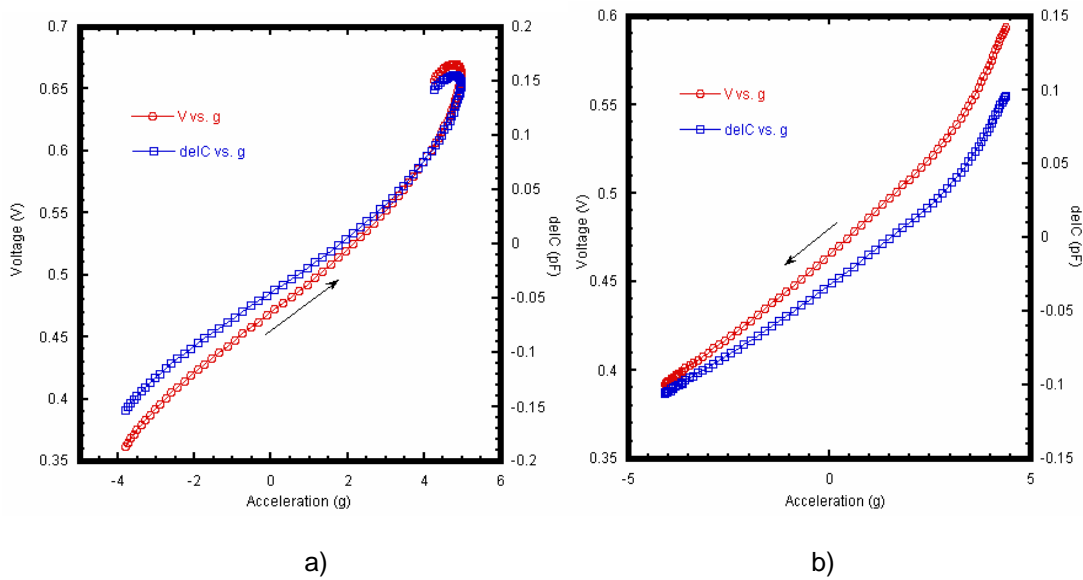


Fig. F.4 Voltage and capacitance response of the z-axis accelerometers on Si substrate. Capacitance change is a) 33.8 fF/g (Device 2) b) 22fF/g (Device 2)

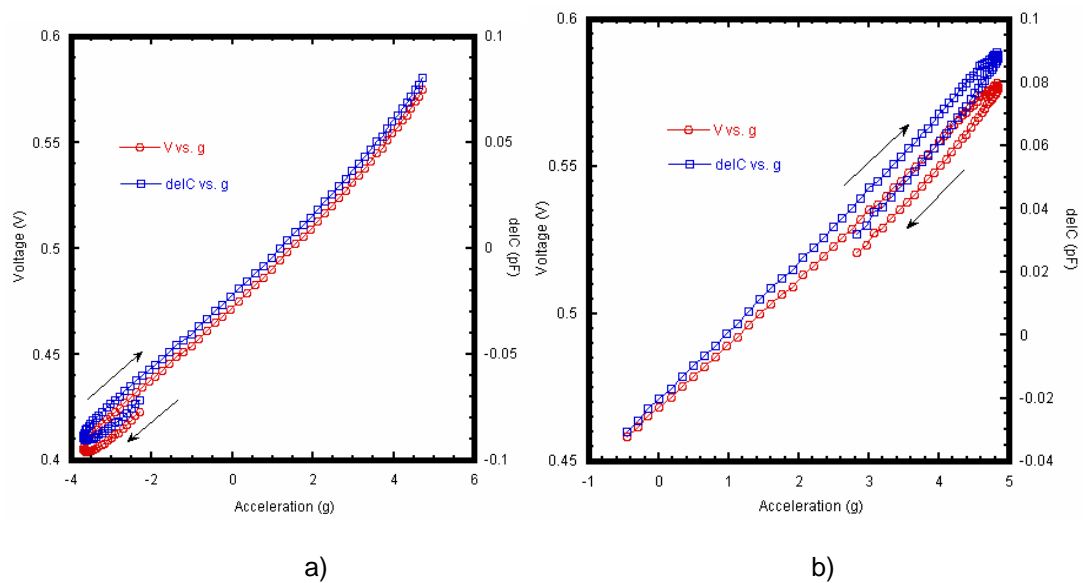


Fig. F.5 Voltage and capacitance response of the z-axis accelerometer on flexible polymer substrate. Capacitance change is a) 19.5 fF/g (Device 2) b) 22.4 fF/g (Device 2)

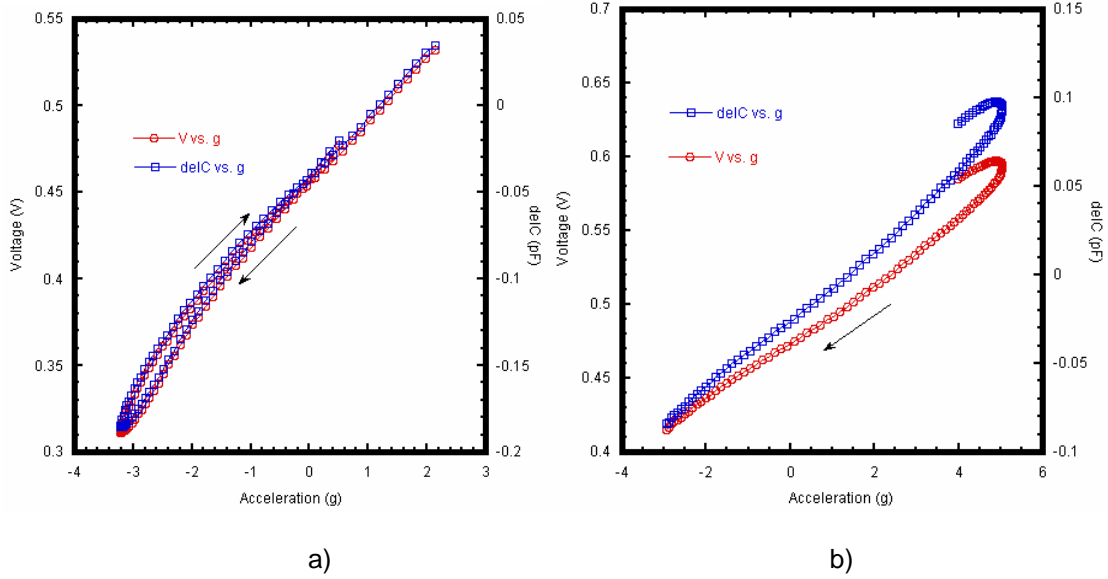


Fig. F.6 Voltage and capacitance response of the z-axis accelerometer on flexible polymer substrate. Capacitance change is a) 41.8 (Device 1) fF/g b) 22.5 fF/g (Device 2)

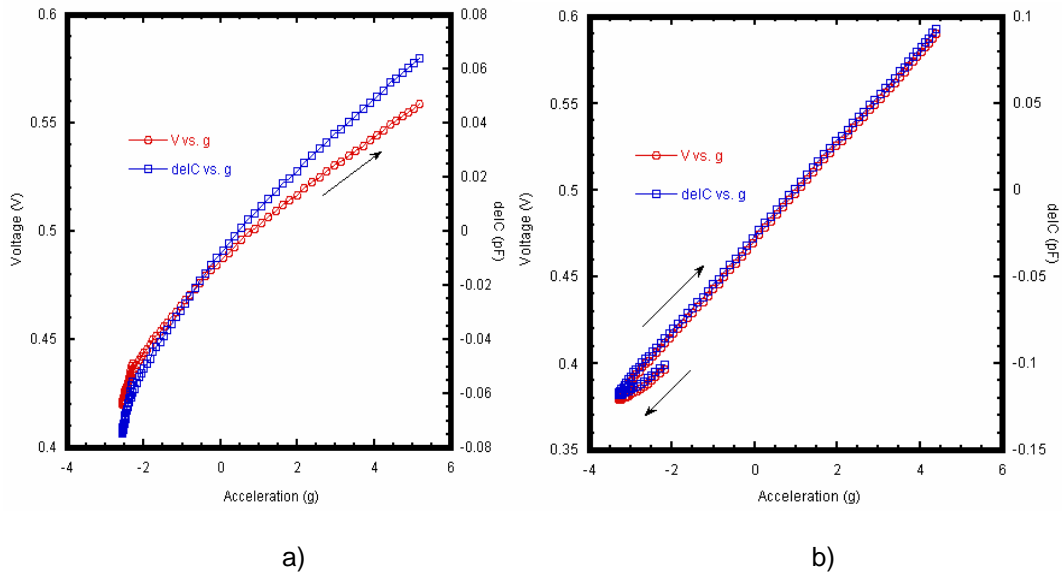


Fig. F.7 Voltage and capacitance response of the z-axis accelerometer on flexible polymer substrate. Capacitance change is a) 18.1 fF/g (Device 1) b) 27.7 fF/g (Device 2)

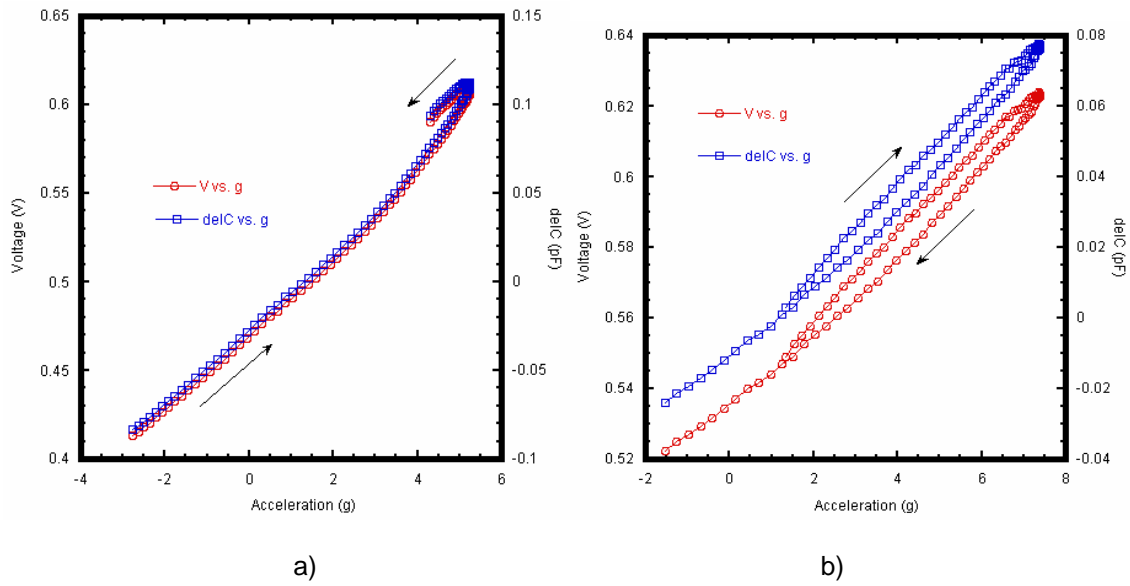


Fig. F.8 Voltage and capacitance response of the a) z-axis accelerometer on flexible polymer substrate b) x,y-axis accelerometer on Si substrate. Capacitance change is a) 25.2 fF/g (Device 1) b) 11.9 fF/g (Device 4b)

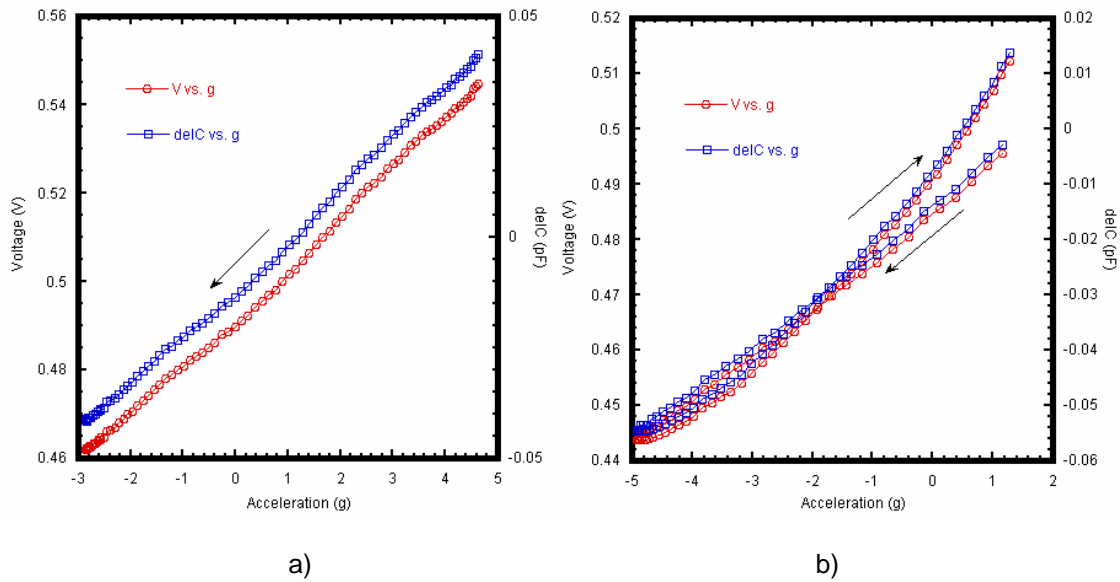


Fig. F.9 Voltage and capacitance response of the x,y-axis accelerometer on flexible polymer substrate. Capacitance change is a) 11 fF/g (Device 4b) b) 9.7 fF/g (Device 4a)

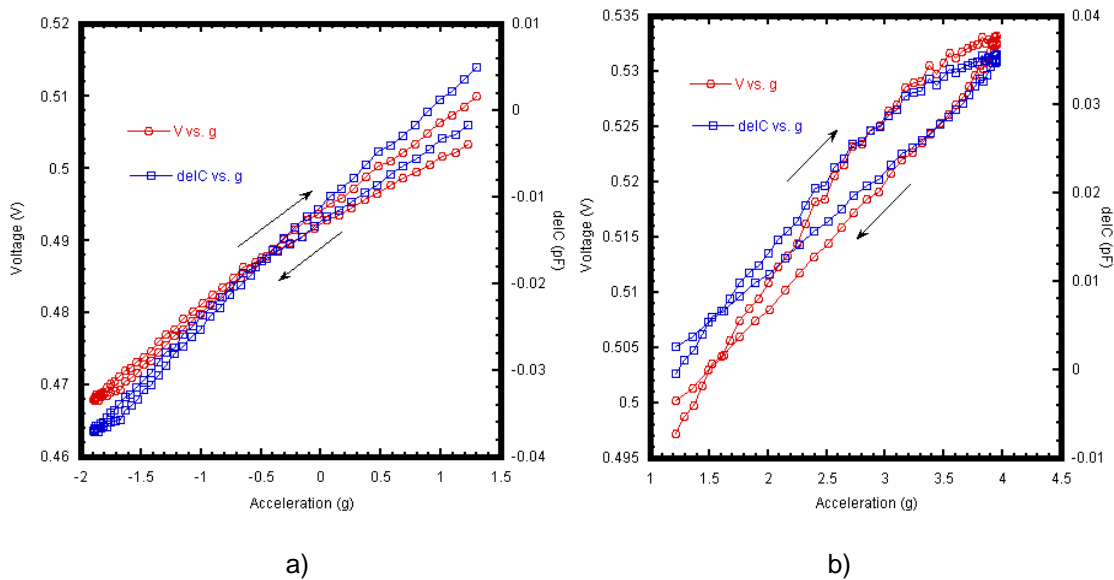


Fig. F.9 Voltage and capacitance response of the x,y-axis accelerometer on flexible polymer substrate. Capacitance change is a) 12.6 fF/g (Device 6b) b) 12.3 fF/g (Device 6a)

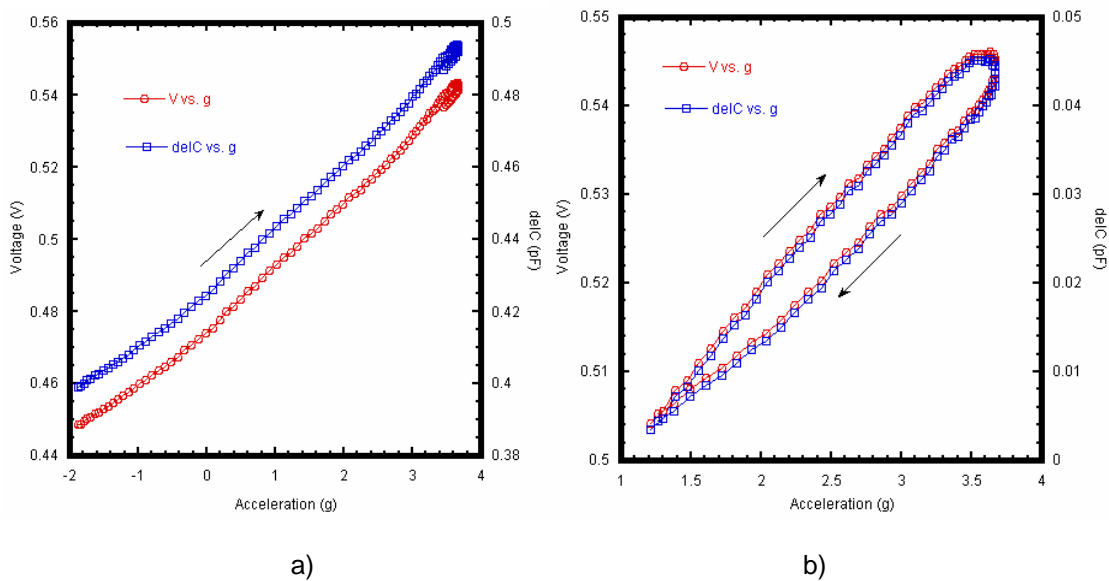


Fig. F.10 Voltage and capacitance response of the x,y-axis accelerometer on flexible polymer substrate. Capacitance change is a) 17.5 fF/g (Device 4b) b) 16.6 fF/g (Device 6a)

REFERENCES

- [1] T. Loher, R. Viero, M. Seckel, A. Ostmann, and H. Reichl, "Stretchable electronic systems for wearable and textile applications", *Proc. IEEE 9th VLSI Packaging Workshop in Japan*, pp. 9-12, 2008
- [2] H. -K. Lee, S. -I. Chang, and E. Yoon, "A flexible polymer tactile sensor: Fabrication and modular expandability for large area deployment", *J. Microelectromech. Sys.*, vol. 15, no. 6, pp. 1681-1686, December 2006
- [3] A. Albarbar, A. Badri, J. K. Sinha, and A. Starr, "Performance evaluation of MEMS accelerometers", *Measurement*, vol. 42, pp. 790-795, 2009
- [4] A. Albarbar, S. Mekid, A. Starr, and R. Pietruskiewicz, "Suitability of MEMS accelerometers for condition monitoring: An experimental study", *Sensors*, vol. 8, pp. 784-799, 2008
- [5] J. N. Schoess, D. Arch, W. Yang, C. Cabuz, B. Hocker, B. Johnson, and m. Wilson, "MEMS sensing and control: An aerospace perspective", in *Smart Structures and Materials 2000: Smart Electronics and MEMS*, *Proc. of SPIE*, vol. 3990, pp. 22-27, 2000
- [6] W. Tiju, A. Ahanchian, and B. Y. Majlis, "Development of tire condition monitoring systems (TCMS) based on MEMS sensors", in *Proc. IEEE Conf. Semiconductor Electronics*, pp.350-353, 2004
- [7] J. S. Kim, K. J. Vinoy, and V. K. Varadan, "Wireless health monitoring of cracks in structures with MEMS-IDT sensors", in *Smart Structures and Materials 2000: Smart Electronics and MEMS*, *Proc. of SPIE*, vol. 4700, pp. 342-353, 2002
- [8] C. U. Grosse, S. D. Glaser, and M. Kruger, "Condition monitoring of concrete structures using wireless sensor networks and MEMS", in *Smart Structures and Materials 2006: Sensors and Smart Structures Technologies for Civil, Mechanical, and Aerospace Systems*, *Proc. Of*

SPIE, vol. 6174, pp. 407-418, 2006

- [9] J. Engel, J. Chen, and C. Liu, "Development of polyimide flexible tactile sensor skin", *J. Micromech. Microeng.*, vol.13, pp. 359-366, 2003
- [10] Z. Celik-Butler and D. P. Butler, "Flexible sensors-A review", *J. Nanoelectron. Opt.*, vol.1, pp. 194-202, 2006
- [11] P. Liu, R. Zhu, and R. Que, "A flexible flow sensor system and its characteristics for fluid mechanics measurements", *Sensors*, vol. 9, pp. 9533-9543, 2009
- [12] M. E. Kiziroglou, C. He, and E. M. Yeatman, "Flexible substrate electrostatic energy harvester", *Electron. Lett.*, vol. 46, no.2, pp. 166-167, January 2010
- [13] J. Smith, R. Hamilton, I. McCulloch, M. Heeney, J. E. Anthony, D. D. C. Bradley, and T. D. Anthopoulos, "High mobility p-channel organic field effect transistors on flexible substrates using a polymer-small molecule blend", *Synthetic Metals*, vol. 159, pp. 2365-2367, 2009
- [14] H. Ho and J. L. Skinner, "Fabrication methods for creating flexible polymer substrate sensor tags", *J. Vac. Sci. Technol. B*, vol. 27, no. 6, pp. 3104-3108, Nov/Dec 2009
- [15] A. Mahmood, D. P. Butler, and Z. Celik-Butler, "Miromachined bolometers on polyimide", *Sensors and Actuators A*, vol. 132, pp. 452-459, 2006
- [16] S. A. Dayeh, D. P. Butler, and Z. Celik-Butler, "Micromachined infrared bolometers on flexible polyimide substrates", *Sensors and Actuators A*, vol. 118, pp. 49-56, 2005
- [17] V. Vong and A. Salleo, *Flexible electronics: Materials and applications*, Springer Science and Business Media, New York, NY, USA, 2009
- [18] M. D. J. Auch, O. K. Soo, G. Ewald, and C. Soo-Jin, "Ultrathin glass for flexible OLED application", *Thin Solid Films*, vol. 417, no. 1-2, pp. 47-50, September 2002
- [19] Y. H. Kim, S. K. Park, D. G. Moon, W. K. Kim, and J. I. Han, "Organic thin film transistor-driven liquid crystal displays on flexible polymer substrate", *Jap. J. Appl. Phys.*, vol. 43, no. 6a, pp. 3605-3608, 2004

- [20] J. H. Cheon, J. H. Bae, and J. Jang, "Mechanical stability of poly-Si TFT on metal foil", *Solid-State Electron.*, vol. 52, no. 3, pp. 473-477, 2008
- [21] S. Wagner, H. Gleskova, I-C. Cheng, and J. C. Sturm, "Mechanics of TFT technology on flexible substrates", in *Flexible Flat Panel Displays*, edited by G. P. Crawford, Wiley Imprint, 2005
- [22] S. U. Jen, C. C. Yu, C. H. Liu, and G. Y. Lee, "Piezoresistance and electrical resistivity of Pd, Au, and Cu films", *Thin Solid Films*, vol. 434, Iss. 1-2, pp. 316-322, June 2003
- [23] K. Saejok, B. Phinyo, E. Chaowicharat et.al, "Effect of temperature to characteristics of polysilicon based surface micromachining piezoresistive pressure sensor", *IEEE Proc. Of ECTI-CON*, pp. 813-816, 2008
- [24] C. S. Smith, "Piezoresistance effect in germanium and silicon", *Phys. Rev.*, vol. 94, no. 1, pp. 42-49, 1954
- [25] E. N. Adams, "Elastoresistance in p-type Ge and Si", *Phys. Rev.*, vol. 96, no. 3, pp. 803-804, 1954
- [26] C. J. Reilly and J. E. Sanchez, Jr, "The piezoresistance of aluminum alloy interconnect structures", *J. Appl. Phys.*, vol. 85, no. 3, pp. 1943-1948, February 1999
- [27] C. Hu, Y. Gao, and Z. Sheng, "The piezoresistance coefficients of copper and copper-nickel alloys", *J. Mat. Sci.*, vol. 35, pp. 381-386, 2000
- [28] A. A. Barlian, W. -T. Park, J. R. Mallon, Jr, A. J. Rastegar, and B. L. Pruitt, "Review: Semiconductor piezoresistance for Microsystems", *Proc. IEEE*, vol. 97, no. 3, pp. 513-552, March 2009
- [29] A. L. Window and G. S. Holister, *Strain gauge technology*, Applied Science Publishers, London and New Jersey, 1982
- [30] P. J. French and A. G. R. Evans, "Polycrystalline silicon as a strain gauge material", *J. Phys. E.: Sci. Instrum.*, vol. 19, pp. 1055-1058, 1986
- [31] S. Sze, *Semiconductor Sensors*, John Wiley & Sons, Inc., New York, 1994

- [32] P. J. French, "Polysilicon: a versatile material for microsystems", *Sensors and Act. A*, v.99, pp. 3-12, 2002
- [33] C. H. Choi, P. R. Chidambaram, R. Khamankar et.al., "Gate length dependent polysilicon depletion effects", *IEEE Electron Device Lett.*, vol. 23, no.4, pp. 224-226, 2002
- [34] L. Wang and D. J. Beebe, "A Silicon-based shear force sensor: development and characterization", *Sensors and Actuators*, vol. 84, pp. 33-44, 2000
- [35] H. Sandmaier and K. Kühn, "A square-diaphragm piezoresistive pressure sensor with a rectangular central boss for low-pressure ranges", *IEEE Trans. Electron Devices*, **40**, pp. 1754-1759, 1993
- [36] K. Kwon and S. Park, "Three axis piezoresistive accelerometer using polysilicon layer", *IEEE Proceedings of International Conference on Solid State Sensors and Actuators*, vol. 2, pp. 1221-1224, 1997
- [37] V. A. Gridchin, V. M. Lubimsky and M. P. Sarina, "Piezoresistive properties of polysilicon films", *Sensors and Actuators A*, vol. 49, pp. 67-72, 1995
- [38] M. M. Mandurah, K. C. Saraswat and T. I. Kamins, "A model for conduction in polycrystalline silicon-part 1: Theory", *IEEE Trans. Electron. Devices*, vol. ED-28, no 10, pp. 1163-1171, 1981
- [39] T. Kamins, *Polycrystalline silicon for integrated circuit applications*, Kluwer Academic Publishers, Boston, MA, USA, 1988
- [40] A. L. Fripp and R. L. Stermer, "Resistivity of doped polycrystalline silicon films", *J. of Electrochem. Soc.*, vol. 117, pp. 1569, 1970
- [41] M. E. Cowher and T. O. Sedgwick, "Chemical vapor deposited polycrystalline silicon", *J. of Electrochem. Soc.*, vol. 119, pp. 1565-1571, 1972
- [42] M. Mandurah, K. C. Saraswat, C. R. Helms and T. I. Kamins, "Dopant segregation in polycrystalline silicon", *J. Appl. Phys.*, vol. 51, pp. 5755-5763, 1980
- [43] Mandurah, K. C. Saraswat and T. I. Kamins, "Arsenic segregation in polycrystalline silicon", *Appl. Phys. Lett.*, vol. 36, pp. 683-685, 1980

- [44] P. J. French and A. G. R. Evans, "Piezoresistance in polysilicon and its application to strain gauges", *Solid-State Electron.*, vol.32, no.1, pp. 1-10, 1989
- [45] M. M. Mandurah, K. C. Saraswat ad T. I. Kamins, "A model for conduction in polycrystalline silicon-part 2: Comparison of theory and experiment", *IEEE Trans. Electron. Devices*, vol. ED-28, no 10, pp. 1171-1176, 1981
- [46] F. A. Padovani and R. Stratton, "Field and thermionic-field emission in Schottky barriers", *Solid State Electronics*, vol. 9, pp. 695-707, 1966
- [47] C. R. Crowell and S. M. Sze, "Current transport in metal-semiconductor barriers", *Solid State Electronics*, vol. 9, pp. 1035-1048, 1966
- [48] M. L. Tarng, "Carrier transport in oxygen-rich polycrystalline-silicon films", *J. Appl. Phys.*, vol. 49, pp. 4069-4075, 1978
- [49] D. P. Joshi and R. S. Srivastava, "A model of electrical conduction in polycrystalline silicon", *IEEE Trans. Electron. Devices*, vol. ED-31, no. 7, pp. 920-926, 1984
- [50] Y. Kanda, "A graphical representation of he piezoresistance coeffieceients in silicon", *IEEE Trans. Electron. Devices*, vol. ED-29, no.1, pp. 64-70, 1982
- [51] D. Sands, G. Williams, and P. H. Key, "Excimer laser recrystallization of amorphous silicon investigated by normal incidence spectral reflectivity", *Semicond. Sci. Technol.*, vol. 12, pp. 750-754, 1997
- [52] H. T. G. Hentzeli, A. Robertsson, et.al., "Formation of aluminum silicide between two layers of amorphous silicon", *Appl. Phys. Lett.*, vol. 50, pp. 933-934, 1987
- [53] T. Antesberger, C. Jaeger, M. Scholz and M. Stutzman, "Structural and electronic properties of ultrathin polycrystalline Si layers on glass prepared by aluminum-induced layer exchange", *App. Phys. Lett.*, vol. 91, article no. 201909, 2007
- [54] W. Knaepen, C. Detavernier et.al., "In-situ x-ray diffraction study of metal induced crystallization of amorphous silicon", *Thin Solid Films*, vol. 516, pp. 4946-4952, 2008

- [55] K. S. Hsu, J. Ou-Yang, L. P. Ren and G. Z. Pan, "Aluminum-induced crystallization of PECVD amorphous silicon at 120 °C", *Electrochem. Solid State Lett.*, vol.10, pp. H365-H367, 2007
- [56] N. Yazdi, F. Ayazi and K. Najafi, "Micromachined inertial sensors", *Proceedings of the IEEE*, vol. 86, no.8, pp. 1640-1659, 1998
- [57] J. W. Gardner, V. K. Varadan and O. O. Awadelkarim, *Microsensors, MEMS and Smart Devices*, John Wiley and Sons, 2005
- [58] G. Gerlach and W. Doetzel, *Introduction to Microsystem technology*, John Wiley and Sons, 2008
- [59] V. Ostasevicius, R. Dauksevicius, R. Gaidys and A. Palevicius, "Numerical analysis of fluid-structure interaction effects on vibrations of cantilever microstructure", *J. Sound and Vibration*, vol. 308, pp. 660-673, 2007
- [60] M. Bao, *Analysis and Design Principles of MEMS Devices*, Elsevier, 2005
- [61] M. Bao and H. Yang, "Squeeze film air damping in MEMS", *Sensors and Actuators A*, vol. 136, pp. 3-27, 2007
- [62] N. Kanani, *Electroplating*, Elsevier, 2004
- [63] J. Zhou, S. Dasgupta, H. Kobayashi, J. M. Wolff, H. E. Jackson, and J. T. Boyd, "Optically interrogated MEMS pressure sensors for propulsion applications", *Opt. Eng.*, vol. 40, pp. 598-604, April 2001
- [64] N. K. S. Lee, R. S. Goonetilleke, Y. S. Cheung, and G. M. Y. So, "A flexible encapsulated MEMS pressure sensor system for biomechanical applications", *Microsys. Tech.*, vol. 7, pp. 55-62, 2001
- [65] G. Blasquez, P. Pons, and A. Boukabache, "Capabilities and limits of silicon pressure sensors", *Sensors and Actuator*, vol. 17, pp. 287-403, 1989

- [66] D. W. Richerson and D. W. Freitag, Ceramics Industry, Metals and Ceramics Division, Oak Ridge National Laboratory, TN 37830,
<http://www.ms.ornl.gov/programs/energyeff/cfcc/iof/chap21-2sin.pdf>
- [67] S. Greek, F. Ericson, S. Johansson, M. Furtch, and A. Rump, "Mechanical characterization of thick polysilicon films: Young's modulus and fracture strength evaluated with microstructures", *J. Micromech. Microeng.*, vol. 9, pp. 245-251, 1999
- [68] R. L. Edwards, G. Coles, and W. N. Sharpe, Jr, "Comparison of tensile and bulge tests for thin-film silicon nitride", *Experimental Mech.*, vol. 44, no. 1, pp. 49-54, February 2004
- [69] S. K. Patil, Z. Celik-Butler and D. Butler, "Piezoresistive Polysilicon Film obtained by Low-Temperature Aluminum Induced Crystallization", *submitted to J. of Vac. Sci. Tech. B*
- [70] A. Boukabache, P. Pons, G. Blasquez and Z. Dibi, "Characterization and modeling of the mismatch of TCRs and their effects on the drift of the offset voltage of piezoresistive pressure sensors", *Sensors and Actuators*, vol. 84, pp. 292-296, 2000
- [71] S. K. Patil, Z. C. Butler, and D. P. Butler, "Microcrystalline piezoresistive polysilicon film obtained by aluminum induced crystallization", in *IEEE Nanotechnology 2008 Proc.*, pp. 767-770, 2008
- [72] B. Y. Majlis, K. Sooriakumar, S. Najdu, and B. Patmon, "Use of micro-machined accelerometer in today's world", in *Proc. IEEE Conf. Semiconductor Electronics*, pp.9-14, 2002
- [73] J. Chae, H. Kulah, and K. Najafi, "A monolithic three-axis micro-g micromachined silicon capacitive accelerometer", *J. Microelectromech. Sys.*, vol. 14, no. 2, pp. 235- 242, April 2005
- [74] C. Xue, S. Chen, H. Qiao, W. Zhang, J. Xiong, B. Zhang, and G. Zhang, "Development of a novel two axis piezoresistive micro accelerometer based on silicon", *Sensor Letters*, vol. 6, pp. 149-158, 2008
- [75] R. de Reus, J. O. Gullov, and P. R. Scheeper, "Fabrication and characterization of a piezoelectric accelerometer", *J. Micromech. Microeng.*, vol. 9, pp. 123-126, 1999

- [76] H. Farahani, J. K. Mills, and W. L. Cleghorn, "Design, fabrication and analysis of micromachined high sensitivity and 0% cross-axis sensitivity capacitive accelerometers", *Microsyst. Technol.*, vol. 15, pp. 1815-1826, 2009
- [77] B. E. Boser and R. T. Howe, "Surface micromachined accelerometers", *IEEE J. Solid State Cir.*, vol. 31, no. 3, pp. 366-375, March 1996
- [78] B. Chen, J. Miao, C. Lim, F. E. H. Tay, and C. Iliescu, "Dynamic behavior of high-g MEMS accelerometer incorporated with novel micro-flexures", *Int. J. Software Eng. & Knowldg. Eng.*, vol. 15, no. 2, pp. 225-230, 2005
- [79] H. Qu, D. Fang, and H. Xie, "A monolithic CMOS-MEMS 3-axis accelerometer with a low-noise, low-power dual-chopper amplifier", *IEEE Sensors*, vol. 8, no. 9, pp. 1511-1518, September 2008
- [80] F. D. Wall, M. A. Martinez, and J. J. Vandenavyle, "Corrosion behavior of structural nickel electrodeposit", *Microsystem Technologies*, vol. 11, pp. 319-330, 2005
- [81] M. Paz and W. Leigh, *Structural dynamics: Theory and computation*, Kluwer Academic Publishers, Norwell, MA, USA, 2004
- [82] R. W. Kotlowitz and I. M. Nevarez, "Compliance metric for the s-bend lead design for surface mount components, with application to clip-leads", in *Proc. Electron. Comp. and Tech. Conf.*, pp. 1104-1114, 1993
- [83] V. Saile, U. Wallrabe, O. Tabata, and J. G. Korvink, *LIGA and its applications*. Wiley-VCH Verlag, Weinheim, Germany, 2009
- [84] W.H. The, J. K. Luo, M. R. Graham, A. Pavlov, and C. G. Smith, "Near-zero curvature fabrication of miniaturized micromechanical Ni switches using electron beam cross-linked PMMA", *J. Micromech Microeng.*, vol 13, pp. 591-598, 2003
- [85] J. K. Luo, A. J. Flewitt, S. M. Spearing, N. A. Fleck, and W. I. Milne, "Young's modulus of electroplated Ni thin film for MEMS applications", *Materials Lett.*, vol. 58, pp. 2306-2309, 2004

- [86] J. K. Luo, M. Pritschow, A. J. Flewitt, S. M. Spearing, N. A. Fleck, and W. I. Milne, "Effect of process conditions on properties of electroplated Ni thin films for microsystem applications", *J. Electrochem Soc.*, vol. 153, no. 10, pp. D155-D161, 2006
- [87] W. T. Ang, P. K. Khosla, and C. N. Riviere, "Nonlinear regression model of a low-g MEMS accelerometer", *IEEE Sensors*, vol. 7, no. 1, pp. 81-88, January 2007

BIOGRAPHICAL INFORMATION

İsmail Erkin Gönenli was born in Ankara, Turkey. He received his B.Sc. (1998) in Metallurgical and Materials Engineering, from the Middle East Technical University, Ankara, Turkey. He pursued his M.Sc. degree in Materials Science and Engineering from the Pennsylvania State University, USA, in August 2001. He completed his Ph.D. degree in Electrical Engineering from the University of Texas at Arlington, in May 2010.

His research focused on design, fabrication and characterization of MEMS pressure sensors and accelerometers for aerospace applications. He is interested in continuing research in MEMS sensors for mechanical and biological applications.